Study of graphene-based high frequency optoelectronic devices for optoelectronic mixing

Alberto Montanaro

PSL
UNIVERSITÉ PARIS

THÈSE DE DOCTORAT
DE L'UNIVERSITÉ PSL

Préparée au Laboratoire de physique de l'ENS

Étude de dispositifs optoélectroniques hyperfréquence à base de Graphène pour le mélange optoélectronique

Soutenue par
Alberto Montanaro
Le 01 Avril 2019

Ecole doctorale n° 564
Physique en Île-de-France

Spécialité
Physique

Composition du jury :

Annick LOISEAU Directrice de recherche ONERA - France	*Président*
Claire BERGER Directrice de recherche CNRS Institut Néel - France	*Rapporteur*
Daniel, NEUMAIER Directeur de recherche AMO - Allemagne	*Rapporteur*
Emiliano, PALLECCHI Maître de conférences IEMN - France	*Examinateur*
Marco, ROMAGNOLI Directeur de recherche CNIT - Italie	*Examinateur*
Bernard, PLAÇAIS Directeur de recherche École Normale Supérieure - France	*Directeur de thèse*
Pierre, LEGAGNEUX Ingénieur de recherche Thales, France	co-*directeur de thèse*

LPENS
LABORATOIRE DE PHYSIQUE DE L'ÉCOLE NORMALE SUPÉRIEURE

ÉCOLE NORMALE SUPÉRIEURE

THÈSE de DOCTORAT de L'ÉCOLE NORMALE SUPÉRIEURE

École doctorale : "Physique en Île-de-France"

réalisée au
Laboratoire de Physique de l'École Normale Supérieure

présentée par
Alberto MONTANARO

En vue de l'obtention du grade de
DOCTEUR de l'ÉCOLE NORMALE SUPÉRIEURE

Sujet de la thèse :

Study of graphene-based high frequency optoelectronic devices for optoelectronic mixing

Presentée et soutenue le 1 Avril 2019 devant le jury composé de :

Mme.	Annick LOISEAU	(Présidente du jury)
Mme.	Claire BERGER	rapporteur
M.	Daniel NEUMAIER	rapporteur
M.	Emiliano PALLECCHI	examinateur
M.	Marco ROMAGNOLI	examinateur
M.	Bernard PLAÇAIS	directeur de thèse
M.	Pierre LEGAGNEUX	co-directeur de thèse

Acknowledgements

First of all, I would like to acknowledge my supervisor, Pierre Legagneux, for having given me the possibility of working in his group. I appreciated your passion in your work, your useful suggestions, your patience in the supervision of my thesis and your open mind that allowed me to develop my ideas. I also would like to acknowledge my thesis director, Bernard Plaçais. Thank you for the illuminating ideas and nuggets of scientific wisdom that you gave me each time we had the occasion to discuss.

Particular thanks to all the people with which I had the pleasure to spend my PhD in Thales Research & Technology. First of all, the *Equipe Nanocarb* in Thales: Jean-Paul Mazellier, who supervised me during my internship and during part of my PhD. Thank you for your availability anytime I needed help, and for your precious suggestions. But above all, thank you for your friendship. A big thank to Laurent, Sylvain, Lucie, Florian (les deux), Julien and all the people that I had the pleasure to meet in these years in the Lab. A particular thank to Sana, who worked on the technology that allowed me to develop my project. And of course a big thank to my big friend Pierre Luis. A special thank to all the Master students who worked on the projects, Pierfrancesco, Sajeeve, Federico and Boris.
And then the grat group of italians in TRT: Paolo Bondavalli, Giuseppe Bellomonte, Paolo Bortolotti Davide Maccariello, and then Peppino, Lorenzo, Virginio and Lorenzo for their sympathy and their spirit which made me feel at home.
The realization of my Phd project wouldn't have been possible without the contribution of all the people of the GrTM, in particular Odile Bezencenet, who did a big work in managing the fabrication of the devices, and Stéphane Xavier for the lithograpy.
I acknowledge all the people of the UMR CNRS/Thales, in particular Pierre Seneor and Bruno Dlubak, who where always available for very useful discussions.
I owe a lot of the knowledge that I had the occasion to acquire in these years to all the people of the *Laboratoire Ondes et Traitement du Signal* and the *Laboratoire de micro et nano-physique* of the Group of physics in TRT. In particular I would like to acknowledge Christian Larat and Stéphanie Molin, for having supervised my internship, and who continued to be available for very useful discussions during all my Phd. A big thank to Ghaya, Perrine, Pascale Löic, and Vincent for the daily discussions. A particular thank to Sylvain Combrie and Alfredo De Rossi, always present for suggestions and help. The RER trips passed very

fast with them and Jean-Luc Reverchon, discussing on physics and optics.
I'd like to aknowledge Arnaud Brignon for having welcomed me in the Micro and Nano physics laboratoy in TRT. Many thanks to Daniel Dolfi, who allowed me to work in the GrP, always available for interesting discussions.
Thank to the technical and administrative staff in TRT, in particular to Christine and Barbara.

Without Michael Rosticher, at the LPA, the fabrication of the super GoBN samples wouldn't have been possible, so many thanks Michael for your availability and for your professionality. Many thanks to Emiliano Pallecchi, Wei Wei and Henry Happy who have been available to collaborate for studying their transistors in Thales.

The life in Paris was not only PhD studies. I encountered a lot of people, and some of them became my family: Paolo, Emma, Carmela, Denis, Mirco, Fernando, Chiara.

A very special thank to my family, which supported and encouraged me during this period.

Thank to Paris, my home.
And thank the person who spent this piece of life with me, *ma petite Silvia*, always present.

Abstract

Since the first experiment performed in 2004 by Andrej Geim et Konstantin Novosëlov, graphene has been extensively studied in the field of photonics and optoelectronics. Its extraordinary properties include very high charge carrier mobility and light absorption in a wide spectrum of wavelengths, including the telecommunication wavelength (1.55 μm).This properties make this material very appealing for the realization of optoelectronic devices used in RADAR and telecommunications. Moreover, since graphene can be integrated the standard silicon technological platform, it has the potential to substitute III-V materials.
The application domain of graphene-based devices and components has considerably grown during the last years. Nevertheless, since the key parameters impacting the performances of graphene-based optoelectronic devices are still not properly controlled, the number of applications at the industrial scale remains very limited.
In this thesis work, optoelectronic mixing, a very used function in RADAR and telecommunication systems, is demonstrated by using graphene-based devices. First, we performed a statistical study of charge carrier mobility, residual doping and contact resistance. This study allowed to identify the best technological process and the best characterization methods (choice of the test devices and of the parameters extraction methods). By using this optimized procedure, we realized the first demonstration of a high frequency optoelectronic mixer based on graphene. Then, an in-depth study of several RF devices with different geometries allowed to identify the best operation conditions and the best design.
Using the designed coplanar waveguides as well as an alternative method relying on high-frequency based RF transistors, the optoelectronic mixing in graphene has been demonstrated up to 67 GHz.
The majority of this work has been conducted using statistical methods. To do so, I implemented a automatized experimental set-up which enabled the study of a considerable number of devices. This approach has proven to be essential for controlling and optimizing the technological process in the perspective of an industrial development.

Résumé

Depuis les premières expérimentations effectuées en 2004 par Andrej Geim et Konstantin Novosëlov, le graphène a été largement étudié dans le domaine de la photonique et de l'optoélectronique. Ses extraordinaires propriétés incluent une très grande mobilité des porteurs de charge et une absorption large bande y compris à la longueur d'onde typique des télécommunications (1.55 µm). Ces propriétés rendent ce matériau très prometteur pour les composants optoélectroniques utilisées dans les RADAR ou pour les télécommunications., En outre, comme le graphène peut être intégré sur une plateforme silicium.il apparait comme un potentiel substitut aux matériaux III-V.

Le domaine d'application des composants à base de graphène a considérablement augmenté au cours de ces dernières années. Néanmoins, comme les paramètres clés impactant les performances des dispositifs optoélectroniques basé sur le graphène ne sont pas encore bien contrôlés, le nombre d'implémentations à l'échelle industrielle reste toujours très limité.

Dans ce travail de thèse, le mélange optoélectronique, une fonction très utilisée dans les systèmes RADAR et de télécommunications, est démontré avec des dispositifs basées sur le graphène. Dans un premier temps, nous avons effectué une étude statistique de la mobilité des porteurs de charge, du dopage résiduel et des résistances de contact. Cette étude a permis d'identifier le meilleur procédé technologique et les meilleures méthodes de caractérisation (choix des composants de test et des methodes d'extraction des parametres).

En utilisant ce procédé optimisé, nous avons réalisé la première démonstration d'un mélangeur optoélectronique hyperfréquence basé sur le graphène. Puis, une étude approfondie de nombreux dispositifs RF avec différentes géométries a permis d'identifier les meilleures conditions opératives et le meilleur design.

A l'aide de lignes coplanaires mais aussi de transistors hyperfréquence à base de graphène, nous avons démontré le mélange optoélectronique à des fréquences allant jusqu'à 67 GHz.

Ce travail a été principalement mené en utilisant des méthodes statistiques. A cette fin, j'ai développé une mesure automatisée qui a permis de mesurer et d'étudier un nombre considérable de dispositifs. Cette approche s'est avérée essentielle pour contrôler et optimiser le processus technologique dans la perspective d'un développement industriel.

Table of contents

List of figures

List of tables

Chapter 1

Introduction

1.1 General Introduction

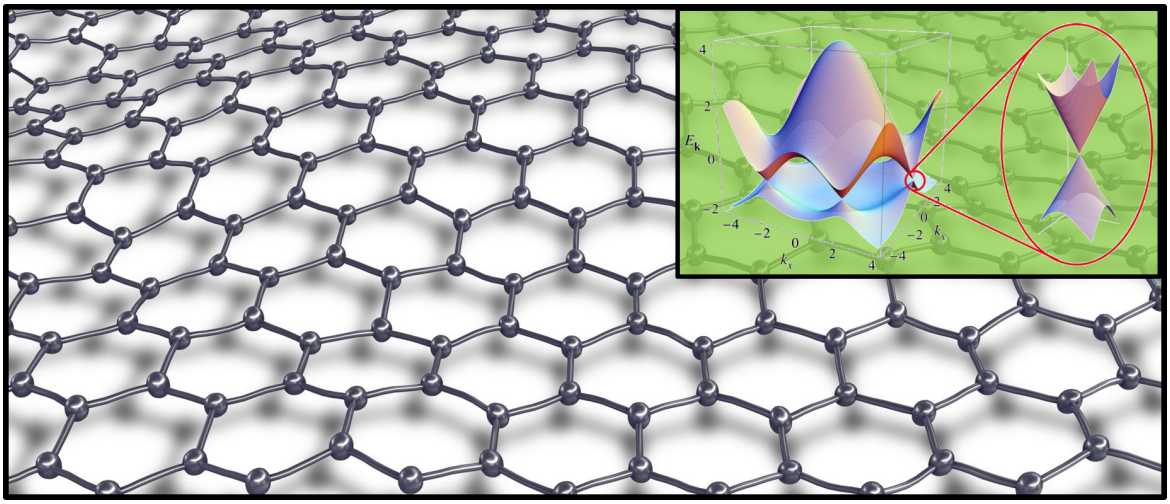

Fig. 1.1 Artistic view (taken from [1]) of a graphene monolayer. In the inset, the band structure of graphene in the Brillouin zone (image adopted from [2])

.

In 1947, the theoretical physicist Philip Russell Wallace described for the first time the electronic band structure of a single monoatomic layer of graphite [10]. In 1986, this atomically thin layer was named *graphene* for the first time by Hanns-Peter Boehm et al.[11]. In 2004, an ultrathin epitaxial graphite composed by three-layer graphene, showing a remarkable 2D electron gas behavior, was described [12]. In the same year, i.e. about 60 years later from its band structure calculation, the graphene has been isolated for the first time by Andrej Gejm and Konstantin Novosëlov using mechanical exfoliation[13]. A. Gejm and K. Novosëlov received the Nobel Prize in Physics in 2010 *"for groundbreaking experiments regarding the two-dimensional material graphene"*.

Since that moment, this material has been extensively studied from both fundamental and applied standpoints.

In this thesis work, the extraordinary electronic and optical properties of graphene [2, 14] have been investigated and exploited to demonstrate applications in the field of high frequency optoelectronics. In particular, the use of graphene as active material to implement fast photodetectors will is investigated. We show that fast graphene photodetectors are suitable for implementing optoelectronic mixing (OEM), a function which is particularly demanded in telecommunications and radar systems. This thesis includes 5 Chapters organized as follows:

This first Chapter describes the electrical and optical properties of graphene. We present the theory of electronic transport in graphene and the principal photocurrent generation mechanisms involved in biased graphene.

The second Chapter is dedicated to the description of the experimental methods. Using graphene grown by chemical vapor deposition (CVD), DC and RF devices have been fabricated. We present the different fabrication steps and then the characterization techniques used to measure these devices.

In the third Chapter, the quality of several samples processed using different technological steps is evaluated. The evaluation has been conducted by comparing the performances of the DC devices fabricated on each sample. Three relevant parameters have been taken into account in order to evaluate the devices performances: residual charge carrier density, charge carriers mobility and contact resistance. Then, an analysis of the impact of mobility and contact resistance on the photocurrent generation is performed.
The study presented in this Chapter served to identify an optimized technological process, which has been consequently used to fabricate a 2-inch sample containing both RF and DC devices. The measurement of the DC devices contained in this sample constitues the last part of the Chapter.

The fourth Chapter concerns the presentation of the RF devices used to demonstrate OEM in graphene. It starts with an introduction to OEM (basic principle and state of the art) and an overview of the state of the art of graphene-based photodetectors. Then, it presents the characterization of photodetectors and optoelectronic mixers contained in the 2-inch sample introduced in Chapter 3. At the end of the Chapter, a very high performance device fabricated in collaboration with the Ecole Normale Superieure is presented. It is based on a very high carrier mobility graphene flake encapsulated in hexagonal boron nitride.

Chapter 5 contains the study of optoelectronic mixing using a high-frequency graphene-based transistor fabricated at IEMN in Lille. The measurement of the devices allowed us to identify the working principle of a graphene transistor used as an optoelectronic mixer.

A large part of the experiments has been performed using a statistical approach. In particular, in Chapter two, more than 500 devices have been characterized to extract the relevant parameters. Experiments in Chapter 4 are also supported by the measurement of 52 RF devices.

The statistical approach has required an effort in the automation of the optoelectronic experimental set-up, which has been an integral part of this thesis, and has been necessary in order to obtain reliable results in a reasonable amount of time. As we observed a large dispersion in the electrical measurements, this peculiar approach is, in our opinion, essential to accurately compare different devices and also to evaluate a technological process for an industrial application.

1.2 Electronic and optical properties of graphene

1.2.1 Electronic band structure

Graphene is an allotrope form of carbon. It consists of a monoatomic layer of carbon atoms organized in an honeycomb structure, as shown in figure 1.1. This structure is at the basis of the extraordinary properties of graphene. In particular, the peculiar electronic and optical properties of graphene come from its electronic band structure, which calculation is present in many references [2]. In the following, the important results are presented.

The Bravais lattice of graphene can be described as the combination of two triangular

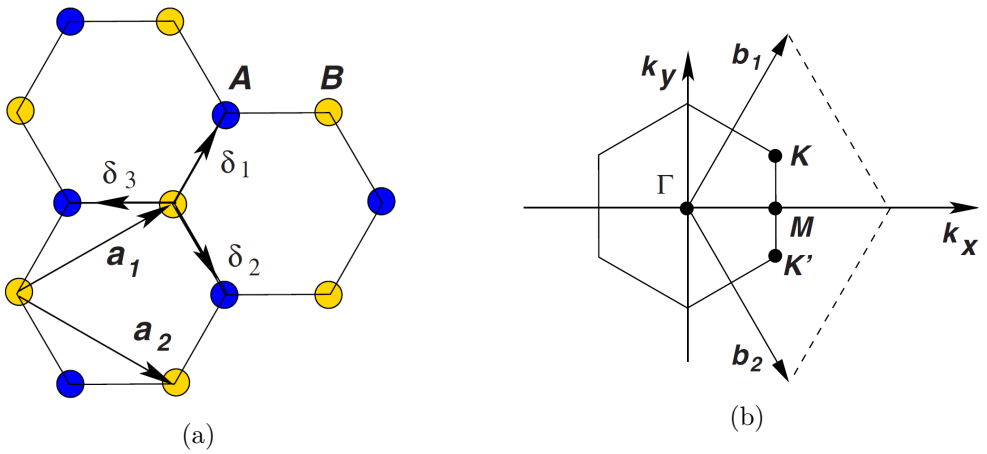

(a) (b)

Fig. 1.2 a) Graphene lattice, composed by two triangular sub lattices, indicated in blue and yellow. b) Brillouin zone of the reciprocal lattice. Images taken from [2]

sub-lattices, which are indicated in blue and yellow in figure 1.2a. The unit cell is composed by two atoms (one for each sub-lattice). The two lattice basis are described by the vectors:

$$\vec{\boldsymbol{a_1}} = \frac{a}{2}(3, \sqrt{3}) \qquad \vec{\boldsymbol{a_2}} = \frac{a}{2}(3, -\sqrt{3}) \tag{1.1}$$

where a = 1.42Å is the distance between the nearest-neighbors carbon atoms. The reciprocal lattice vectors are so given by:

$$\vec{\boldsymbol{b_1}} = \frac{2\pi}{3a}(1, \sqrt{3}) \qquad \vec{\boldsymbol{b_2}} = \frac{2\pi}{3a}(1, -\sqrt{3}) \tag{1.2}$$

which define the Brillouin zone, depicted in figure 1.2b. In order to compute the band structure of graphene, a tight-binding approximation is sufficient [2], taking into account the hoping of electrons between the nearest-neighbor and next-nearest-neighbor atoms. The solution of the tight-binding Hamiltonian gives the following energy relation for electrons in the π bands in the reciprocal space [10]:

$$E_{\pm}(\boldsymbol{k}) = \pm t\sqrt{3 + f(\boldsymbol{k})} - t' f(\boldsymbol{k}) \tag{1.3}$$

with

$$f(\boldsymbol{k}) = 2cos(\sqrt{3}k_y a) + 4cos(\sqrt{\frac{3}{2}}k_y a)cos(\frac{3}{2}k_x a) \tag{1.4}$$

t and t' being the hoping energies for the nearest-neighbor and the next-nearest-neighbor site, and k_x, k_y the reciprocal space vectors. The plus sign in equation 1.3 refers to the upper (*conduction*) band and the minus to the lower (*valence*) band.
The energy dispersion profile described by equation 1.3 is depicted in the inset of figure 1.1. There are two coordinates in the Brillouin zone (**K** and **K'** in figure 1.2b) at which the conduction and valence band touch each other. These two points are also called Dirac points. By developing equation 1.3 around the the K points, one finds:

$$E_{\pm}(\boldsymbol{k}) = \pm\hbar v_f |\boldsymbol{k}| + O((\frac{k}{K})^2) \tag{1.5}$$

being $v_f = \frac{3ta}{2\hbar} = 10^6 m/s$ the Fermi velocity. This equation shows that electrons and holes have a linear dispersion relation near the K points. This relation, that is unusual in semiconductors (which generally have a quadratic dispersion) is very similar to the energy dispersion relation of photons:

$$E = \hbar c k \tag{1.6}$$

where c is the speed of light. Fermions exhibiting this linear dispersion are called Dirac fermions, since they are described by the Dirac equation, and behave as massless relativistic particles.

1.2.2 Graphene-based field effect transistors

1.2.2.1 Carriers statistics

Since graphene is a monoatomic layer, the computation of carrier statistics is done by considering the general formulas used for a two-dimensional electron gas. By doing so, The density of states in graphene at a specific energy E is given by [15]:

$$g_{g2D} = \frac{2|E|}{\pi\hbar^2 v_f^2} \tag{1.7}$$

Which is computed by taking into account the valley and spin degeneracy, and using the dispersion relation given in equation 1.5. The electrons density per unit area is then given by:

$$n_e = \int_0^{+\infty} g_{g2D}(E_F) f_{FD}(E - E_F) dE \tag{1.8}$$

while the holes density is:

$$n_h = \int_{-\infty}^{0} g_{g2D}(E_F)[1 - f_{FD}(E - E_F)] dE \tag{1.9}$$

Where E_F is the Fermi energy level and f_{FD} the Fermi-Dirac distribution. The total charge carriers density n is given by the sum of n_e and n_h, and does not have a closed formula. For $E_F \gg k_B T$ (k_B being the Boltzmann constant and T the temperature) the expression of n becomes [15]:

$$n = \frac{E_F^2}{\pi\hbar^2 v_f^2} \tag{1.10}$$

1.2.2.2 Electrostatics and electronic transport in graphene-based transistors

Figure 1.3a shows a schematic representation of a graphene-based transistor. The structure is composed by a graphene film which is transferred on a substrate and contacted by two electrodes (source and drain). Moreover, an insulating layer separates the graphene layer from a third electrode (gate). The application of a voltage potential between the gate and the graphene channel modifies the Fermi energy in graphene. This is the well known field effect, which is exploited in semiconductors in order to operate transistors. However the transistors based on this material show some peculiar properties which are not present in transistors based on ordinary semiconductors. Since this basic structure will be used throughout this work, a brief description is given in this section, following ref [15].

Considering the capacitor formed by the metal-insulator-graphene stack depicted in figure 1.3b, the electrochemical potential at the metal and at the graphene can be respectively

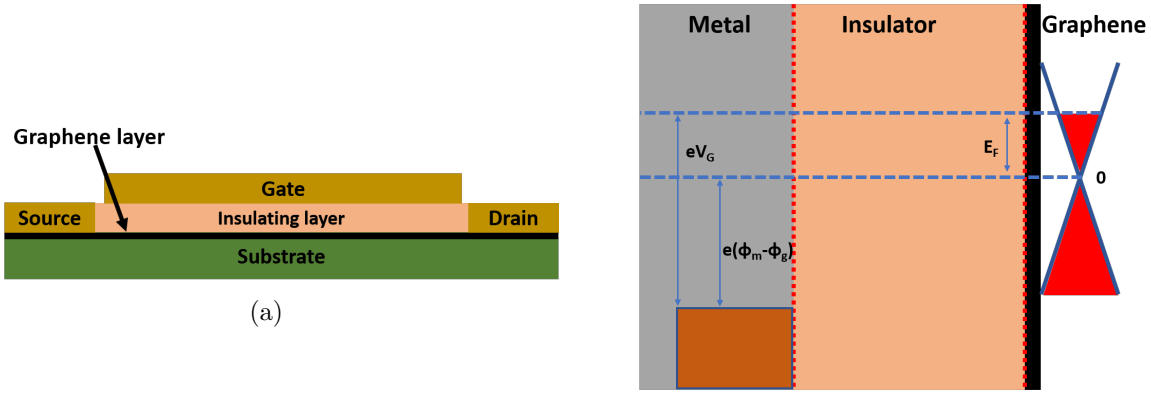

(a) (b)

Fig. 1.3 a) Graphene field effect transistor. b) Band diagram of a metal-insulator-Graphene stack

written as [15]:

$$\Psi_m = -e\phi_m - W_m \tag{1.11a}$$

$$\Psi_g = -e\phi_g + E_F - \chi_g \tag{1.11b}$$

$$\tag{1.11c}$$

ϕ_m and ϕ_g being respectively the metal and graphene electrostatic potentials, χ_g the graphene electron affinity, W_m the metal work function and E_F the graphene chemical potential with respect to the charge neutrality point (CNP), this last defined as $E_{NP} = -e\phi_g - \chi_g$. When a voltage V_G is applied between the metal and the graphene channel, this sets the total electrochemical potential, which then becomes:

$$eV_G = \Psi_g - \Psi_m = E_F + e(\phi_m - \phi_g) \tag{1.12}$$

In the formula, for sake of simplicity, we consider $W_m \approx \chi_g$. The second term in equation 1.12 refers to the electrostatic potential, which corresponds to an electric field in the oxide layer, as in a common parallel plate capacitor:

$$\phi_m - \phi_g = E_{ox} t_{ox} = \frac{en}{C_{ox}} \tag{1.13}$$

where $C_{ox} = \frac{\epsilon_{ox}\epsilon_0}{t_{ox}}$ (being ϵ_0 and ϵ_{ox}, respectively, the vacuum permittivity and the relative permittivity of the material acting as insulating layer, and t_{ox} the thickness of the insulating layer). So, equation 1.12 can be rewritten as:

$$eV_G = E_F + \frac{e^2 n}{C_{ox}} \tag{1.14}$$

Very close to the Dirac Point, the term E_F is not negligible (quantum capacitance regime [16]). For $eV_G \gg E_F$, the carrier density can be calculated from V_G within the parallel capacitor approximation, by neglecting E_F.

$$n(V_G) = \frac{C_{ox} V_G}{e} \tag{1.15}$$

A more realistic formula to obtain the charge carrier density n from the applied gate voltage V_G takes into account also the residual charge carrier density n_0:

$$n_{tot} = \sqrt{n^2(V_G) + n_0^2} \tag{1.16}$$

n_0 is the minimal charge carrier density achievable and is an effective quantity which takes into account the residual charge in the oxide, at the graphene/oxide interface, and disorder induced charge density. The modulation of n by means of a gate voltage is referred to as *electrostatic doping*. Typically, the free carriers density can be tuned from 10^{11} up to 10^{13} cm^{-2} by applying a gate voltage that moves the Fermi level from 10 to 400 meV away from the Dirac point. Moreover, thanks to its gapless nature, the channel of a graphene transistor exhibits *ambipolar conduction*. This means that the charge carriers can be either electrons or holes, depending on the gate-channel bias. The typical resistivity curve as a function of the applied gate voltage is shown in figure 1.4.

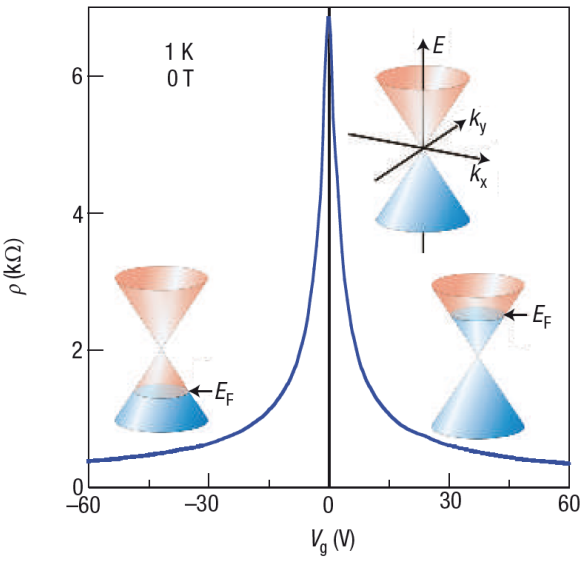

Fig. 1.4 Resistance vs gate voltage in a graphene field effect transistor. Taken from [2]

.

At a given charge carrier density, the channel sheet conductivity in the diffusive regime can be calculated as:

$$\sigma = ne\mu \tag{1.17}$$

where μ is the charge carriers mobility, which is normally expressed in $cm^2V^{-1}s^{-1}$. By referring to figure 1.3a, the total measured resistance between the source and the drain contacts comprises a resistance due to the metal/graphene contacts (*contact resistance*), and the graphene channel resistance.
Mobility, contact resistance and residual doping are the figure of merit that will be taken into account to benchmark the quality of the fabricated devices.

1.2.3 Photocurrent generation mechanisms in biased graphene

Nair et al. [17] calculated in 2008 the absorption of light by a two-dimensional Dirac fermions gas, by using the Fermi's golden rule. They showed that this quantity is solely defined by the fine structure constant $\alpha = \frac{1/4\pi\epsilon_0 e^2}{\hbar c}$:

$$A_g = \alpha\pi \simeq 0.023 \tag{1.18}$$

This value is relatively high if one considers that the absorption takes place in a monoatomic film. Thanks to the absence of a bandgap, and since the dispersion relation in graphene remains quasi-linear up to at least 0.5 eV [18, 19], this formula is valid for a very wide optical spectrum, which includes UV, visible and infrared wavelengths [17].
The absorbed light can be converted in an electrical current, and this allows the use of graphene as an active material to build photodetectors. The conversion of the absorbed light in an electrical signal can be enabled by different physical mechanisms which can take place in graphene. Among them two mechanisms are dominant in biased graphene[1]. These two mechanisms are the ones of interest in this work, and are briefly presented in the following.
Let's consider the structure in figure 1.5 which is very similar to the one presented in paragraph 1.2.2.2: a graphene layer is transferred on an insulating layer, supported by a conducting substrate, and then it is contacted by two electrodes. In this case, the conducting substrate can be used as a back-gate. An experimental evidence of the photocurrent generation dependence on electrostatic doping has been shown by Freitag et al. [3]. A light beam was focused on a graphene channel, as shown in figure 1.5. A voltage was applied between the two contacts, and the generated photocurrent was measured. Figure 1.6a shows the magnitude of the photocurrent with respect to the voltage applied along the graphene channel. The measurement was performed at high and low electrostatic doping, by changing the back-gate voltage. In both cases, the photocurrent has a linear dependence on the bias voltage. This suggests that light changes the conductivity of the graphene layer in both cases. However,

[1] "*biased graphene*" refers to a graphene channel submitted to an electric field

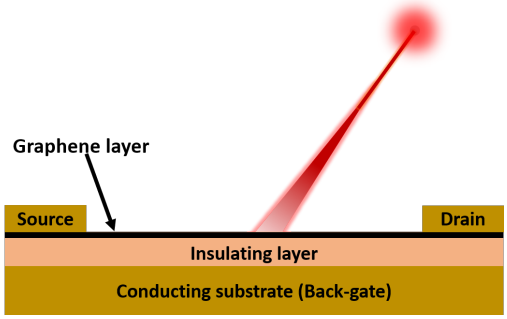

Fig. 1.5 Graphene field effect transistor in back-gate configuration. A light beam that is shined on the graphene layer generates a photocurrent between the source and drain contacts

.

the photocurrent sign is different in the two regimes. This is even more clear in figure 1.6b, where the photocurrent is plotted with respect to the back-gate voltage. At low elctrostatic doping, the photocurrent has the same sign of the current flowing in the graphene channel due to the applied voltage V_{DS}. For this doping level, the carrier concentration n rises up to $n+n^*$. This increases the conductivity σ from $ne\mu$ to $(n+n*)e\mu$ [3]. We will refer to this regime as ***photoconductive regime***.

At high electrostatic doping, the dominant physical mechanism enabling photodetection is the bolometric effect [20, 3]: the power of the electromagnetic radiation incident to the graphene channel generates heating, which changes the transport conductance. In particular, the increase in carrier temperature induces a decrease of carriers mobility [3]. We will refer to this regime as ***bolometric regime***.

These two mechanisms will be used to demonstrate high frequency photodetectors and optoelectronic mixers.

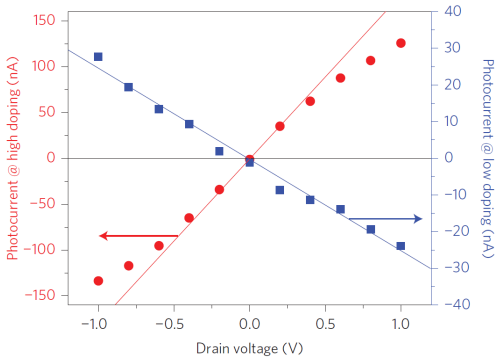

(a)

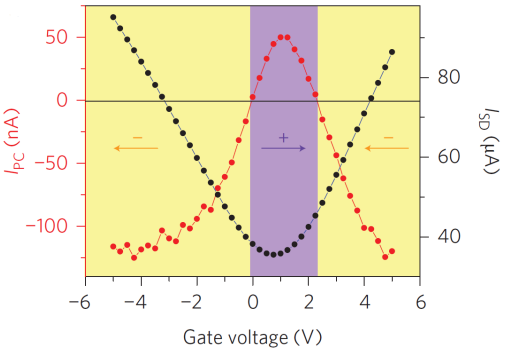

(b)

Fig. 1.6 a) Generated photocurrent in a graphene monolayer at high (red curve) and low (blue curve) electrostatic doping, as a function of the source-drain bias. b) Photocurrent amplitude as a function of the back-gate voltage. Images taken from [3].

Chapter 2

Experimental Methods

A good control of the graphene electrical parameters, such as carrier mobility, contact resistance and doping, is essential to understand the optoelectronic properties of graphene devices. This control involves primarily the technological process. In this Chapter, the fabrication steps for the production of the graphene-based devices are presented, as well as the devices structure and functionality. A particular emphasis is put on a method developed in Thales [21], which has the double purpose of protecting graphene during the technological steps and passivating the fabricated devices. This process stabilizes and improves the electrical properties of the devices.
The second part of the Chapter is dedicated to the presentation of the experimental setup used for the characterization of the devices. In particular, a description of the DC measurement setup is provided, as well as a detailed presentation of the experimental setup for high frequency optoelectronic measurements.

2.1 Technological Process

2.1.1 Devices overview

During this work, two types of devices have been realized and measured:

1. ***DC devices***. They served to characterize the carrier mobility and contact resistance. Figures 2.1a and 2.1b show the two kinds of DC devices: Hall-bar-like devices used for four-probe measurement, and TLM (Transfer Length Method) devices. The experimental setup and the measurement methods are presented in section 2.2.2.

2. ***RF devices***. Figure 2.1c shows the picture of a typical RF device. It consists in a coplanar waveguide (CPW) in a signal-ground-signal configuration, that embeds a graphene mono-layer in the middle of the signal line. The description of the experimental methods used to characterize these devices is described in section 2.2.3.

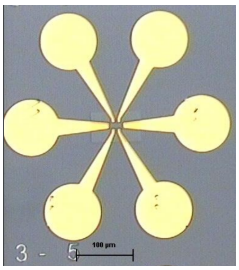

(a) four-probe measurement devices

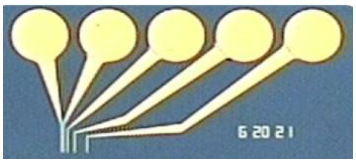

(b) TLM devices

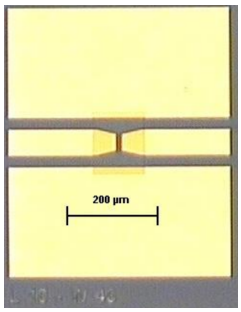

(c) RF devices

Fig. 2.1 Devices Typologies. a) and b) are, respectively, Hall-bar like devices for four-probe measurement, and TLM structures. c) is a CPW embedding graphene, for RF opto-electronic measurements

Both typologies of device share the same structural design: a graphene film is transferred on a Si/SiO_2 substrate, patterned and then contacted by metallic contacts. Moreover, a voltage can be applied between the silicon substrate and the graphene channel, in order to tune the carrier density by field effect (see Chapter 1). From this common principle, each device has a particular geometry. The four-probe devices and the TLM structures have been used to evaluate the contact resistance and the carrier mobility of the graphene samples. In the RF devices, graphene is embedded in an RF structure (a CPW), which allows to fabricate devices operating at high frequency.
All the devices share the same fabrication method, which is described in the following section.

2.1.2 Fabrication procedure

The fabrication of the devices follows a technological process flow that consists in several fabrication steps. Figure 2.4 schematically summarizes the different steps.

a) Graphene growth and transfer The first fabrication step was performed by the Spanish company *Graphenea*. Graphene was grown by Chemical Vapour Deposition (CVD) method [22–24] on copper foils. The procedure to transfer graphene from the copper foil to the SiO_2/Si substrate is schematically showed in figure 2.2a: a PMMA (Poly(methyl methacrylate)) resist is deposited on the graphene surface. Then the stack Cu/graphene/PMMA is immersed in a solution that etches the Cu foil, resulting in the PMMA/graphene stack floating above the solution. Next, the stack is put on a SiO_2/Si substrate. Finally, the PMMA film is dissolved in acetone.
Figure 2.2b shows graphene monolayer transferred by Graphenea on a 4" wafer. Two different substrates were used in this work. The first is a doped silicon with 300 nm of silicon oxide on top of it. The second one is a high resistivity (20000 Ωcm) silicon substrate with a $2\mu m$

silicon oxide on top. In both cases, the silicon dioxide was obtained by thermal oxidation of the silicon substrate.

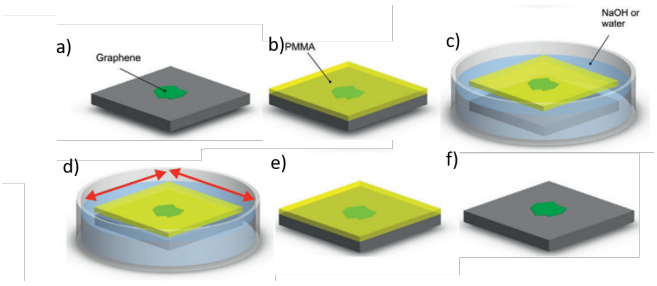

(a) Graphene Transfer process flow (adopted from [24])

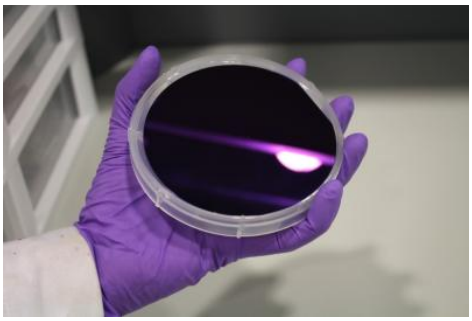

(b) Monolayer graphene transfer on a four inch wafer adopted from [25]

Fig. 2.2 Graphene Transfer

b) Protection layer deposition The second step consists in depositing a 1 nm thick aluminum layer by evaporation, that is subsequently oxidized in air. This layer insures the protection of graphene, during the device fabrication in order to minimize the contamination of the graphene surface[26, 27].

c) Alignement marks deposition Alignment marks are defined by optical or electronic lithography. The marks are used to align all the other lithographic masks.

d) Graphene etching The graphene channel of each device is defined by oxygen plasma etching. Figure 2.3 shows the graphene channel (green pattern) for four-probe measurement devices. As can be noticed, two lithography steps were used to define the graphene channel. The larger one is the first used, and defines a first rectangle. Then, the final shape of the channel is obtained by another etching step using the second mask. This 2-step method has been used since it minimizes the risk of detachment of the graphene channel.

e) Metallic contacts deposition The metallic contacts geometry is then defined by an optical or electronic lithographic step. The metal is deposited by sputtering or evaporation methods, followed by lift-off process. Figure 2.3 shows on the left the metallic contact pads (grey patterns).

f) Passivation The last step consists in the deposition of a layer of aluminum oxide (Al_2O_3) by atomic layer deposition (ALD). It consists of sequential alternating pulses of gaseous chemical precursors which leave, for each gas pulse, no more than one monolayer at the substrate surface, through a self-limiting process. Thus, this method allows to control the

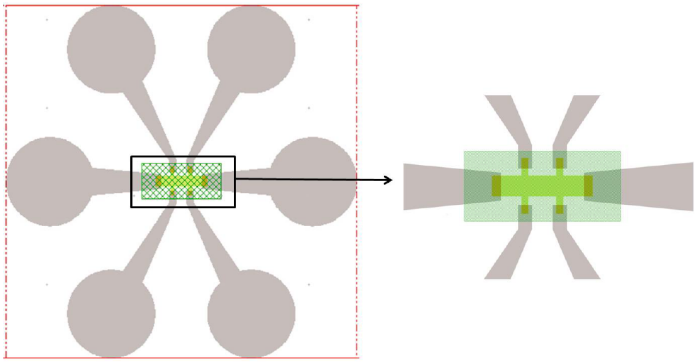

Fig. 2.3 Metal and graphene etching levels masks

number of atomic layers that are deposited. This step was carried out by the University of Cambridge, and then at Thales R&T.
To study the impact of the technological process on the devices electrical performances, we have fabricated devices with some variants (e.g. thermal anneal) or without protection/passivation layers.

2.2 Experimental setup

2.2.1 The probe station

The fabricated devices four-probe devices and TLM have been tested using DC electrical measurement, while CPW have been characterized through high-frequency electrical characterization methods. The common environment on which all these measurements have been implemented is a probe station Cascade Microtech Summit 12000. This platform has been integrated with a 1.55 μm optical column, which has been designed as part of this thesis work, in order to perform optoelectronic measurements on our devices. The main parts of the probe station are highlighted in figure 2.5:

(A) Chuck, which is the metallic support on which the samples are positioned. The chuck can be moved in the x,y, and z direction with a micrometric resolution. A BNC port is electrically connected to the chuck, thus giving the possibility to apply an electrical voltage.

(B) RF probes for high-frequency measurements of the CPW. The pitch of the probes can be 100 μm or 250 μm, depending on the devices.

(C) DC multi-probes used to perform DC measurements on four-probe devices.

(D) Single DC probes.

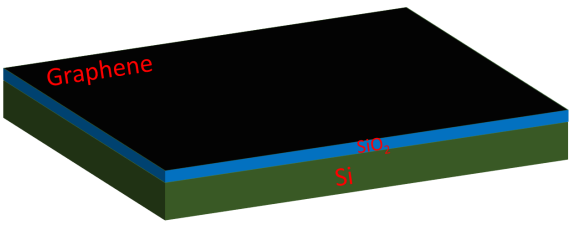

(a) Graphene Transfer

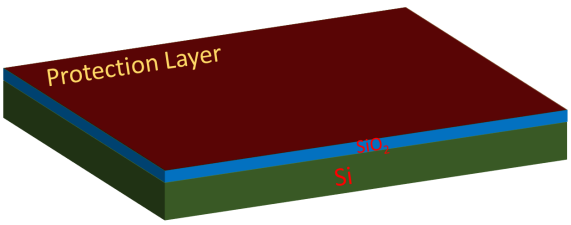

(b) Protection layer deposition

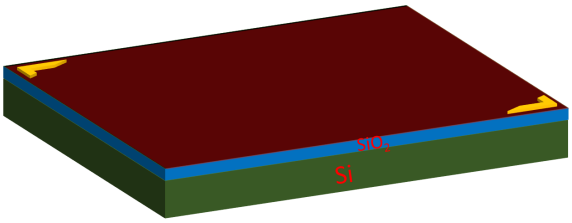

(c) Alignment Marks deposition

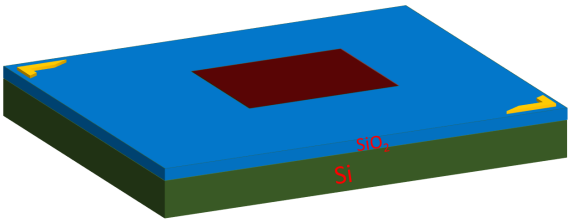

(d) Graphene etching

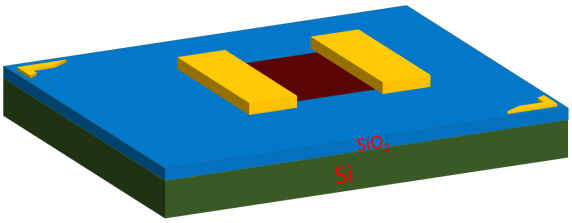

(e) Metallic contacts deposition

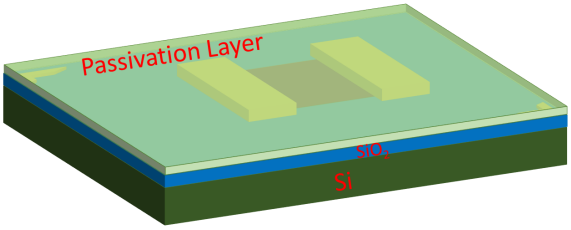

(f) Passivation

Fig. 2.4 Fabrication Process Flow

(E) Visible optical microscope. This microscope is equipped with a variable 1X/8X zoom, used during the positioning of the DC and RF probes.

(F) Infrared (1.55 μm) optical column, which has the double purpose of imaging the devices and focusing a 2 μm diameter laser beam on the devices. Moreover, thanks to three stepper motors, the laser beam can be displaced in order to perform a scan all over the graphene channel surface.

The visible microscope and the imaging infrared system for laser focusing are interchangeable. All DC and RF probes are supported by micropositioners to accurately position them on the device contact pads. The probes are then connected to various electrical instruments. The DC probes are connected to Source Measure Units (SMUs) (Keithley 2636), capable of measuring and sourcing voltages and currents. The RF probes (ACP GSG-100 and GSG-250 from Cascade Microtech) are connected to a Vector Network Analyzer (VNA) (Model Rohde & Schwarz ZVA67) to probe high-frequency electrical signals. SMUs are also used to add a DC bias to the RF signals. This is performed thanks to bias tees integrated in the VNA. The detailed DC and RF optoelectronic setup is discussed in the next sections.

2.2.2 DC measurement methods

As shown in figure 2.6, the total resistance of a graphene device is composed of the graphene channel resistance and also of two contact resistances that rise from the metal-graphene contacts. This contribution limits the device performances. In addition to this, contact resistances affect also the extraction of the carriers mobility, leading to underestimated values. The fabricated DC devices allowed us to access to these quantities.

Four-probe measurements One way to eliminate the contact resistance from the measurement is the four-probe method. It consists in contacting a material in four points, as showed in figure 2.7. A current I is imposed between the external contacts A and B, while zero current is imposed between the internal contacts (C and D). Then, the voltage drop across the points C and D ($V_{INT} = V^+ - V^-$) is measured. This voltage drop is only due to the current imposed by the external contacts and is not affected by the contact resistance. By knowing the distance l between points C and D, and the channel width W, the square resistance of the graphene channel without the contribution of the contact resistance can be simply extracted:

$$R_{\square} = \frac{V_{INT}}{I}\frac{W}{l} \tag{2.1}$$

An extimation of the contact resistance can then be extracted from:

$$R_{cont} = R_{tot} - R_{\square}\frac{W}{L} \tag{2.2}$$

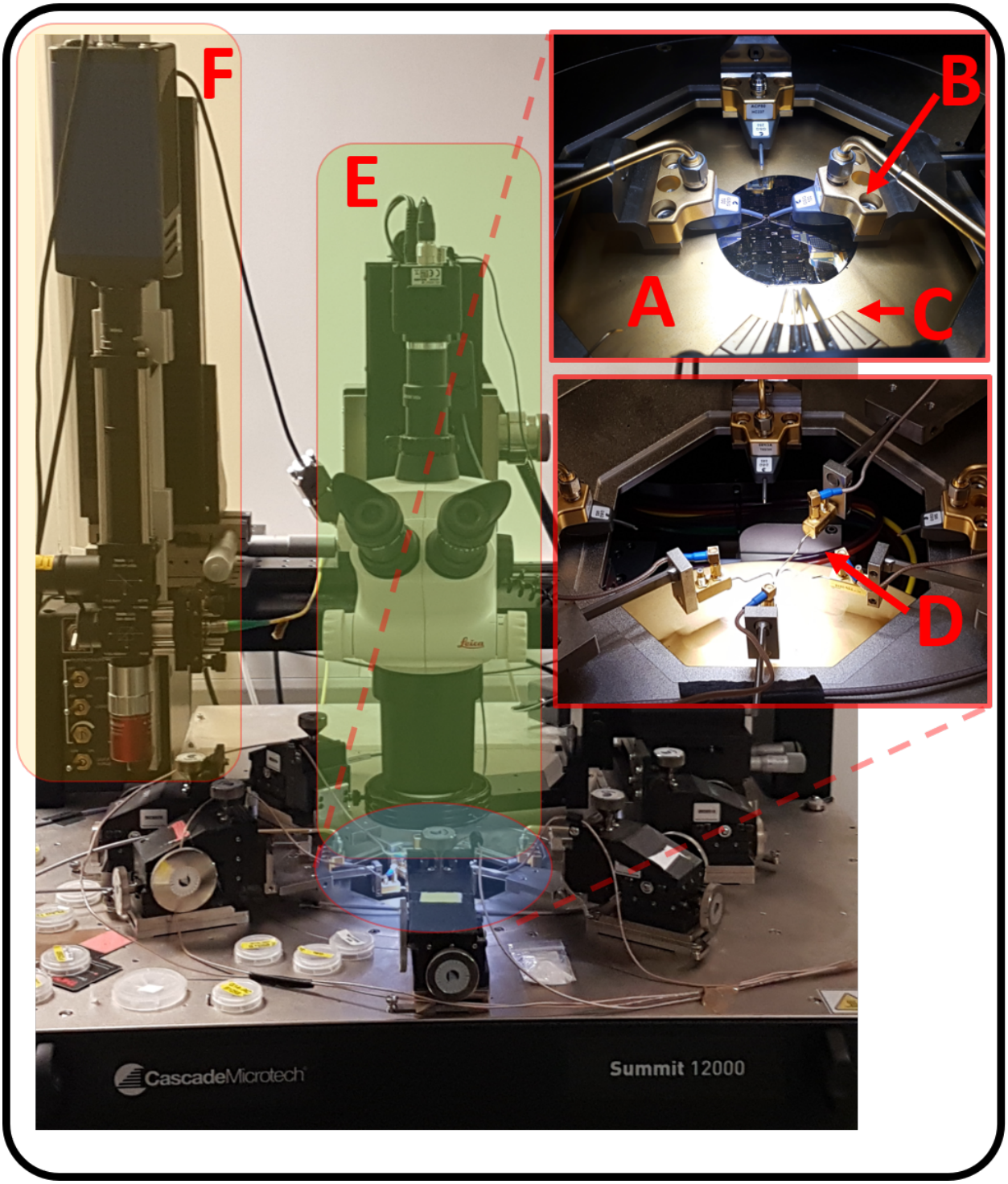

Fig. 2.5 Probe Station. The principal elements constituting the system are indicated with letters. The blue region highlighted in blue is zoomed in the two figures on the right. The chunk is the metal plate which supports the samples under test (A). RF, DC multi-probes and single DC probes are indicated, respectively with the letters B, C and D. The visible optical microscope is indicated with the letter E and is highlighted in green. The infrared optical column is in dicated with the letter F and highlighted in orange

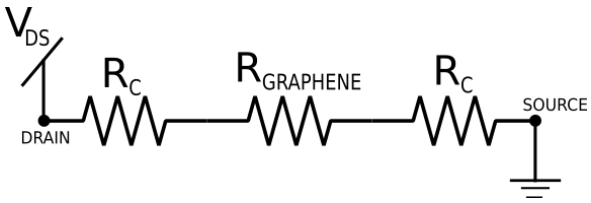

Fig. 2.6 Schematic of the measured resistance on a graphene device. The total resistance is the series contribution of two contact resistances due to the metal-graphene contacts plus the graphene channel resistance

.

Where $R_{tot} = V_{AB}/I$. It is important to notice that we used non-invasive contacts to probe

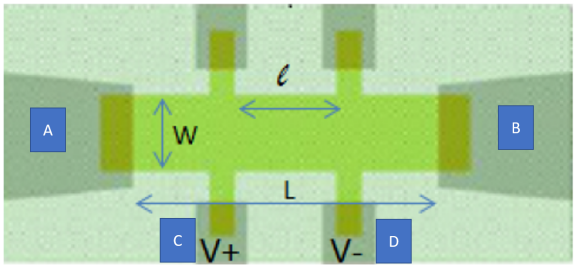

Fig. 2.7 four-probe measurement configuration

.

the internal voltage drop (contacts C and D). As highlighted by [28], top contacts modify the graphene carrier concentration under or close to the contacts. This leads to false measurement values [29]. The use on non-invasive contacts avoids this effect.

TLM measurements TLM devices are made of a graphene layer contacted by 5 contacts, as shown in figure 2.8a. The inter-contacts distance varies, so creating 4 channels of different lengths L_i. By placing two tips on two adjacent contacts and applying a source-drain voltage $V_{SD,i}$, a current $I_{SD,i}$ flows between the contacts and so the total resistance $R_{TOT}(L_i)$ can be measured:

$$R_{TOT}(L_i) = R_{Channel}(L_i) + 2R_c = R_{\square}\frac{L_i}{W} + 2R_c = \frac{V_{SD,i}}{I_{SD,i}} \tag{2.3}$$

The contact resistance as well as the square resistance of graphene is then extracted by fitting equation 2.3 (figure 2.8b).

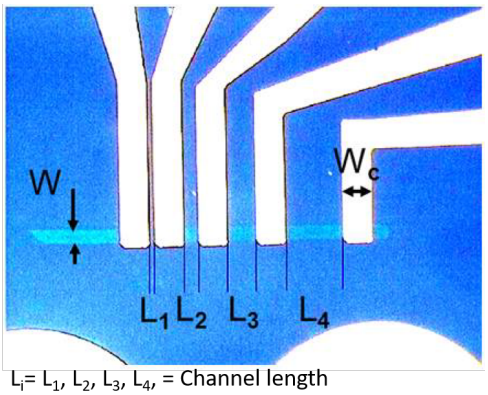

(a) TLM device channel

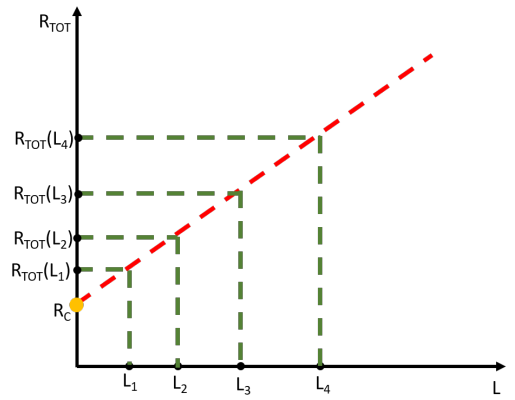

(b) Curve for the extraction of contact resistance starting from a TLM measurement

Fig. 2.8 TLM Measurement

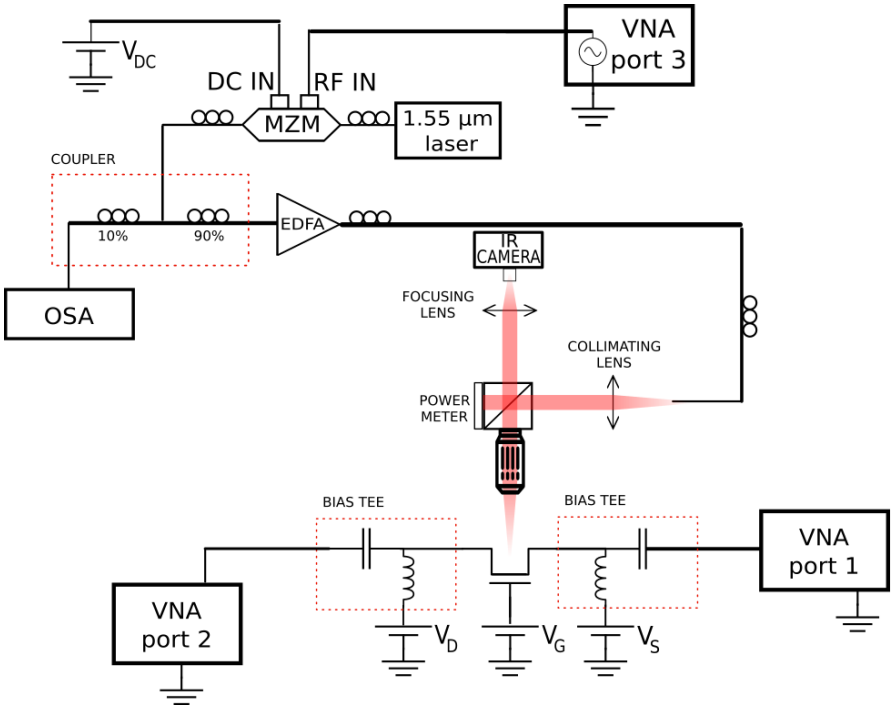

Fig. 2.9 Experimental setup for high frequency optoelectronic measurements

.

2.2.3 High frequency optoelectronic setup and measurement methods

2.2.3.1 High frequency optoelectronic setup

The setup designed for the optoelectronic measurements is schematically shown in figure 2.9. It is composed by 3 parts:

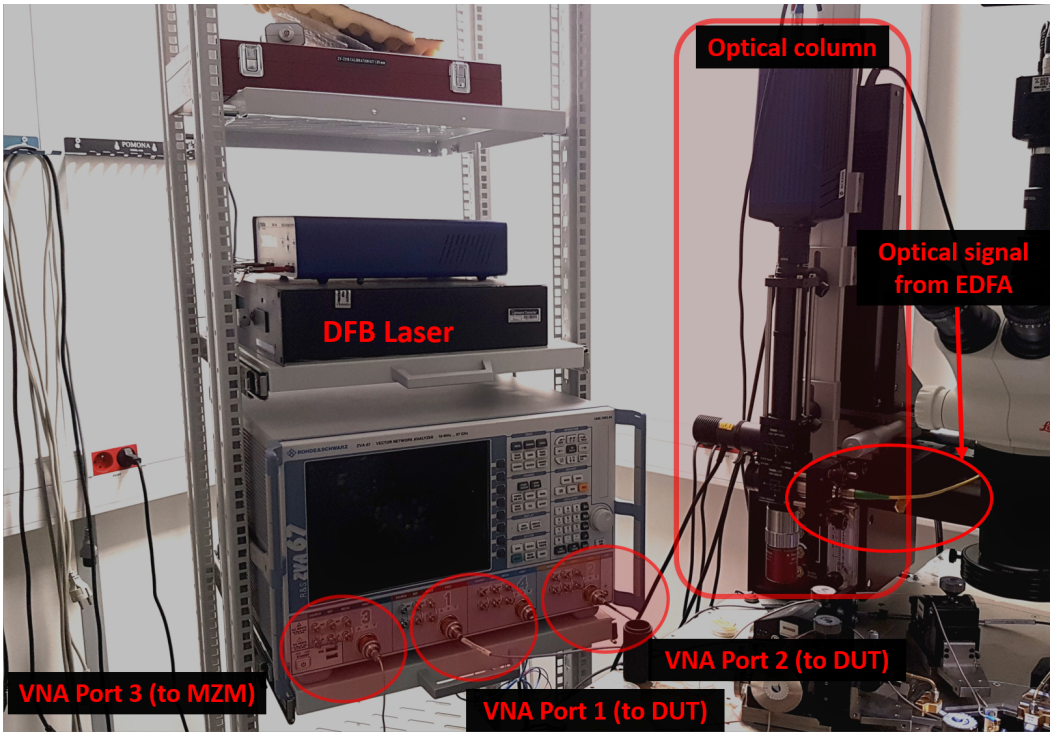

Fig. 2.10 Particular of the experimental set-up, comprising the VNA, the laser source (Distributed feedback laser) and the optical IR column

.

1. **Optical signal generation:** A 1.55 μm wavelength distributed feedback laser (DFB) laser beam (indicated in figure 2.10) is modulated by a Mach-Zehnder Modulator (MZM) operating up to 40 GHz. The output of a MZM is then split by means of a 10%/90% coupler. The 10% output is coupled to an optical signal analyzer (OSA) to monitor the modulation of the laser beam performed by the MZM. The 90% output is amplified by an Erbium-doped fiber amplifier (EDFA). The output of the EDFA is then coupled with the second stage. An image of this part of the experimental setup is shown in figure 2.11.

2. **Optical coupling with the sample and imaging:** The amplified optical beam is coupled to the optical column (indicated in figure 2.10), collimated and then focused on the samples by means of a 20x infinity corrected objective with a working distance of 20 mm and a focal length of 10 mm. Figure 2.12a shows the objective positioned over the

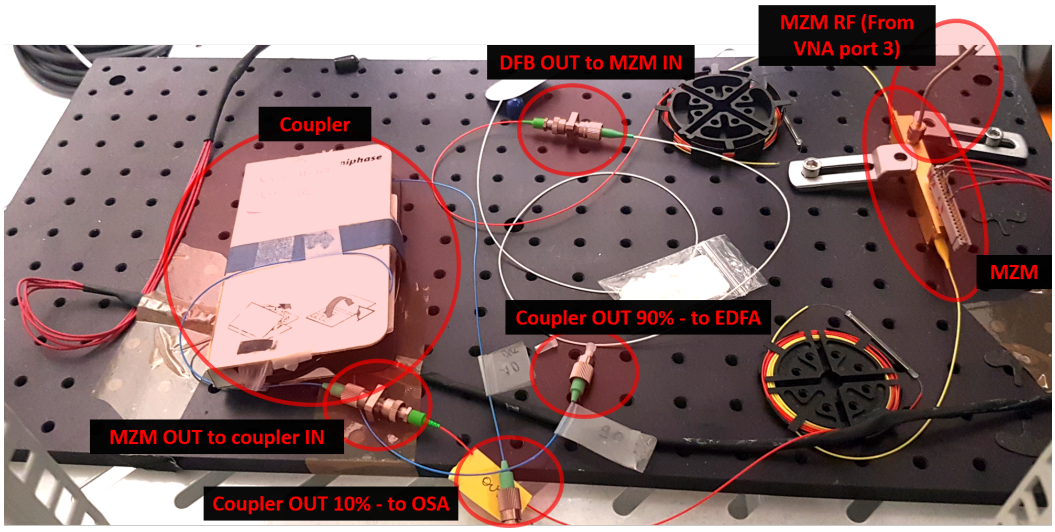

Fig. 2.11 Particular of the experimental setup, comprising the Mach-Zehnder modulator that modulates the light coming from the Distributed feedback laser. The 10% of the MZM optical output is sent to an optical spectrum analyzer, while the other 90% is sent to an Erbium-doped fiber amplifier before being focused on the device under test.

.

sample. The optical column serves also as imaging system: a 1.55 μm Light-Emitting Diode (LED) is used to illuminate the samples. the image is then collimated by the objective and focused by means of a 200 mm lens on the focal plane of an IR camera. An image of the focused beam on the samples imaged by the IR camera is shown in figure 2.12b. The laser spot that is focused on the samples can be moved with submicrometric precision over the samples by means of two stepper-motors that control the position of the fiber collimator with respect to the principal optical axis.

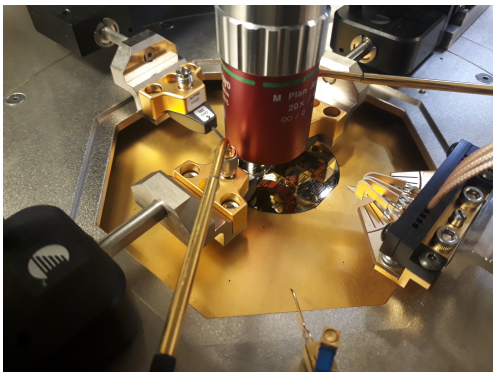

(a)

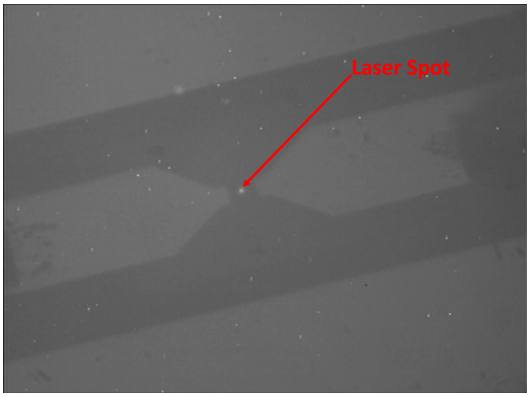

(b)

Fig. 2.12 *a)* IR objective positioned over the sample. *b)* Image of the focused laser beam over the graphene channel of an RF device

3. **Electrical measurement:** The RF samples are contacted by coplanar RF probes (67 GHz) (figure 2.13). The RF probes, as well as the MZM, are connected to a 67 GHz, four-port Vector Signal Analyzer (VNA). Typically, 3 of the four ports are used in our measurements. The first and second ports are connected to the graphene CPWs, to measure the RF response of the devices. The third port is used as a signal generator and is connected to the MZM RF input, to modulate the power of the optical beam (see figure 2.10).

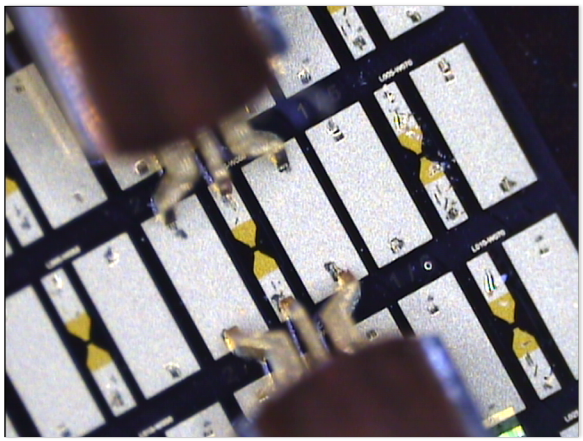

Fig. 2.13 RF device contacted by RF probes

.

2.2.3.2 High-frequency optoelectronic measurement methods

To characterize the high-frequency devices we have measured the S-parameters, and performed photodetection and optoelectronic mixing experiments.

S-Parameters measurement S-parameter measurements where performed on the RF devices in order to evaluate the electrical performances as a function of frequency. Here, we present an overview of the S-parameter measurement principle. An exhaustive development of this technique can be found in [30]. Figure 2.14 represents a 2-port electrical network. The expressions of the voltage and current waves traveling through the port i (i=[1,2]) have the general expression:

$$V_i(z) = V_i^+ e^{j\beta_i z} + V_i^- e^{-j\beta_i z} \tag{2.4a}$$

$$I_i(z) = I_i^+ e^{j\beta_i z} + I_i^- e^{-j\beta_i z} = \frac{V_i^+}{Z_{0i}} e^{j\beta_i z} - \frac{V_i^-}{Z_{0i}} e^{-j\beta_i z} \tag{2.4b}$$

Where V_i^+ and I_i^+ are the incident voltage and current waves amplitudes at the port i, V_i^- and I_i^- are the reflected voltage and current waves amplitudes at the port i, β_i is the propagation constant and Z_{0i} is the impedance of the transmission line connected to the port

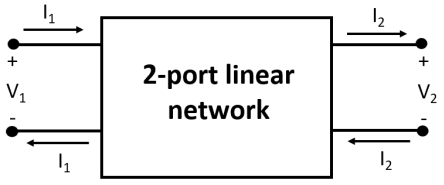

Fig. 2.14 2-port linear network representation

.

i. This impedance is often equal to 50 Ω, as in our case.
We now define the normalized incident and reflected waves at the port i as:

$$a_i = \frac{V_i^+}{\sqrt{Z_{0i}}} = I_i^+ \sqrt{Z_{0i}} \tag{2.5a}$$

$$b_i = \frac{V_i^-}{\sqrt{Z_{0i}}} = -I_i^- \sqrt{Z_{0i}} \tag{2.5b}$$

The square of these two quantities corresponds, respectively, to the incident and reflected power waves at the port i. The Scattering matrix is defined starting from 2.5a and 2.5b. For a 2-port network, in particular, one can write:

$$\begin{pmatrix} b_1 \\ b_2 \end{pmatrix} = \begin{pmatrix} S_{11} & S_{12} \\ S_{21} & S_{22} \end{pmatrix} \begin{pmatrix} a_1 \\ a_2 \end{pmatrix} \tag{2.6}$$

A generic element of the S-matrix is then naturally defined as:

$$S_{ij} = \frac{b_i}{a_j}\Big|_{a_k=0 \quad \forall k \neq j} \tag{2.7}$$

The measurement of the S-parameters will be used in this work for different purposes that will be developed case by case in the text.

Photodetection In order to measure the frequency response of the fabricated photodetectors, a MZM is used to modulate an optical beam generated by a 1.55 μm DFB laser. It has two electrical inputs, one optical input and an optical output. One of the two electrical input is used to bias the MZM with a DC voltage. The DC bias sets the working point of the MZM. As shown in figure 2.15, the optical output of the MZM follows a sinusoidal law as a function of the DC voltage. In the point $V_{\pi/2}$, one half of the optical input power is transferred at the output, while in the point V_π, a very small portion of the optical input is transferred to the output. When biased at this point, the MZM is operated in the double sideband-suppressed carrier (DSB-SC) mode [31].

A sinusoidal signal of frequency f_{MZM} is generated from one of the ports of the VNA and is applied to the RF electrical input of the MZM, which operates in the DSB-SC mode. The

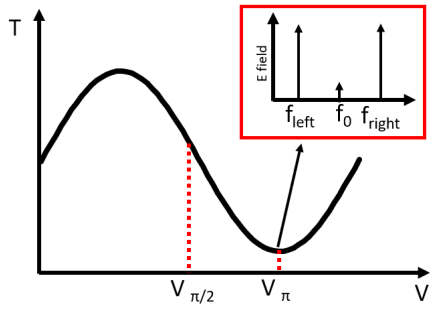

Fig. 2.15 MZM output power characteristics. In the inset, the optical spectrum of the MZM output when operated in DSB-SC mode with an electrical input signal f_{MZM}

.

resulting optical spectrum is shown in the inset of figure 2.15. The central peak (in our case at 1.55 μm) is almost suppressed, and two peaks appear at a frequency offset f_{MZM} from the optical carrier. The left sideband peak is centered at $f_{left} = f_0 - f_{MZM}$ and the right sideband peak is centered at $f_{right} = f_0 + f_{MZM}$, where f_0 is the optical carrier frequency (which is the optical frequency of the CW laser being modulated). If the peak at f_0 is small enough, it can be neglected, and the expression of the two-tone optical field at the output of the MZM can be written as:

$$E_{opt} = Ee^{i2\pi f_{left}t} + Ee^{i2\pi f_{right}t} \tag{2.8}$$

The instantaneous power is proportional to the square modulus of the field:

$$P_{tot} \propto \mid E_{opt} \mid^2 = E_{opt}E^*_{opt} = P_{opt} + P_{opt}cos(2\pi(f_{right} - f_{left})t) \tag{2.9}$$

Where $P_{opt} = 2E^2$.
The power P_{tot} at the output of the MZM in the DSB-SC mode is low. So, an EDFA is employed to amplify the signal.
The amplified optical signal is then focused on the channel of the graphene coplanar waveguide (gCPW). The two sides of the device are connected to two ports of the VNA by means of two RF probes. A DC voltage V_{DC} is applied between the two sides of the gCPW by means of a SMU that is connected to the VNA ports with a bias tee integrated in the VNA itself. The light focused on the graphene channel generates a photoresponse signal. This signal is detected by observing the wave b_i at one of the two ports connected to the gCPW.
A photodetector carries out a quadratic detection of the incident optical field, so generating a current proportional to the instantaneous optical power, which has the expression written in equation 2.9. Moreover, we can note that $(f_{right} - f_{left}) = 2f_{MZM}$. This frequency will be denoted next in the text as f_{opt}. We can then write the expression of the photocurrent

generated by an ideal photodetector as:

$$I_{Photo} = \eta P_{opt} + \eta P_{opt} cos(2\pi f_{opt} t) \tag{2.10}$$

For a real photodetector, η is frequency dependent. For our gCPW, as shown in Section 4.1, it depends also on the DC voltage V_{DC} applied between the two sides of the gCPW. By sweeping the frequency f_{MZM} (and so consequently f_{opt}) and by observing the incoming wave in the ports connected to the gCPW under test, the frequency response of our device can be measured. f_{MZM} is generally swept from 1 to 33.5 GHz. Thus, the frequency dependent photodetection performances of the gCPW can be probed in a range f_{opt} between 2 and 67 GHz.
Photoresponse measurements have been performed even on DC devices, in particular on four-probe structures. The setup is simpler, and is described in Chapter 5.

Optoelectronic mixing An electronic mixer is a three-port device. Two of the three ports are input ports. The resulting output in the third port is the mixing product between the two input signals. An optoelectronic mixer is a similar device. The substantial difference with an electrical mixer is that one of the two electrical input signals is replaced by an optical one. This optical signal is modulated, in general, in the microwave range. The modulation of the optical signal is photodetected by the optoelectronic mixer and then mixed with an electrical signal injected in the electrical input port of the device. So, the resulting output is the mixing product between a photodetected signal and an electrical one.
The measurement of an optoelectronic mixer is done with a similar set-up used for the photodetection measurement. In particular, for the the optical part, a laser beam modulated at high-frequency (f_{opt}) is focused on the channel of the gCPW, using the same set-up described in the previous Section (Paragraph 2.2.3.2). But now, instead of just DC biasing the two sides of the gCPW, we add in one of the two port an electrical signal at frequency f_{ele}, as shown in figure 2.16. The other port of the gCPW is then the output of the optoelectronic mixer.
At the output, we can measure the up ($f_{opt} + f_{ele}$) or down ($|f_{opt} - f_{ele}|$) converted frequency resulting from the mixing product. A quantitative description of how this two signals are obtained after mixing is carried in Section 4.1. For example, if the two signals are sinusoids at frequency f_{opt} and f_{ele}, the typical spectrum at the output port is the one showed in the inset of figure 2.16, on the right. This spectrum can be obtained by measuring the signal at the output port of the gCPW connected to a spectrum analyzer. In general, one of the two inputs is called Local Oscillator (LO), and the other is called RF input. The converted frequencies $f_{LO} - f_{RF}$ and $f_{LO} + f_{RF}$ are called intermediate frequencies (IF). In this work we focused on the downconverted frequency. We will consider as LO the optical signal, and as RF the electrical signal. The power downconversion efficiency of a mixer at the intermediate

frequency IF=$f_{LO} - f_{RF}$ is:

$$P_{eff}(IF) = \frac{P_{IF}}{P_{RF}} \tag{2.11}$$

This quantity can be experimentally extracted by measuring the amplitude of the downconverted peak power and dividing it by the electrical power injected in the gCPW. In order to obtain a frequency dependence of P_{eff}, this procedure has to be done for a sufficient number of frequencies $f_{IF} = f_{LO} - F_{RF}$, by sweeping the RF frequency. An accurate calibration of instruments and cables power losses as a function of the frequency window of interest has to be carried on. The process of frequency sweeping as well as the power calibration is easily done thanks to a measurement function implemented in the VNA for the measurement of mixers.

The four ports of the VNA are independent and can be used to deliver a certain amount

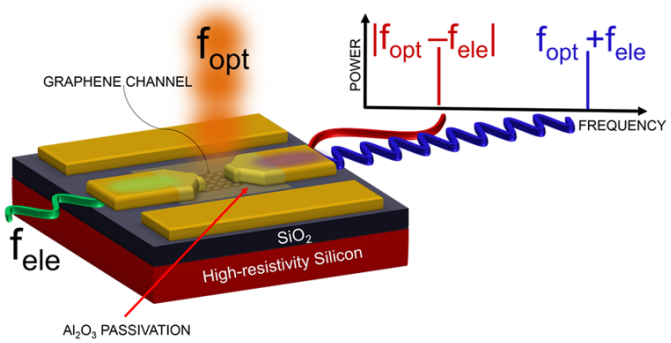

Fig. 2.16 Picture of the gCPW used as a mixer

.

of electrical power a_i as well as to measure a wave b_i. So, in order to measure the mixer response at all the frequencies of interest, the port number 3 is set to generate a single frequency $f_{LO}/2$. This signal is used to drive the MZM and to generate the LO frequency, the port number 1 generates an RF wave a_1 that is swept between f_{RF_1} and f_{RF_2} and is delivered to one side of the gCPW, and port number 2 is connected to the other side of the gCPW and is used to measure the signal b_2 between the frequencies f_{IF_1} and f_{IF_2}, where $f_{IF_1} = f_{LO} - f_{RF_2}$ and $f_{IF_2} = f_{LO} - f_{RF_1}$. In order to obtain the mixer downconversion efficiency over the whole IF range, it is sufficient to measure in the VNA the ratio $\frac{b_2^2}{a_1^2}$. To guarantee an error-free measurement, the VNA internal losses as well as the cables and probes losses are corrected prior to the measurement through a power correction procedure [32]. This leads to a more accurate measurement with respect to the one done employing a signal generator plus a spectrum analyzer.

Chapter 3

Technological process evaluation

As discussed in Chapter 2, two different DC devices (TLM and four-probe) have been designed in order to evaluate the technological process. This Chapter is dedicated to the presentation of the experimental results obtained from the measurement of these devices.
The Chapter starts with some considerations on the robustness of the TLM measurement and the four-probe method for the extraction of contact resistance. Then, two methods for the extraction of the mobility are discussed and compared. We defined three figures of merit to evaluate the technological process: carrier mobility, residual doping and contact resistances. This methodology allowed us to analyze the impact of the technological process on the device performances. The best technological process was used to fabricate a 2" wafer containing RF and hundreds of DC devices. Based on these DC devices, we performed a statistical analysis of the three figures of merit over the whole 2" wafer.
The last part of the Chapter is dedicated to the experimental results obtained by performing low-frequency optoelectronic measurements on the four-probe devices. These measurements show the impact of the contact resistance and mobility on the performances of the responsivity of biased graphene photodetectors.

3.1 Choice of the measurement and parameters extraction methods

In Chapter 1, we pointed out that the charge carrier mobility in graphene can reach extraordinary high values. This leads to the possibility of fabricating very fast devices. But the actual value strongly depends on several factors such as the graphene quality, the choice of the dielectric materials on which the graphene layer is transferred, and the technological process [33–35]. Moreover, graphene-based devices suffer from a high contact resistance value [36, 37], that limits both DC and RF performances [38]. Another parameter to be monitored after device fabrication is the residual doping level of graphene, which importantly influences the photoresponse (cfr Chapter 1). For these reasons, it is essential to measure the residual

carrier concentration, the carrier mobility and the contact resistance after device fabrication. Kim et al. [39] have shown that these parameters can be determined when the graphene channel is integrated in a dual-gated field effect transistor, assuming a constant carrier mobility. The top-gate characteristics (with constant back gate and thus constant contact resistance) can then be fitted to extract the field effect carrier mobility. Then, the back-gate characteristics allow to determine the contact resistance as a function of the back gate voltage. However, with the back-gated two-contact RF devices that we use, the back voltage modifies both channel resistance and the two contact resistances. Thus an accurate extraction of those three parameters cannot be performed.

For this reason, TLM and four-probe measurements were done. These two measurement methods are described in Chapter 2. For TLM devices, four consequent channels of different length are measured, and the contact resistance is extracted from a linear fit of the measured resistances as a function of the channel length, as described in figure 2.8b. This measurement supposes that the contact resistance value is identical for each graphene-metal contact of the four channels. With four-probe measurement, the sum of the two contact resistances of one single channel is extracted following the formula 2.2. The experimental results and the discussion on the extraction of the contact resistance and mobility is presented in this section.

3.1.1 Comparison of the DC methods for contact resistance extraction

TLM measurements Figure 3.1a shows the sequential measurement of the current flowing on four consequent channels of a TLM structure, as a function of the gate voltage. As can be seen, the charge neutrality point voltage is not the same for the four channels. In order to properly extract the contact resistance, the four curves have to be aligned along the charge neutrality point voltages, which are indicated with red crosses on figure 3.1a. Therefore, only TLM structures on which the Dirac point voltage is observable on all the four channels allow to accurately extract the contact resistance of one device. For example, figure 3.1b shows a measurement on a TLM device in which the channels with length L=20μm and L=10μm have a high residual doping, and the Dirac point voltage is higher than the limit of the measurement equipment (200 V). Therefore, this device cannot be used to precisely determine the contact resistance. This drastically reduces the statistical population: the square n. 18 of the sample GRF25 (see Appendix B for details) contains 83 devices, but the measurement of the charge neutrality point voltage of all the four channels was possible only on 2 devices.

To estimate an average contact resistance among all the TLM structures, we calculated the average resistance for each channel length of the different TLMs. We first implemented this method for resistance values measured at the charge neutrality point. The corresponding

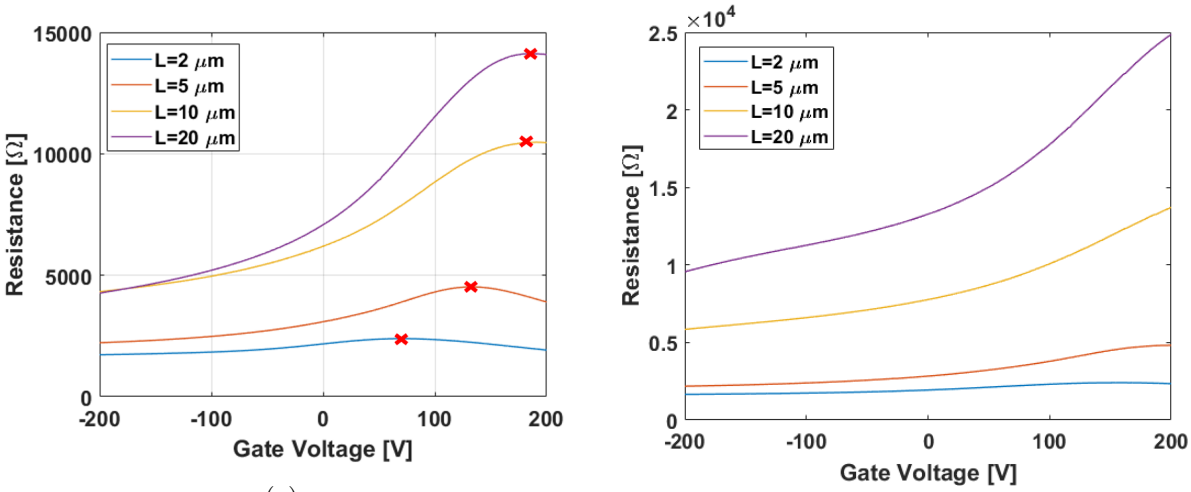

Fig. 3.1 TLM measurements. a) TLM measurement with measurable Dirac point voltage for all the four different lengths. b) TLM measurement with measurable Dirac point voltage only for channel length L= 2,5 μm.

resistances are shown in in figure 3.2. A linear fit has been used to extract the average contact resistance, which has a value of R_C=813Ω. Therefore, the contact resistance value per μm is 2032Ωμm, considering that the channel width of TLM devices is W=5 μm. As will be shown later, this value appears lower with respect to the average value found with the four-probe method. The high dispersion in the measured values, presented in Appendix B, suggests that the estimated value suffers from an important error. Moreover, even if this approach gives an average value of the contact resistance, it cannot be used to extract other parameters, such as carriers mobility, for each device, because the contact resistances of each TLM structure are unknown.

Four probe devices measurements The four-probe measurement technique has been described in Chapter 2. This method relies on the measurement of the graphene resistance without the contact resistance contribution, by reading the voltage drop between two intermediate contacts with a voltmeter, while a current is imposed between the two external contacts. By doing so, the graphene square resistance $R_\square$ is extracted, and mobility and carrier concentrations are calculated.
The contact resistance is extracted by calculating the total channel resistance starting from $R_\square$ and subtracting it from the total resistance measured between the two external contacts. With this method, we were able to get information from a much higher number of devices (323 devices) with respect to the TLM technique. This because all parameters can be measured on each four-probe device. Moreover, in TLM devices, the mobility calculation requires first the contact resistance extraction (that is then subtracted to the total resistance to obtain

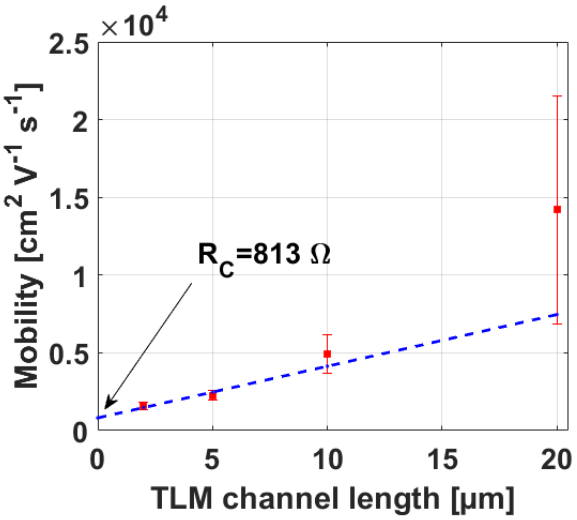

Fig. 3.2 Extraction of the contact resistance with the TLM method. The fit has been done averaging over all the measured population on the wafer, for each channel length

.

$R_{\square}$), while with the four-probe measurement, $R_{\square}$ is directly measured without no need of fit. Since the measured contact resistance exhibits an important dispersion, the four-probe method appears better suited for our analisys.
For these reasons, the four-probe measurement has been chosen to perform the statistical study of our devices. By referring to figure 2.7, the four-probe devices dimensions are l=10 μm, L=24 μm and W= 6 μm.

3.1.2 Mobility calculation

We compared two different methods for the extraction of carriers mobility in graphene. One method relies on the calculation of the transistor transconductance, while the other is based on the fit of the carrier mobility and density values, starting from resistivity measurement.

Mobility extraction from transconductance calculation Considering the formula of a graphene transistor in the linear (triode) region, i.e. when the source-drain voltage is smaller than the saturation voltage, the current flowing along the channel as a function of the gate voltage V_G, far from the Dirac point voltage, can be expressed as [15]:

$$I_{DS}(V_G) = \frac{W}{L}\mu n(V_G) e V_D \tag{3.1}$$

Where W and L are, respectively, the width and length of the transistor, μ is the carrier mobility and $n(V_G) = \frac{C_{ox}V_G}{e}$ is the carrier density. By defining the transistor transconductance

$g_m = \frac{dI_{DS}}{dV_G}$, the mobility can be expressed as[1]:

$$\mu_{FE} = g_m \frac{L}{W} \frac{1}{C_{ox} V_D} \tag{3.2}$$

Where FE states for Field-Effect. In general, the peak transconductance is used to calculate μ_{FE} [**40**] as shown in figure 3.3a.

Mobility extraction from fit The square resistance of graphene can be expressed as:

$$R_{\square} = \frac{W}{L} \frac{1}{\sqrt{n_0^2 + n^2(V_G)}\mu e} \tag{3.3}$$

Where n_0 is an effective quantity which represents the charge carrier density at the charge neutrality point. This charge density is due to charges or defects either in graphene or at the graphene/dielectric interface. Then, $n(V_G) = \frac{C_{ox} V_G}{e}$. The mobility is extracted by fitting the $I_{DS}(V_G)$ curve.

Figure 3.3b shows the value of mobility for the 98 four-probe devices contained in the square n. 12 of the sample GRF 25 (cfr. Appendix B).
The blue curve represents the mobility value extracted from the transconductance calculation, while the red one is the mobility obtained by fitting the resistivity curve of the devices. As can be seen, the two methods give very close values for each device. Nevertheless, for some devices, it was not possible to calculate the mobility with the fitting method. This because the Dirac point voltage was higher than the maximum voltage which could be delivered by our SMU, and so the value of n_0, essential for the fit, could not be extracted. Moreover, the fit method gives sometimes not accurate values, which overestimate the actual mobility. For example the fitted mobility obtained for the device indicated by the res arrow in figure 3.3b is more than three times higher than the one obtained with the field effect mobility method on the same device. The inset shows that the square resistance obtained using the fitted mobility (red dashed) is in this case very different from the measured one (red continuous). For these reasons, the statistics have been performed using the transconductance method.

3.2 Experimental results

In this section we present the experimental results. We evaluated different variants of the technological process presented in Chapter 2. We individuated the best technology and fabricated a 2" wafer containing different RF devices and hundreds of four-probe structures.

[1]It has to be noticed that this formula is valid when the Fermi level is far from the Dirac point, where the charge carrier concentration n induced by the gate voltage is much higher than the residual charge carrier density n_0. This quantity will be introduced in the next lines of the text

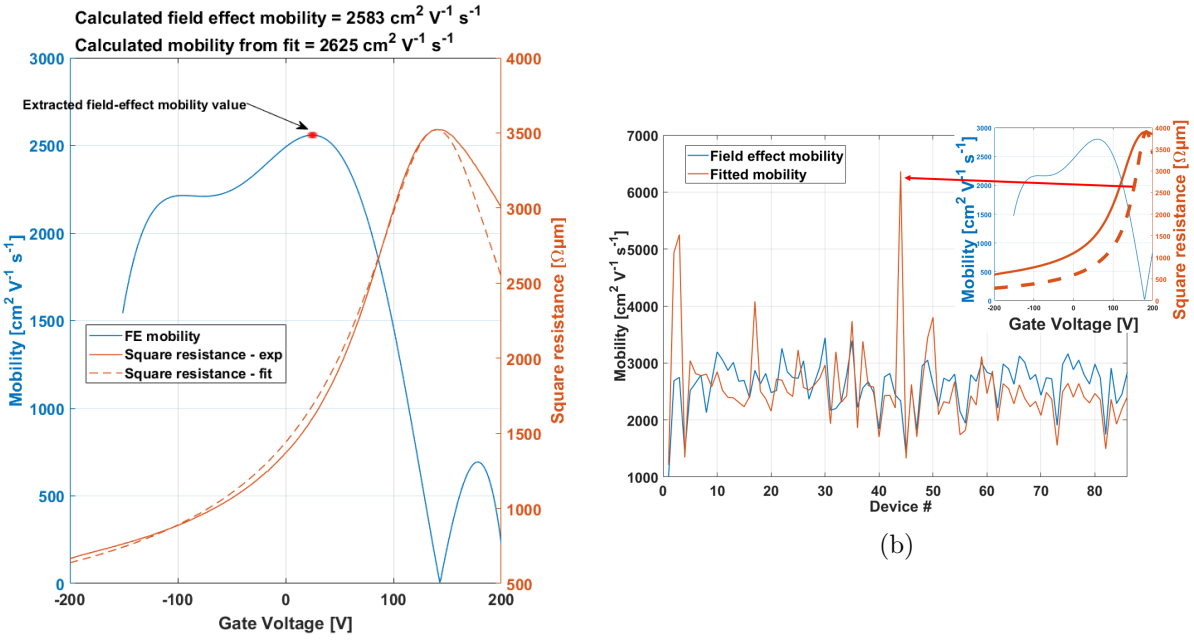

(a) (b)

Fig. 3.3 Mobility extraction. a) Example of the extraction of the mobility using the filed effect mobility extraction method and the fit of the conductivity curve. The red point on the blue line is the value of mobility extracted with the filed effect extraction method. The red dashed curve is the model calculated extracting the mobility and the residual doping starting from the fit of the conductivity. b) mobility values extracted using the two methods, for a population of 98 devices. The conductivity fit method gives sometimes erroneous values of mobility, as indicated in the inset, where the model (red dashed line) doesn't fit with the measurement (red continuous line).

Table 3.1 Summary of the samples characteristics for the technological process preliminary study

Device name	**Protection Layer**	**Thermal treatment**	**Passivation Layer**
GRF20	Yes	UHV 250° 1h	Yes
GRF21	No	No	Yes
GRF22	Yes	No	Yes

Table 3.2 Average mobility of the devices in the different samples, that have been fabricated using different technological process, summarized in Table 3.1. The average mobility is reported before and after the deposition by ALD of a 30 nm thick Al_2O_3 film on the fabricated devices.

Device name	**mobility before passivation**	**mobility after passivation**
GRF20	996 $cm^2/(V{\cdot}s)$	1849 $cm^2/(V{\cdot}s)$
GRF21	371 $cm^2/(V{\cdot}s)$	879 $cm^2/(V{\cdot}s)$
GRF22	535 $cm^2/(V{\cdot}s)$	1591 $cm^2/(V{\cdot}s)$

From these four-probe structures the statistics of the key parameters for the new wafer have been obtained.

3.2.1 Preliminary study

Table 3.1 summarizes the differences in the technology used for three different samples containing four-probe structures.

Sample GRF21 did not integrate the protection layer[2]. The other two samples, GRF20 and GRF22 integrated a protection layer. Moreover, sample GRF20 undergone an UHV anneal at 250°, just before the deposition of the protection layer. The measured carrier mobility values for the three samples are listed in the first column of table. 3.2 (*mobility before passivation*).

In a second time, a passivation layer was deposited by ALD on all the samples (see Chapter 2). A second measurement was then performed. The results of the mobility are shown in the second column of table 3.2 (*mobility after passivation*).

It can be noticed that sample GRF21 (which does not integrate any protection/passivation layer) reports the worst mobility values. Moreover, a thermal annealing performed just before the Al_2O_3 protection layer deposition improves the performances.

As a conclusion for the preliminary study, we determined a technological process which allowed us to fabricate graphene devices exhibiting a good carrier mobility. This process integrates a thermal anneal of the transferred graphene film, a protection layer realized before the lithographic process and an Al_2O_3 passivation layer deposited after the device fabrication [21, 41].

[2] As detailed in 2.1.2, the protection layer is a 1 nm thick aluminium layer that is subsequently oxydised in air. It is deposited after graphene transfer and before any lithography process.

3.2.2 Final study

A 2" wafer (named GRF25) was finally fabricated, following the technological process used for the sample GRF20. A photo of the sample is shown in figure 3.4. The detailed description of the devices location on the sample can be found in Appendix B. Here, the four-probe measurements are presented. In figure 3.4, the 6 squares containing four-probe structures have been highlighted with red circles. Table 3.3 details the number of devices for each square, as well as the number of functioning devices[3]. The third column shows the number of devices for which the Dirac point voltage was visible[4]. This corresponds to a residual doping of less than $2.16 \cdot 10^{12}$ cm^{-2}.

The contact resistances have been calculated for each device. Figure 3.5 shows the map

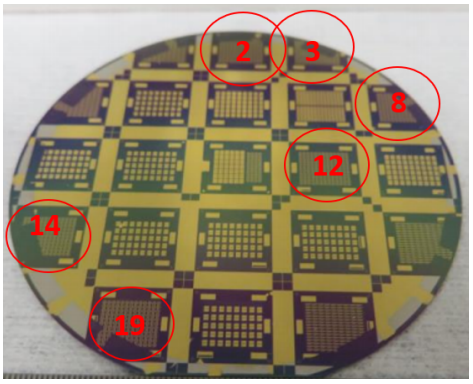

Fig. 3.4 2" fabricated wafer. squares with four-probe devices are highlighted with red circles

.

of the contact resistances value for each probed square, taken at high electrostatic doping. The mobility values for each square are represented in figure 3.6. Both contact resistance and mobility have been calculated only for the functioning devices population. Figure 3.7 shows the residual doping values, the values have been taken only on the devices for which the Dirac point voltage was visible. The other devices are marked in red, and have a residual doping higher than $2.16 \cdot 10^{12}$ cm^{-2}.

In total, 555 devices have been tested. 323 of them where functional, corresponding to the 58.2 % of the entire statistical population. Among the functional devices, on 170 we where able to measure the Dirac point voltage. This corresponds to the 30.6 % of devices having a residual doping of less than $2.16 \cdot 10^{12}$ cm^{-2}. The total statistics for the contact resistance at the Dirac point voltage is shown in figure 3.8a, while in figure 3.8b is shown the histogram of the contact resistance distribution. The mean value for the contact resistance is 14.96 k$\Omega\mu$m at the charge neutrality point, while at high doping is 10.95 k$\Omega\mu$m. The contact resistance

[3]We define a "functioning device" a device exhibiting current along the graphene channel, for which the two internal contacts for the four-probe measurement work properly.

[4]The Dirac point voltage was visible if it was in the range [-200,200] V, that was the measurement limit of our instrumentation, as alreasdy pointed out before in this Chapter

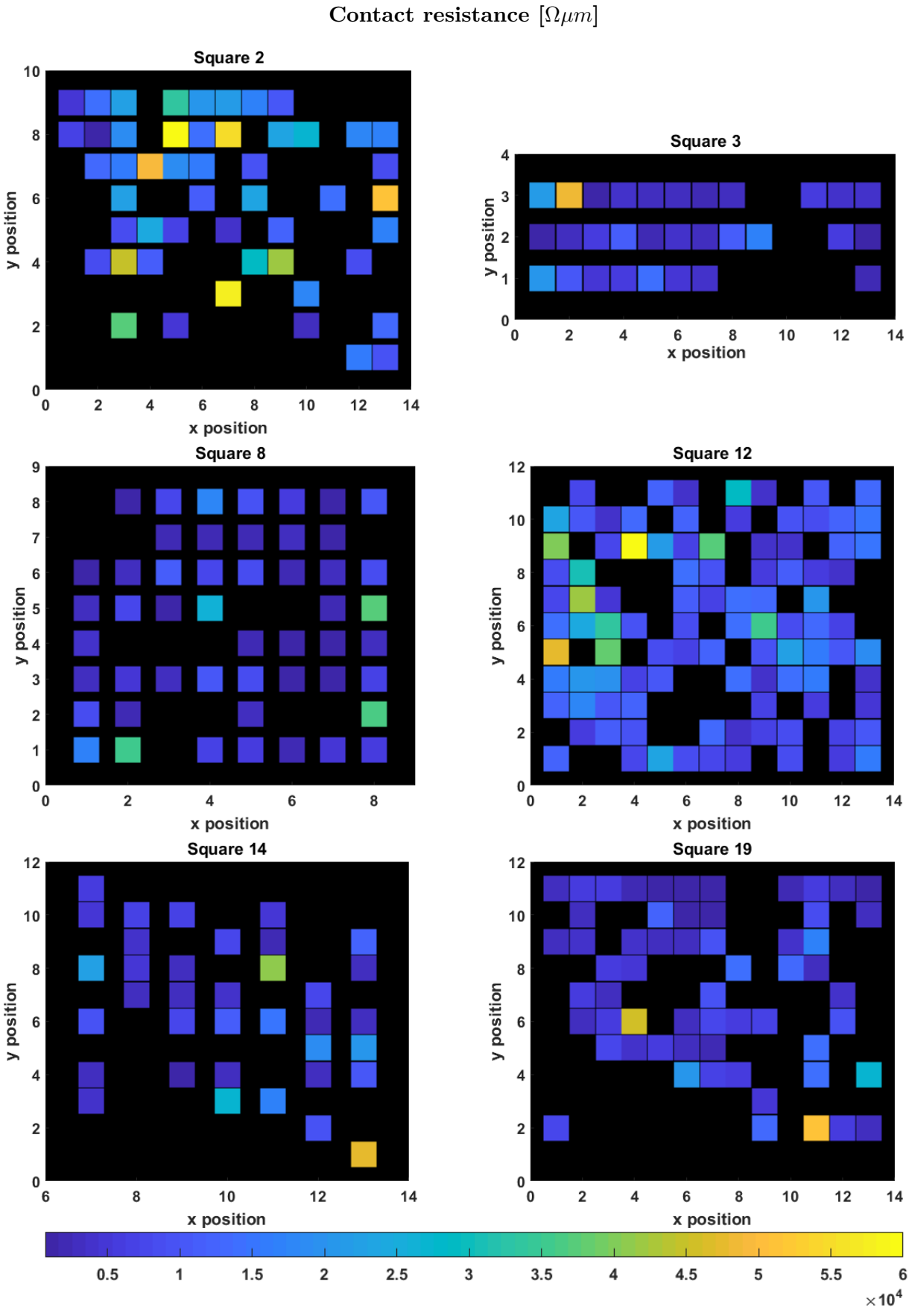

Fig. 3.5 Contact resistance map

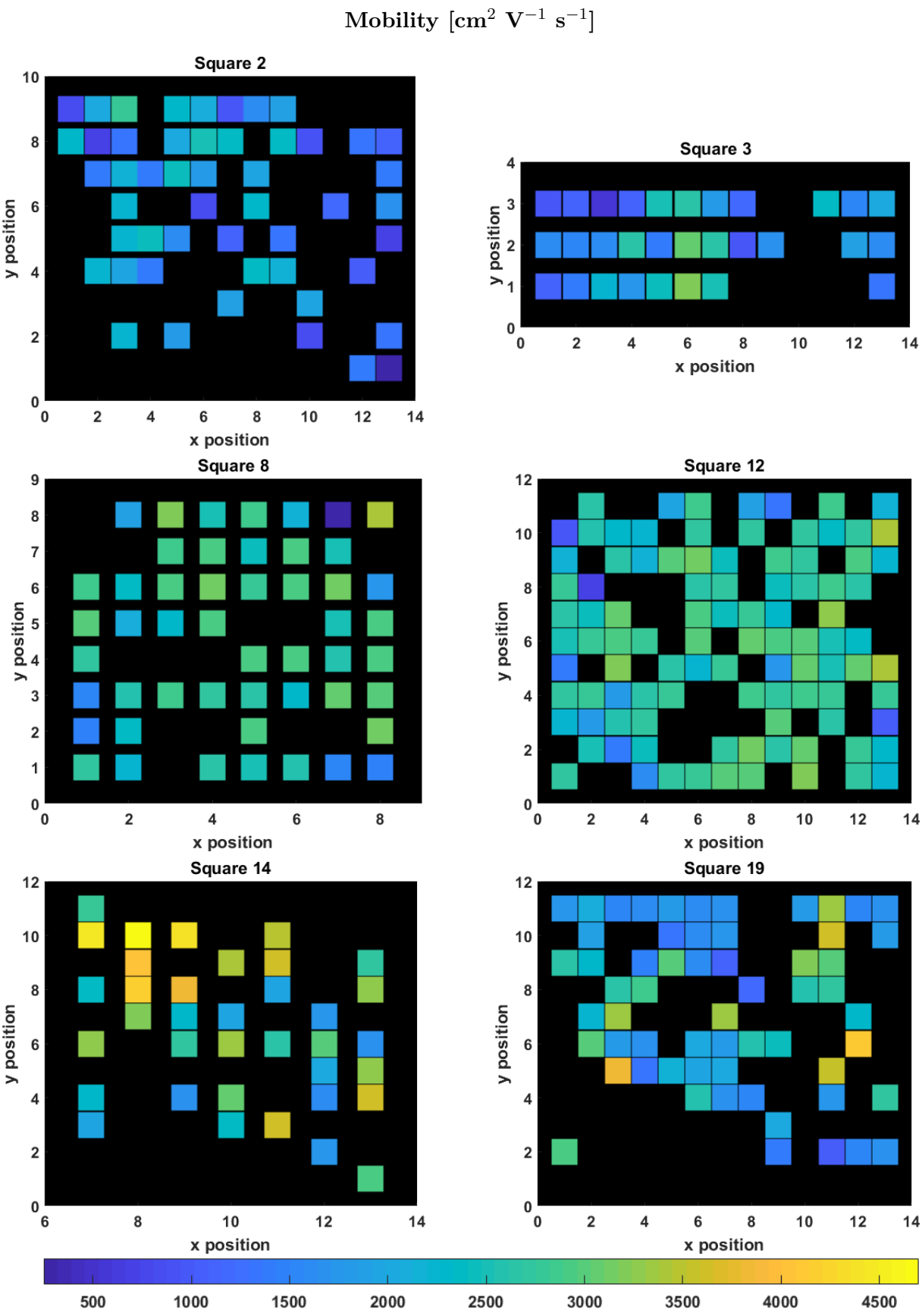

Fig. 3.6 Mobility map

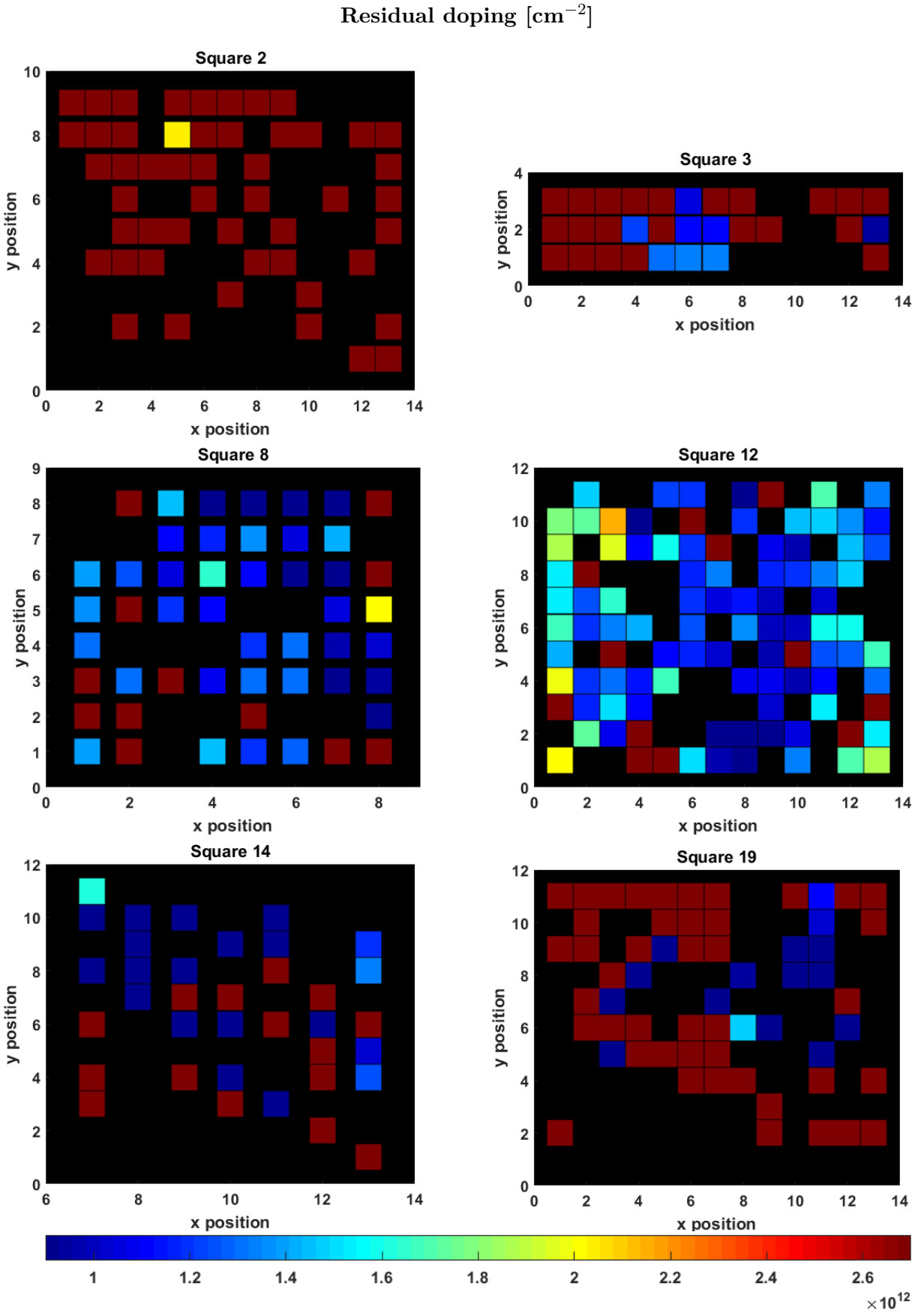

Fig. 3.7 Residual doping map

Table 3.3 Summary of the number of devices that have been tested for each square. The second column shows the number of functioning devices, while the third one shows the number of devices on which the Dirac point voltage was measurable (<200V). The percentage is referred to the total number of devices present in the squares (first column)

Square #	**Total # of devices**	**Functioning devices**	**Dirac point**
2	117	50 *(42.7%)*	1 *(0.9%)*
3	39	30 *(76.9%)*	8 *(20.5%)*
8	64	50 *(78.13%)*	38 *(59.4%)*
12	143	98 *(68.5%)*	86 *(60.1%)*
14	77	36 *(46.8%)*	21 *(27.3%)*
19	115	59 *(51.3%)*	16 *(13.9%)*
Total	**555**	**323 *(58.2%)***	**170 *(30.6%)***

value is lower than 5 kΩ for the 29% of the devices at the charge neutrality point, and for 28.3% of the devices at high doping. The mobility distribution (figure 3.8c) was extracted from the entire population of the working devices, since its extraction didn't require the visibility of the Dirac point voltage.

The measured mobility values are in line with the expectations for graphene on SiO_2[42]. The residual doping also is in good agreement with our previous works[21, 41]. However, the contact resistance average value remains high.

3.2.3 Impact of the key parameters on photodetection

As shown in the previous Sections, four-probe devices allow to eliminate the contact resistance contribution from the measurement of the resistivity of the graphene channel. It is so interesting to use this approach to extract the intrinsic responsivity of graphene used as active material for photodetection, in order to valuate the impact of contact resistance and mobility on the performances. To do so, we characterized 18 four-probe structures. Figure 3.9a shows a scheme of the measurement: a 1.55 μm laser beam, modulated at 700 Hz by means of a chopper, was focused in the center of the graphene channel. The optical power of the laser before modulation was set to 60 mW. So, the modulated part of the optical power was 30 mW. By doing so, the conductivity of the portion of the channel on which the light was present was changed. Then, a constant voltage V_{AB}=2V was applied between the external contacts A and B. The change in conductivity $\Delta\sigma = \sigma_{light} - \sigma_{dark}$[5] induced by the illumination of the four-probe device internal region (contacted by the contacts indicated with the letters C and D) was measured by means of a lock-in amplifier which was connected to the internal probes and synchronized to the optical chopper modulating frequency. At

[5] σ_{light} is the conductivity of the graphene channel under illumination, σ_{dark} is the conductivity of the channel under dark conditions

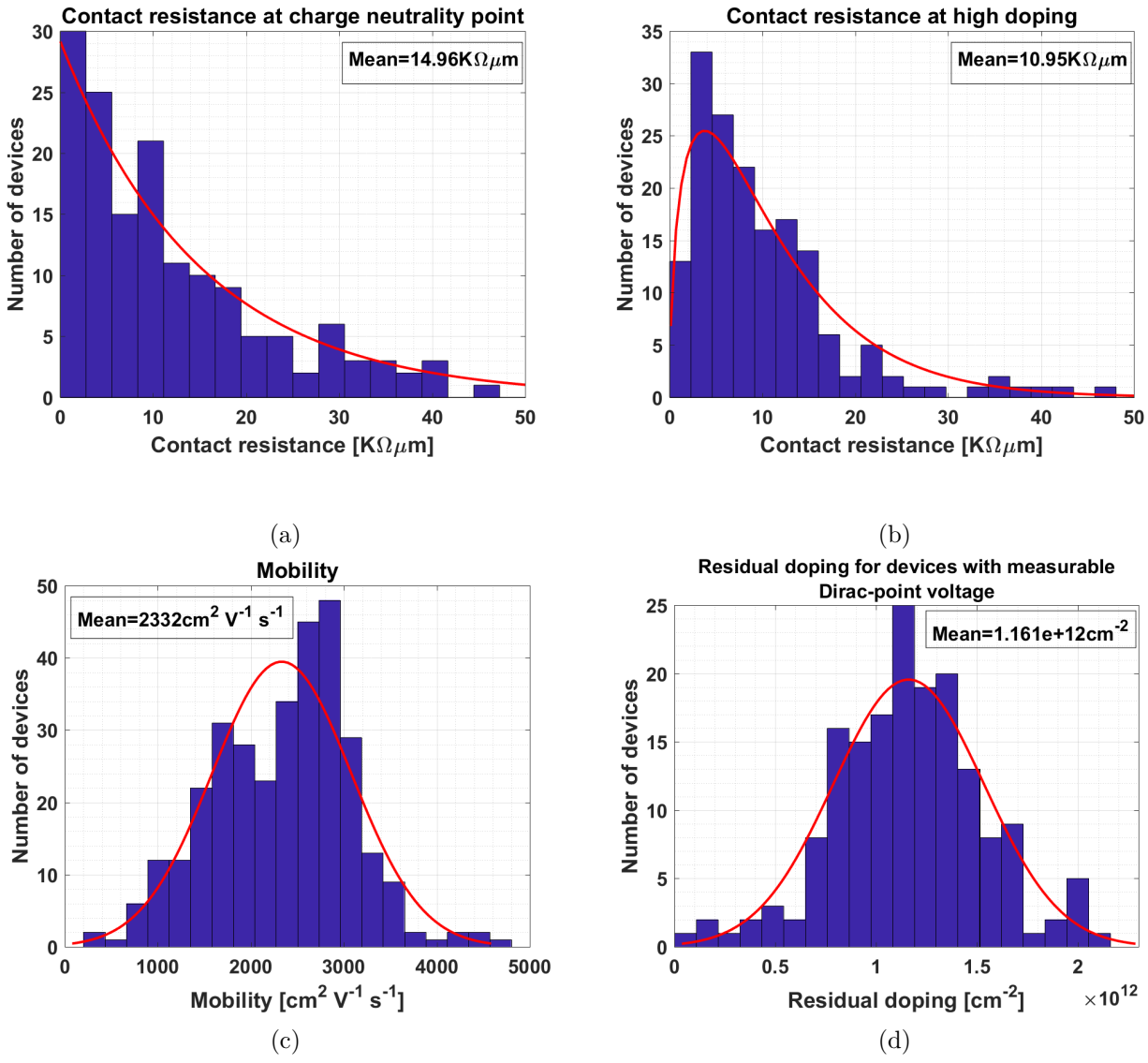

Fig. 3.8 Total statistics of the measured DC key performance parameters

the same time, we measured the constant DC voltage drop along the internal region. The details of the change in conductivity ($\Delta\sigma$) extraction are discussed in Appendix C. The plot

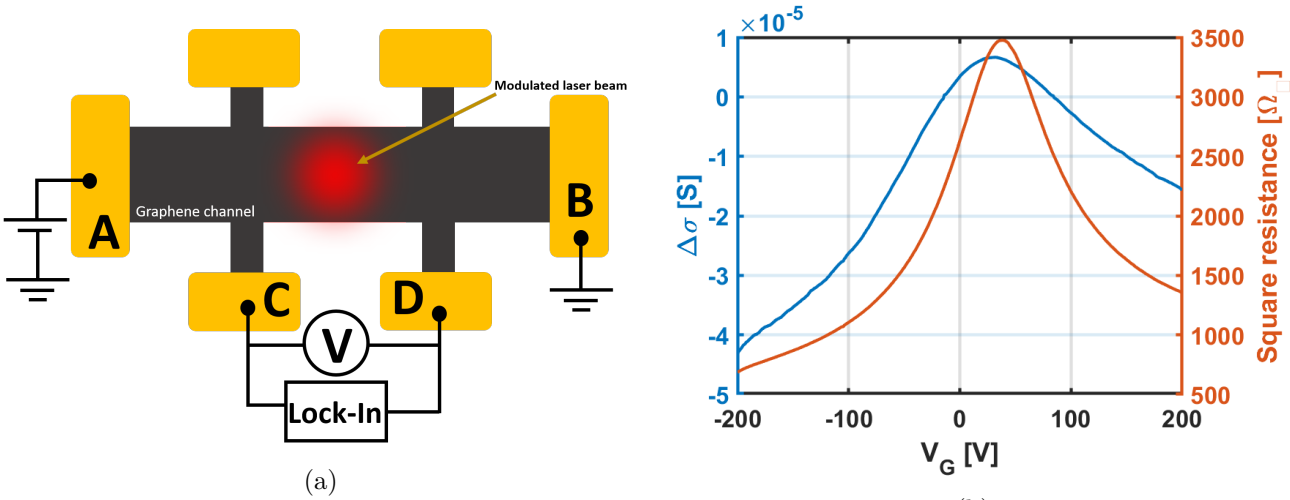

(a) (b)

Fig. 3.9 a)Experimental scheme for change in conductivity measurement on a four-probe structure. b) Blue curve: change in conductivity induced by the laser excitation. Red curve: extracted square resistance of the graphene sheet. The measurement has been obtained under a voltage bias between the two external contacts $V_{AB} = 2$ V, with a modulated optical power of 30 mW

in figure 3.9b shows Δ_σ as a function of the back-gate voltage. We observed the change in conductivity discussed in Chapter 1: near the Dirac point voltage, a positive change takes place. This is attributed to an increase of charge carrier concentration (*photoconductive behaviour*) [19, 20]. At high doping, the change in conductivity becomes negative. This is attributed to a decrease of the carrier mobility [3, 20] (*bolometric behaviour*) and is due to electrons temperature increase induced by the incident radiation.
Δ_σ is plotted against the charge mobility in Figure 3.10 for both bolometric (3.10a) and photoconductive (3.10b) regime. The blue dots correspond to devices having a lower contact resistance value. A clear increase of the conductivity change is observed when the mobility is higher. The dependence Δ_σ on the contact resistance is presented in the insets of figures 3.10a and 3.10b. These results show the importance of reducing the contact resistance and charge carrier mobility: passing from a charge carrier mobility of 1500 $cm^2V^{-1}s^{-1}$ to 4000 $cm^2V^{-1}s^{-1}$, in combination with an improvement of the contact resistance, we measured more than one order of magnitude improvement in the responsivity.

3.2.4 Chapter conclusions

This Chapter has shown the study of some variants of the general technological process described in Chapter 2. This study allowed to determine an optimized fabrication process,

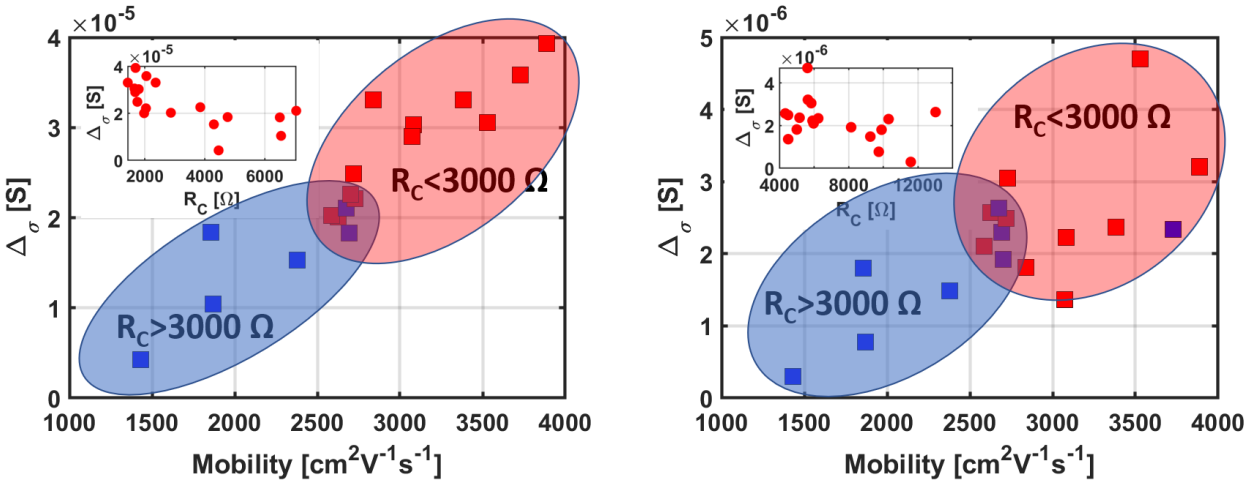

(a) (b)

Fig. 3.10 a) Laser-induced change in conductivity versus carrier mobility at high (a)) and low (b)) electrostatic doping. In the inset, Δ_σ is plotted against the contact resistance

which was used to fabricate a 2" wafer containing numerous devices. On this wafer, a statistical analysis on the key performance figures of merit have been carried out. The results show a good average value for the mobility (2332 $\frac{cm^2}{Vs}$) and the residual doping (1.16 10^{12} cm^{-2}). The value of contact resistance remains still important. Preliminary studies on the use of gold in direct contact with the graphene channel are encouraging and show a reduction of contact resistance. The role of both contact resistance and charge carriers mobility on photodetectors performances is experimentally revealed by low-frequency optoelectronic Graphene-based devices still suffer from a non-negligible dispersion of the key performance parameters. The accurate monitoring of the technological process is only possible if statistical measurements are implemented. In fact, it is hazardous to compare different technological steps if the performances of only a few devices are measured. We think that the effort done during this thesis work in the automation of the measurement system in order to probe a relevant population of devices in a reasonable time has shown the powerfulness of this approach.

Chapter 4

High frequency photodetection and Optoelectronic Mixing based on graphene devices

4.1 Optoelectronic mixing: General principle, motivations and state of the art

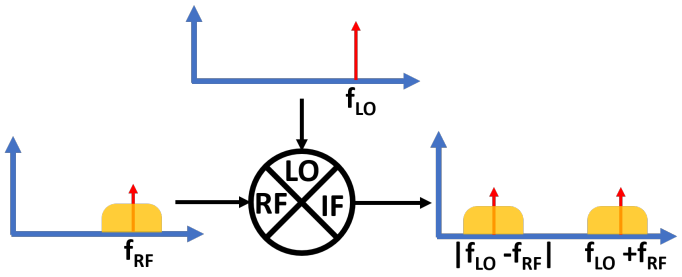

Fig. 4.1 Heterodyne mixing principle

.

One of the most used function in communication systems and signal processing is frequency translation. In several situations, there is the need to shift the information carried around a certain frequency, towards lower or higher frequencies, depending on the application. Heterodyning is a technique that is used to achieve this purpose [43]. It consists in employing a three-port device, called mixer, that is capable of multiplying two input signals, as shown in figure 4.1: a single tone at frequency f_{LO}, called local oscillator, is applied at one of the two input ports of a mixer. The other input receives some information carried around an RF frequency f_{RF}. The result is, as shown in figure 4.1, a shift of the information around

the frequencies $|f_{LO} - f_{RF}|$ (*downconversion*) and $f_{LO} + f_{RF}$(*upconversion*), also called intermediate frequencies (IF).

Electronic mixers for heterodyning are largely used in radio technology. Figure 4.2 shows the block diagram of a radio, including a superheterodyne receiver [44], the most used configuration for implementing hetherodyning technique nowadays. In this example, a tunable LO from 10.55 MHz to 11.7 MHz is multiplied with the signal arriving from an antenna. Many channels are present in the received signal, all centered around a different frequency. If the frequency of the local oscillator is set to f_{LO}= 10 MHz+f_k, the k-*th* channel will be centered around f_{IF}=(10 MHz+f_k)-f_k=10 MHz after mixing. Then a filter centered around 10 MHz is used to filter out all the other channels, so that only the information in the k-*th* channel is sent to the speaker.

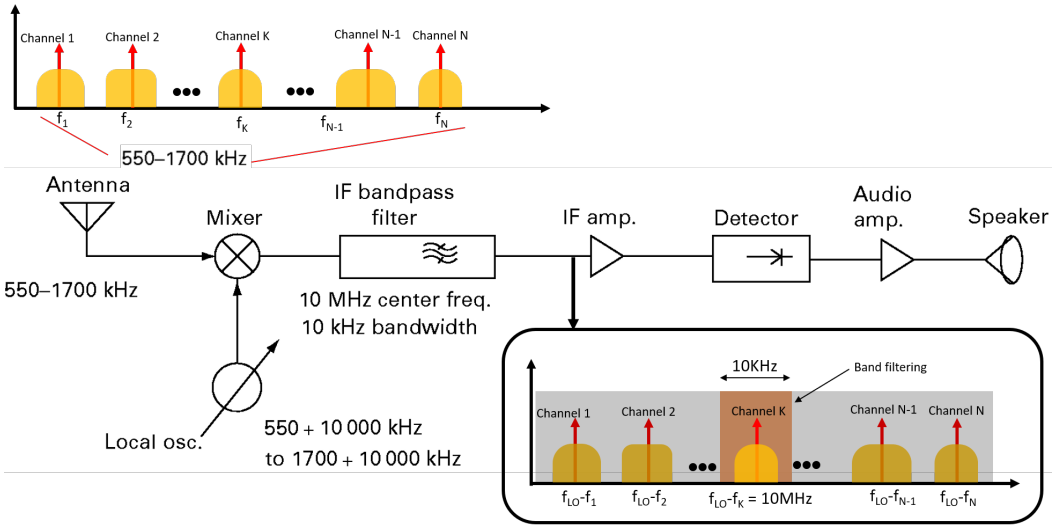

Fig. 4.2 Radio receiver. Adopted from [4]

.

Another remarkable application that uses this technique is RADAR (radio detection and ranging) technology[45, 46]. Figure 4.3 shows a typical block diagram of a RADAR receiver. As can be noticed, it is very similar to the one showed previously. The signal received from the RADAR antenna is amplified by means of a low-noise amplifier (LNA), filtered in the band of interest, and then downconverted by means of an electronic mixer in the operating band of the RADAR receiver electronics.

During the last decades, optical systems have substituted some building blocks that could previously be implemented only with electronic components. This is the case of both the previous examples: the development of optical fibers has revolutionized modern communications, thanks to their high-transmission bandwidth, electromagnetic interference immunity and low transmission loss compared to copper cables [7]. Moreover, the development

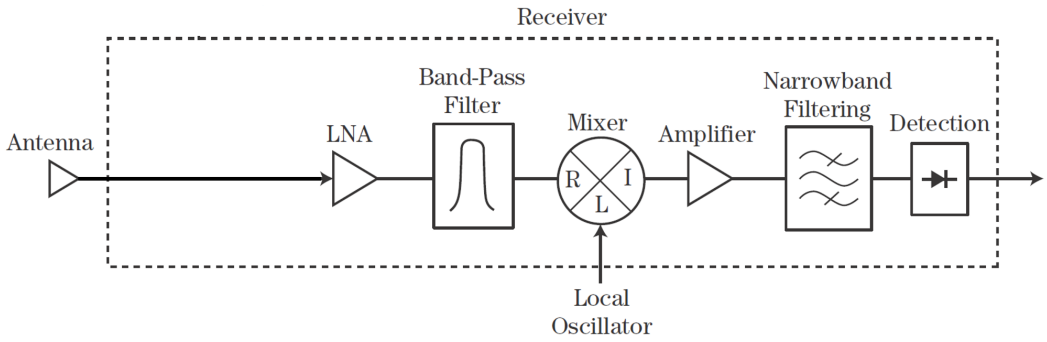

Fig. 4.3 RADAR receiver. Adopted from [5]

.

of lasers opened the possibility to integrate the photonic technology also in RADAR systems [47, 48]. This has led to the development of optoelectronic systems, in which optical and electrical signals are present together. In these systems, components capable to translate the information from the optical domain to the electrical one (and vice versa) are necessary. In particular, photodetectors have the role to transform optical signals in electrical ones. In the following, three examples of RADAR and LADAR (laser detection and ranging) systems that use photonics together with electronics are presented. The three cases share a common configuration: a photodetector is used to translate high frequency signals from the optical to the electrical domain, and then an electronic mixer is employed to translate information to baseband.

Figure 4.4 shows an example of a proposed LIDAR[1]-RADAR system [6] that advantageously uses photonic technology: a two-frequency laser pulse containing 2 optical frequencies ν_1 and ν_2 is sent to the target. The back-scattered light from the target is collected and detected by an RF photodetector. The generated photocurrent containing the information from the target has a modulation close to $f_{mod} = \nu_1 - \nu_2$, generally chosen to be in the RADAR frequency range ([1-10 GHz]), resulting from the quadratic detection of the optical field. The target information that has been converted from the optical to the electrical domain is then downconverted in baseband using an electronic mixer, before being processed.

Another remarkable example [7] is shown in figure 4.5, in which a FM/cw LADAR architecture block diagram is presented: the current driving a laser diode is frequency-modulated by means of a chirp signal (a signal in which the frequency increases or decreases with time). The optical signal is directed to the target. The light that impinges the target is then scattered, collected, and detected by means of a photodiode, that converts the optical signal into a current proportional to the light power. This current has the same waveform than the original one used to modulate the laser, except for the time delay, that represents

[1]LIDAR is the acronym for *light detection and ranging*. The terms LIDAR and LADAR are in practice interchangeable and used as synonims. The *Handbook of Optoelectronics* [49] quotes: *"while some differentiate the usage of the three expressions 'laser radar', 'lidar' and 'ladar', they are in fact generally used freely and interchangeably"*

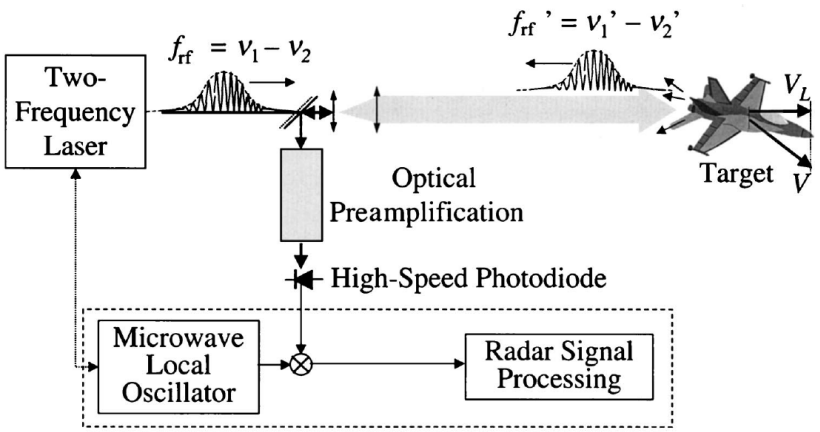

Fig. 4.4 LIDAR-RADAR scheme proposed by [6]

.

the propagation time spent from the optical signal to go from the laser to the target, and then back to the photodetector. After amplification, the photodetected signal is mixed, by means of an electrical mixer, with an undelayed sample of the transmitted chirp waveform [7]. The intermediate frequency has the following expression:

$$f_{IF} = 2\Delta F \frac{\tau}{T} \tag{4.1}$$

where ΔF is the difference between the final frequency and the starting frequency, T is the chirp period and $\tau = D/c$, being D the distance to the target and c the speed of light.

In the first two examples, information comes from the optical part of the system, and an

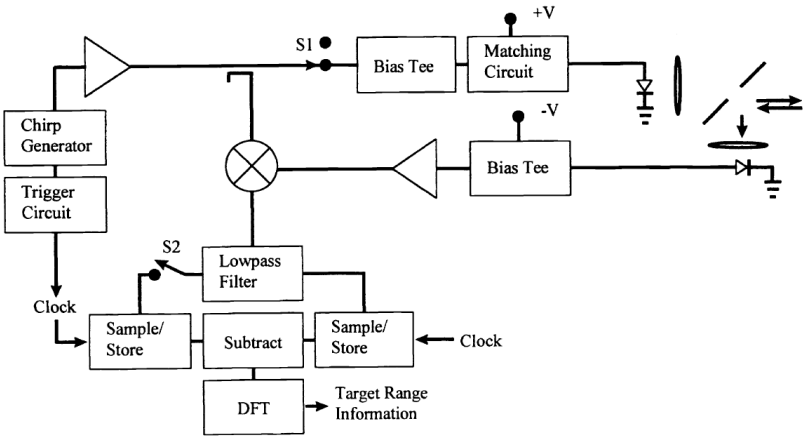

Fig. 4.5 FM/cw LADAR architecture block diagram. Adopted from [7]

.

electronic LO is used for downconversion. There are some applications based on an optical local-oscillator. For example, in phased-array antennas used in RADAR systems, the LO

signal can be advantageously distributed to each antenna using an optical carrier. The optical LO-signal distribution has the advantage of transmitting high-frequency carriers over tens of meters with very low attenuation and electromagnetic immunity. A principle schematic is shown in figure 4.6 [8]. Here, a DFB laser is modulated using a MZM and then amplified with EDFAs and distributed over 64 different cells composing an array. The optical LO is then photodetected by each channel using an high-power photodiode (HPD), before being mixed with the information received by each antenna.

All these examples describe systems in which a photodetector plus an electronic mixer are

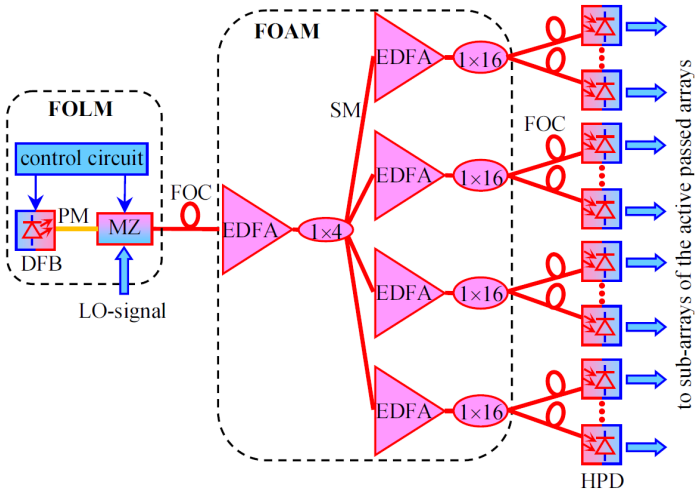

Fig. 4.6 Distribution of an optically carried local oscillator over 64 cells active phased array. Adopted from [8]

.

used in cascade in order to recover the information at the IF frequency of the receiver. In most cases, after detection, it is necessary to use a wide band amplifier before mixing the photodetected signal, as shown in figure 4.7a. In order to limit noise, this amplifier doesn't have in general a high gain.

A different approach makes use of a single component that is capable of providing the photodetection function and the mixing in the same device. Such a kind of device is generally called optoelectronic mixer, or self-mixing detector [7].

Using just one device instead of two allows to reduce costs and increase performances. In figure 4.7b a schematic of a receiver using an optoelectronic mixer is presented. The amplification is done at the IF frequency, after filtering the signal. In this case, an amplifier with lower bandwidth can be used, which allows to have higher gain and lower noise.

An optoelectronic mixer can be seen as a photodetector with some particular characteristics, that will be analyzed in the following. Let's first consider the photocurrent generated in a photodetector being illuminated by light having a certain optical power P. This current is proportional to the optical power itself through the responsivity R of the device ($I_{photo} = R \cdot P$).

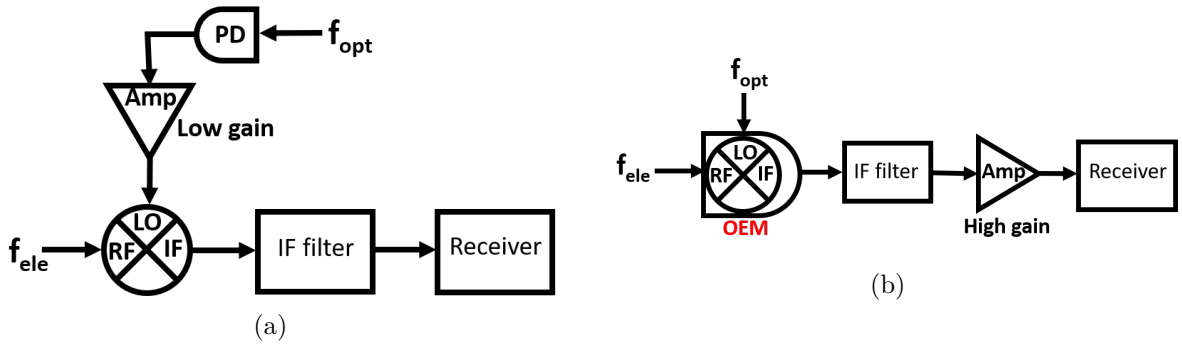

Fig. 4.7 Mix between an optical and an electrical signal using a classical configuration (a)) and an optoelectronic mixer (b))

An optoelectronic mixer is a photodetector whose responsivity R can be modulated by the application of an electrical signal V_{bias}. If the electrical signal is a varying function of time as well as the optical signal, the photocurrent will be:

$$I_{photo}(t) = R(V_{bias}(t)) \cdot P(t) \tag{4.2}$$

Let's consider the case in which the electrical signal that is applied to the device is a sinus with a frequency f_{ele}, and that the optical signal power varies also sinusoidally with a frequency f_{opt}. The expression of the electrical and optical signals have, respectively, the form:

$$V_{bias}(t) = \bar{V_{DC}} + V_m sin(2\pi f_{ele} t + \phi) \tag{4.3a}$$

$$P_{opt}(t) = P_{cw} + P_m sin(2\pi f_{opt} t)) \tag{4.3b}$$

where $\bar{V_{DC}}$ is the bias point of the photodetector around which a a small AC electrical signal of amplitude V_m is applied. In the same way, P_{cw} is the constant optical power, while P_m is the amplitude of the oscillating part of the optical power. ϕ is the phase shift between the two signals.
Following figure 4.8, the expression of $R(V_{bias}(t))$ in the small signal limit is then:

$$R(V_{bias}(t)) = R(\bar{V_{DC}}) + V_m \Delta_R sin(2\pi f_{ele} t + \phi) \tag{4.4}$$

where

$$\Delta_R = \beta(f_{ele}) \frac{dR(V_{DC})}{dV_{DC}}\Big|_{V_{DC}=\bar{V_{DC}}} \tag{4.5}$$

Here, we include a dependence on the injected electrical frequency through a frequency-dependent proportionality constant $\beta(f_{ele})$.

The generated photocurrent is then:

$$I_{photo}(t) = [R(\bar{V_{DC}}) + V_m \Delta_R sin(2\pi f_{ele} t + \phi)] \cdot [P_{cw} + P_{mod} sin(2\pi f_{opt} t))] \tag{4.6}$$

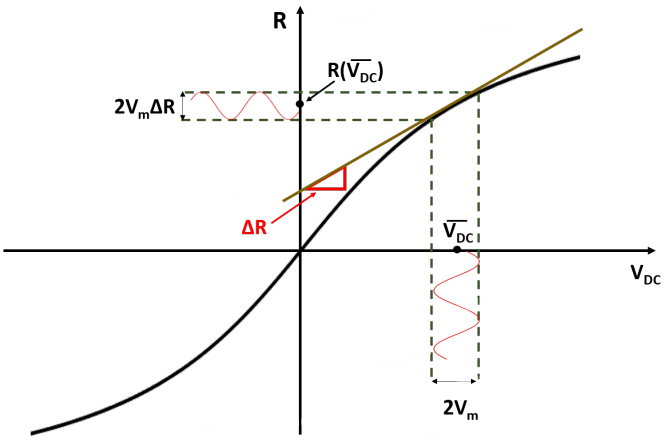

Fig. 4.8 Small signal model used to calculate the time-varying responsivity modulated by an AC signal.

By developing 4.6, one finds:

$$I_{photo}(t) = R(\bar{V_{DC}})P_{cw} + R(\bar{V_{DC}})P_{mod}sin(2\pi f_{opt}) + V_m\Delta_R P_{cw}sin(2\pi f_{ele}t + \phi) + \frac{V_m\Delta_R P_{mod}}{2}[cos(2\pi(f_{ele} - f_{opt})t + \phi) - cos(2\pi(f_{ele} + f_{opt})t + \phi)] \tag{4.7}$$

The equation contains four different terms:

1. The first two terms result from the application of a constant bias. If $V_m = 0$, that is, no electrical varying signal is applied, only these two terms are present. We will refer to this operation mode as *photodetection mode*.

2. The last two terms result from the application of an AC bias. In particular, the last term represents the mixing between the electrical and optical signals. if $V_m \neq 0$ we refer to as *OEM mode*.

Interestingly, if around $V_{DC} = 0$ $R(V_{bias})$ is linear with respect to the applied voltage, the photocurrent expression in the OEM mode reduces to:

$$I_{photo}(t) = V_m\Delta_R P_{cw}sin(2\pi f_{ele}t+\phi)+\frac{V_m\Delta_R P_{mod}}{2}[cos(2\pi(f_{ele} - f_{opt})t + \phi) - cos(2\pi(f_{ele} + f_{opt})t + \phi)] \tag{4.8}$$

This requires a photodetector that presents a linear characteristics of the photocurrent versus the applied voltage. The advantage in having $V_{DC} = 0$ is that the first two terms in equation 4.7 are eliminated, which brings to lower electrical power consumption.
It has to be noticed that the parameters $R(\bar{V_{DC}})$ and Δ_R in equations 4.6,4.7 and 4.8 are dependent on f_{opt}. As already underlined, Δ_R is also dependent on f_{ele}. Depending on the application, an optoelectronic mixer has to operate a specific operation frequency. RADAR

and new communication systems like 5G technology can operate at some tens of GHz [50–54]. In these applications, the photodetector used as optoelectronic mixer must exhibit very large bandwidth.
Another important parameter is the optical operating wavelength of the optoelectronic mixer. The majority of applications require the typical telecommunication wavelength of 1.55 um. As silicon does not absorb 1.55 µm light, this is generally fulfilled using III-V compounds. State of the art optoelectronic mixers that operate at 1.55 μm wavelength are based on III-V semiconductors epitaxially grown on InP substrates. 60 GHz optoelectronic mixing has been demonstrated by using heterojunction phototransistors (HPT) based on InP/InGaAs, which exhibit high photoconductive gain [55]. InGaAsP-based travelling-wave uni-travelling carrier photodiodes have been employed in order to detect 0.1 THz signals, with a downconversion efficiency of -40 dB [56].
CMOS-compatible optoelectronic mixers have also been demonstrated: around 10 dB upconversion loss at 60 GHz has been measured by using avalanche photodiodes, at 850 nm optical wavelength[57].
The realization of high-speed optoelectronic mixers operating at telecom wavelength, which are compatible with the standard silicon technology, remains a challenge. The extraordinary electrical and optical properties of graphene could face this issue: graphene absorbs 1.55 μm light [17], so the photodetection inefficiency of silicon at the telecom wavelength is overcome. Moreover, the very high carrier mobility (up to 150000$cm^2V^{-1}s^{-1}$ at room temperature [58–61]) and short photocarrier lifetime [62] allow to reach very high frequency operations. Several CMOS-compatible graphene-based photodetectors have been already demonstrated [63–66].
For this reason, the possibility of using graphene as the active material for photodetection and optoelectronic mixing have been investigated in this Chapter.

4.1.1 Graphene-based photodetectors and optoelectronic mixers: State of the art

Different physical mechanisms at the basis of the photocurrent generation in graphene can be exploited in order to design a photodetector, as described in Chapter 1. In particular two competing mechanisms are present in biased graphene. These two mechanisms are very interesting for implementing OEM with graphene. In fact, the responsivity of photodetectors based on biased graphene is dependent on the electrical voltage that is applied between the two contacts of the graphene channel itself. Moreover, a zero bias corresponds to zero photocurrent generation(see 4.8.), which is a very convenient characteristics.
High-speed photodetectors based on graphene have been largely studied during the last years. One of the first works [65] demonstrated a 40 GHz bandwidth graphene-based photodetector, and predicted an intrinsic bandwidth that could exceed 500GHz. The graphene channel was

vertically illuminated, and the reported responsivity was about 0.5 mA/W. The actual state of the art performance in terms of bandwidth has been reached by Schall et al. [67] by using a graphene-based photodetector relying on the bolometric effect. The device consists in a graphene channel contacted by two electrodes and placed on top of a Si waveguide. The graphene layer absorbs light through the coupling with the evanescent field of the optical waveguide. A bandwidth of more than 128 GHz has been reported. This frequency limit has been mostly attributed to the used measurement equipment and not to the intrinsic device. The measured RF responsivity was about 0.18 mA/W. In terms of responsivity, A responsivity of 0.4 A/W (using photo-thermoelectric effect) without channel voltage bias and 1 A/W with channel voltage bias has been obtained by [68]. These results show that, in terms of bandwidth and responsivity, graphene has a high potential if used as active material for OEM.
The first experimental demonstration of optoelectronic mixing in graphene has been reported by Mao et al. [69]. In their work, the graphene channel was biased with a source-drain DC voltage and electrostatically doped by the gate voltage. They have demonstrated the mixing of a 2 MHz electrical signal with a 1 GHz intensity-modulated optical signal at 1.55 μm wavelength. The following part of this Chapter is dedicated to the study of high-frequency devices. First, a preliminary study is presented, in which 30 GHz OEM is demonstrated [70]. Starting from this result, a more complete study on the device performances is carried out by means of statistical analyses. In this last study, the analyzed frequency range has been extended up to 67 GHz.

4.2 Devices description

A schematic representation and an optical picture of the RF device used to demonstrate 30 GHz OEM are shown in the left part of figure 4.9. The device consists in a CPW that is interrupted in the central (signal) line by a graphene monolayer acting as the active part of the device.

The fabrication process, that is detailed in Chapter 2, includes the following steps: a CVD graphene monolayer was first transferred on a high-resistivity silicon substrate covered by a 2 μm thick thermal SiO_2 layer. Then, the graphene active zone was defined by optical lithography and reactive ion etching. A metallic multilayer (Ni-Ti-Au-Ti) was deposited by electron beam evaporation, and an optical lithography pattern allowed us to locally grow 2 μm thick pads by electrolytic process, which reduces RF losses. The metallic multilayer deposited on the graphene channel was removed by successive etching techniques (dry/wet) until the Ni base layer was removed by wet chemistry. Finally, a 30 nm thick Al_2O_3 layer was deposited by Atomic Layer Deposition (ALD) to passivate the graphene channel [71]. The comparison between the Raman spectra performed after graphene transfer (i.e, before the lithographic process) and after passivation, indicates that the structural properties of

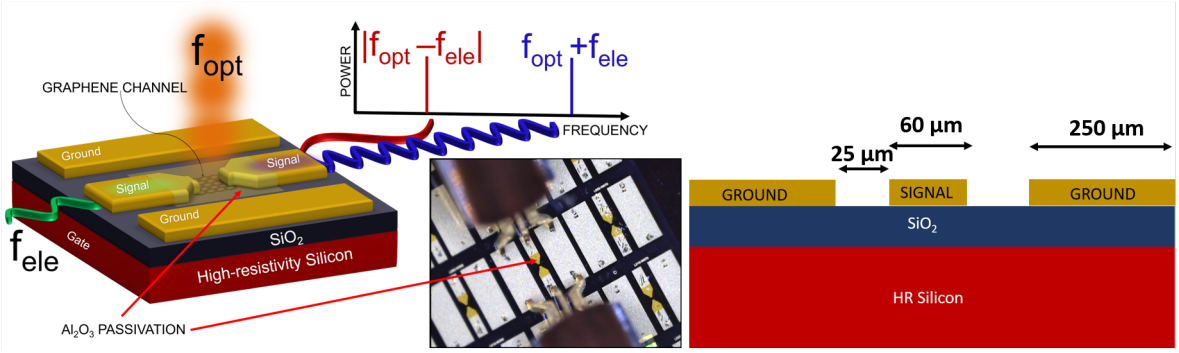

Fig. 4.9 Schematic of the graphene-based optoelectronic mixer. The simultaneous injection of an intensity-modulated laser beam at frequency f_{opt} and an electrical RF signal at frequency f_{ele} produces at the output two signals at the difference and sum of the input frequencies. *In the center*: Optical image of the gCPW, contacted by the RF probes. The graphene channel is passivated with an Al_2O_3 layer. To allow the RF probes to electrically contact the device, the insulating film has been removed on the metallic pads. On the right, the transversal view of the gCPW, and its dimensions.

graphene are not degraded by the fabrication process Appendic B.

As shown in figure 4.9, the ground-signal spacing is 25 μm, and the signal and ground width are, respectively 60 μm and 250 μm. These two dimensions have been chosen by considering the oxide thickness and dielectric constant in order to obtain a 50 Ohm match, necessary to minimize the electrical insertion losses when the device is coupled with the measurement system. The details are presented in Appendix A. The experimental setup designed to measure the devices is described in section 2.2.3.1. DC and RF characterizations have been performed on this device. In particular, we first measured the current flowing on the device by applying a voltage between the two sides of the CPW, and a voltage to the substrate acting as a gate. The RF measurements concerns the characterization of the devices as photodetectors and as optoelectronic mixers. A preliminary result on the first fabricated device is shown in Section 4.3. Then a complete characterization of several RF devices is presented in Section 4.4.

4.3 Photodetection and optoelectronic mixing demonstration up to 30 GHz

Our first result has been obtained on a device with a graphene channel length of L = 23 μm and width W = 20 μm, shown in figure 4.9. The solid blue line in figure 4.10a shows the DC current that flows in the graphene channel as a function of the voltage applied to the substrate (acting as a back-gate) for a DC channel bias $V_{DC} = V_{IN} - V_{OUT} = 4$ V. Thanks to the Al_2O_3 passivation layer, time-stable V-shaped curves are obtained [72]. The measurement

allowed us to determine the CNP voltage (V_{CNP}). Then, the biased channel was illuminated by a laser having a spot size of 20 μm, modulated in intensity at a frequency $f_{opt} = 5$ GHz. The modulated component of the optical power on the channel was $P_m = 22.5$ mW. In the same figure 4.10a the amplitude of the generated AC photocurrent ($I_{ph,m}$) is plotted as a function of the back-gate voltage (red dots). This AC photocurrent corresponds to the term $R(\bar{V_{DC}})P_{mod}$ in equation 4.7. From the graph, one can see that the photodetection has its maximal efficiency when the channel current is minimum. In this particular experiment, the applied gate voltage range didn't allow us to explore the high doping regime, in which the bolometric current regime dominates. For this reason, we studied the RF optoelectronic response of the device by setting the gate voltage to the charge neutrality point, where the photoconductive regime dominates, and a local maximum of the photoresponse is present.
We performed two types of experiments. First, we characterized the device by maintaining a DC channel bias voltage (*photodetection*). Then, the constant bias was switched off and an RF signal was injected (*optoelectronic mixing*).

4.3.1 Photodetection

For the same laser parameters of figure 4.10a, figure 4.10b shows the amplitude of $I_{ph,m}$ as a function of the channel bias. The dependence is linear for voltages up to 6 V. The $I_{ph,m}$ amplitude value obtained for $V_{DC} = 8$ V suggests that the photocurrent response starts to saturate for voltages above 6V. Such a behavior has already been observed [3].
Figure 4.10c shows that the amplitude of $I_{ph,m}$ varies linearly with P_m (P_m varies between 0 and 22.5 mW). The modulation frequency is still $f_{opt} = 5$ GHz and the channel bias was $V_{DC} = 6$V.
For the same channel bias, the frequency response of the device is presented in figure 4.10d. Here, the responsivity[2] (namely, the photocurrent amplitude $I_{ph,m}$ normalized over the modulated component of the optical power P_m) is plotted as a function of f_{opt} for frequencies up to 30 GHz.
Figure 4.10b and 4.10c demonstrate that the photocurrent is a linear function of both the channel bias and the optical power. This experimental evidence allows to write the equation of the generated photocurrent in biased graphene by using equation 4.2.

[2]In [70], all the plots in figure 4.10 are calculated by normalizing the obtained photocurrent to the instrumentation losses and also to the transmission losses of the device, in order to evaluate the intrinsic responsivity of an ideal device which doesn't present transmission losses. This is clearly specified in [70] and in the *Supporting information* accompanying the article. Here the plots are presented without the normalization over the device transmission losses, in order to be quantitatively consistent with the results presented in the rest of the Chapter, on which this correction has not been performed.

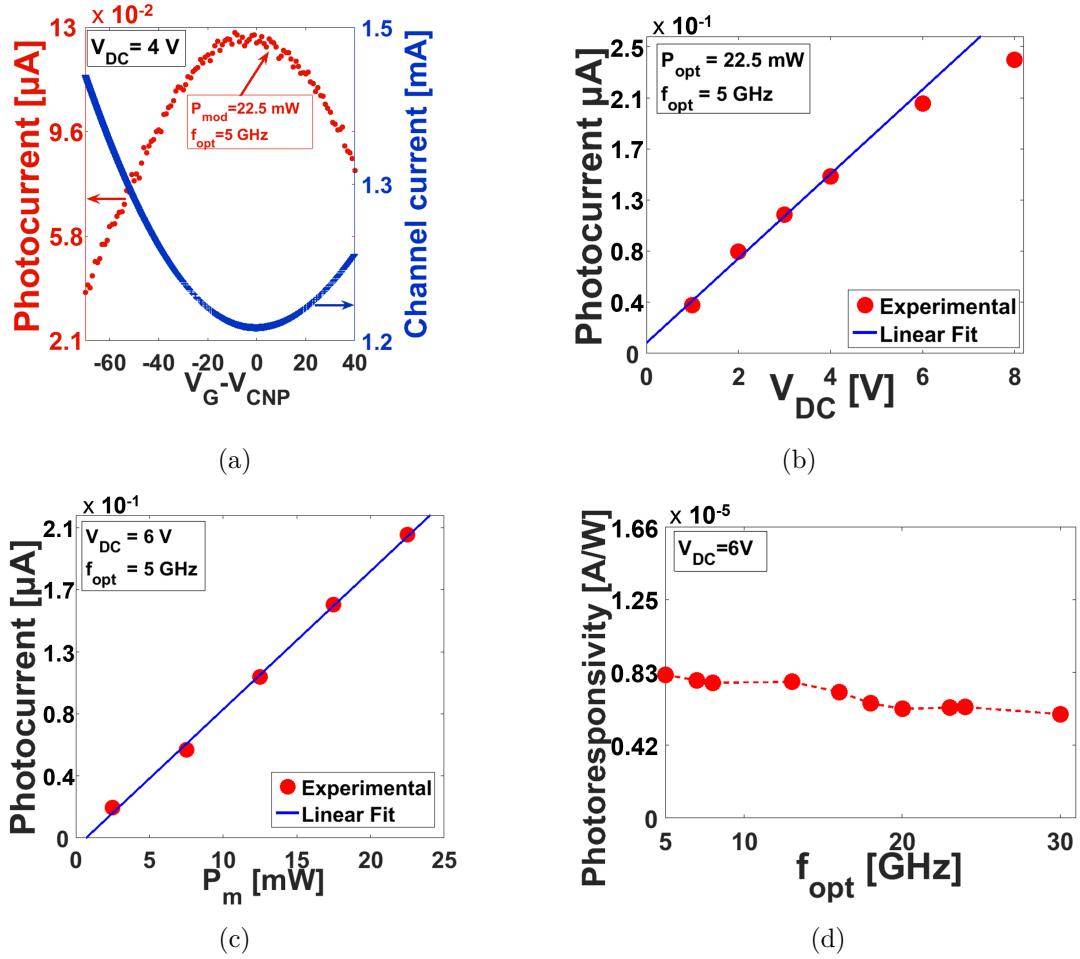

Fig. 4.10 a) *blue plot:* channel current as a function of $V_G - V_{CNP}$; *red plot*: photocurrent generated by a 5 GHz intensity-modulated laser beam. The modulated component of the laser beam is fixed at P_m= 22.5 mW. Both curves are measured under a channel bias voltage $V_{DC} = 4V$. b) Photocurrent as a function V_{DC} for $P_m = 22.5mW$ (f_{opt} =5 GHz); the small residual current at a polarization of 0 V predicted by the linear fit can be due to the non-perfect symmetry of the device [9]. c) Photocurrent as a function of P_m for f_{opt} =5 GHz and $V_{DC} = 6V$. d) Responsivity ($I_{ph,m}/P_m$) as a function of the optical modulation frequency f_{opt}.

4.3.2 Optoelectronic mixing

Equation 4.2 - 4.7 shows that a bias-dependent responsivity is essential in order to operate a photodetector as an optoelectronic mixer. Moreover, we just showed in figure 4.10b that around $V_{DC} = 0$ the responsivity $R(V_{bias})$ is linear with respect to the applied voltage. So, also equation 4.8 holds for our device. Following what has just been stated, for the optoelectronic mixing configuration, we switched off the constant voltage bias V_{DC} and injected an RF modulated signal in the gCPW, while maintaining the illumination of the graphene channel. The blue solid line in figure 4.11a shows the power measured on the spectrum analyzer. The injected electrical power was 14 dBm, at frequency $f_{ele} = 400$ KHz. P_m was set to 22.5 mW, and $f_{opt} = 5$ GHz. Two peaks appear at $f_{down} = |f_{opt} - f_{ele}| = 4.9996$ GHz and $f_{up} = f_{opt} + f_{ele} = 5.0004$ GHz, experimentally demonstrating the optoelectronic mixing. One can notice that no signal at f_{opt} is measured (no constant bias V_{DC} was applied). For a direct comparison with the photodetection mode, in the same figure (4.11a), the red dashed curve shows the power signal when the modulated component of the electrical signal was switched off, and a constant $V_{bias} = V_{DC} = 3$V was applied.
For the same optical signal ($f_{opt} = 5$ GHz) and the same electrical frequency (f_{ele}=400 KHz), we measured the downconverted power P_{IF} at intermediate frequency (IF=4.9996 GHz) as a function of the RF electrical input power (P_{IN}). Figure 4.11b shows that P_{IF} varies linearly with P_{IN}. As P_{IF} and P_{IN} are respectively proportional to I_{ph}^2 and V_{RF}^2, I_{ph} varies linearly with V_{RF}. This confirms that I_{ph} is proportional to the source-drain bias for either DC (figure 4.10b) or AC electrical signals (4.11b).

We then studied the optoelectronic mixing with high-frequency (close to 30 GHz) electrical and optical signal carriers. In particular, for $f_{opt} = 30$ GHz and $f_{ele} = 29.9$ GHz, a downconversion to $f_{down} = 100$ MHz is obtained (figure 4.11c).
Figure 4.11a shows the output power of the device, at a fixed optical input power, for the same electrical power absorbed in the graphene channel in both photodetection and OEM configuration. For photodetection, the absorbed electrical power is due to the DC bias, while in the OEM configuration it is due to the RF bias voltage. The output power is -94 dBm (photodetection) and -98 dBm (OEM). Since an optoelectronic mixes a photodetected signal with an electrical AC signal, one can conclude that the low output power is mainly due to the small photodetected signal and not to the mixing process itself.
The photodetection losses can be attributed to the low photoconductive gain and the weak absorption. The photoconductive gain[19] is defined as $G = \frac{\tau_r}{\tau_{trans}}$, where τ_r is the recombination time, while $\tau_{trans} = \frac{L^2}{\mu V_{bias}}$ is the the transit time of a carrier under an electric field generated in the channel. Time-resolved experiments show a first sub picosecond relaxation time due to interactions with optical phonons followed by a picosecond decay[73–78]. By considering a mobility of 2000 $\frac{cm^2}{Vs}$, that is a typical value obtained in our CVD graphene, and by using a value of $\tau_r = 1$ ps, we found for our device a photoconductive gain

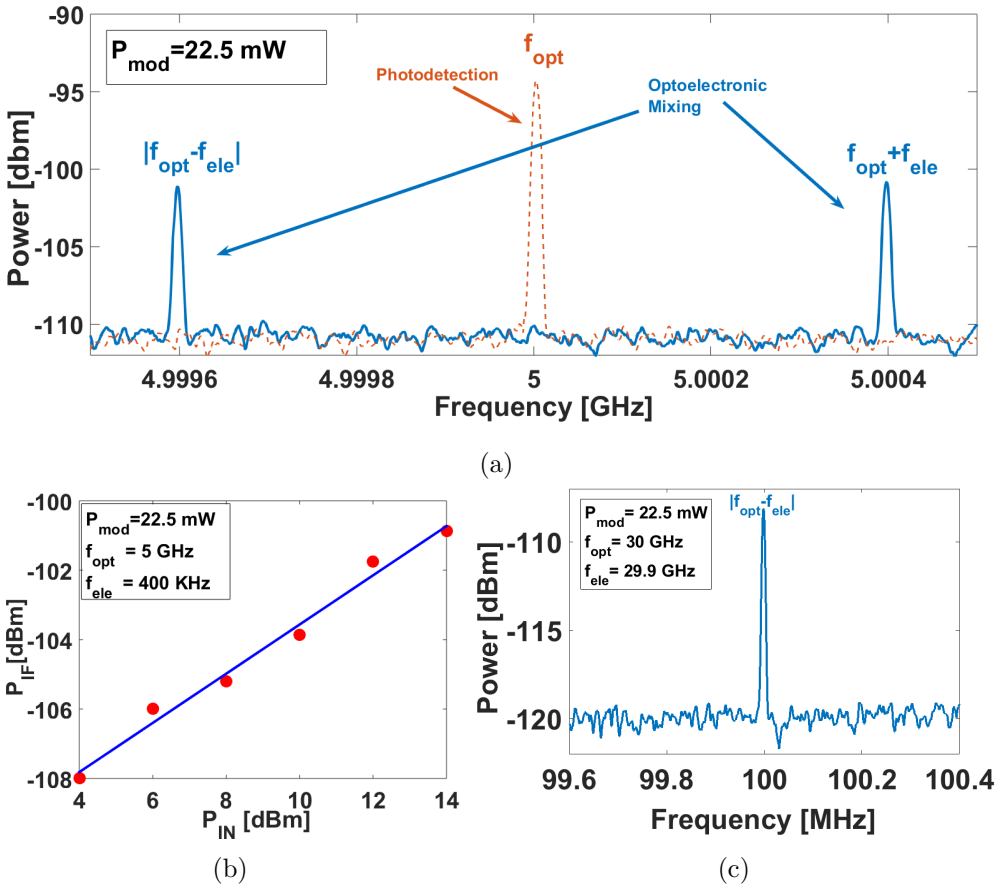

Fig. 4.11 a) *Solid blue curve*: optoelectronic mixing effect, obtained by injecting a 14 dBm electrical signal at frequency f_{ele}=400 KHz. The laser parameters are: P_m = 22.5 mW and f_{opt} = 5 GHz. *Red dashed curve (for comparison)*: photodetection of the modulated component of the laser beam at 5 GHz. In this case, $V_{bias} = V_{DC}$ = 3 V. b) Downconverted power (P_{IF}) at intermediate frequency (IF) as a function of the electrical RF input power (P_{IN}), for the same laser parameters and electrical frequency (400 KHz). c) Downconverted power to 100 MHz of a laser signal at f_{opt}=30 GHz (P_m=22.5 mW), mixed with a 10 dBm electrical signal at 29.9 GHz. The laser power is P_m=22.5 mW.

around 10^{-3}. This corresponds to a power loss, with respect to the case G = 1, around 60 dB.
Moreover, one has to consider the intrinsic limitation of graphene due to a small light absorption (which is however very impressive if we consider that we are dealing with a monoatomic material). The calculation described in Appendix A predicts a light absorption of about 1.8%. This corresponds to a power loss of 35 dB with respect to the ideal case of 100% absorption.
To improve the downconversion efficiency without decreasing the operating frequency, it is necessary to decrease the transit time τ_{trans} using shorter channels. The impact of this parameter is studied in Section 4.4.3.

4.4 Statistical study

4.4.1 Motivations

The first demonstration of high frequency OEM presented in 4.3 showed the potential of graphene as active material in optoelectronic mixers. The study has been limited in the region in which graphene has a photoconductive behavior, that is, around the Dirac point voltage (see Chapter 1). This preliminary study has been followed by a wider study over a considerable number of devices. These devices have been fabricated on the two inch wafer presented in Chapter 3. A statistical analysis is presented, thanks to the availability of 52 of devices. The study objective was the identification of the critical parameters that influence the performances of our devices. First, a contact resistance extraction technique for the RF devices based on a de-embedding method has been developed and analyzed. This allowed us to exclude the impact of the contact resistance on the photocurrent. We also conducted a study on the homogeneity of the photoresponse along the graphene channel, by scanning the laser spot over the active area. Moreover, the response was studied as a function of the geometrical parameters, that are the length (L) and the width (W). The frequency range of the measurements has been extended up to 67 GHz. Finally, we evaluate the performances of our graphene device as an optoelectronic mixer.

4.4.2 Circuital Model and contact resistance evaluation

In order to obtain the intrinsic performances of the tested RF devices and so to extract the relevant parameters, it was essential to evaluate the contact resistance of each gCPW. In Chapter 3 a statistical distribution of the contact resistance has been presented. This gives an idea of the mean contact resistance present also in the RF devices. However, the precise contact resistance cannot be determined on each tested gCPW with traditional DC methods, since just two contacts are present on the two sides of the graphene channel. Using the mean value obtained with four-probe devices to analyze the operation of one 2-contact RF device

would bring to erroneous results, because of the high dispersion of the contact resistance value distribution. Here we present a lumped electrical model of the gCPW in wich, instead of simply using a resistance to model the graphene-metal contact, a contact impedence is used. This contact impedence is extracted thanks to high-frequency measurements and a de-embedding technique [16]. This model has been proposed by [79] and tested on a very similar structure at frequencies up to 13.5 GHz. Here, the analysis is extended over a relevant statistical population, up to 67 GHz. This extraction method gives a statistical distribution of the contact resistance value that is in very good agreement with the one that has been obtained by means of the four-probe measurement in Chapter 3. Thanks to this result, we used this method in order to have a more precise value of the contact resistance for each device.

Figure 4.12 shows the lumped circuital scheme used to model the gCPW: a contact impedance

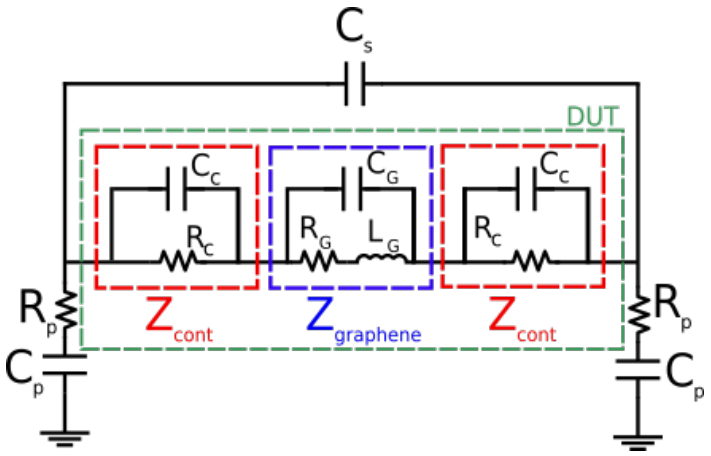

Fig. 4.12 Lumped circuit of the gCPW

.

Z_{cont} describes the metal-graphene contact. Also the graphene channel is modeled by using a generalized impedance $Z_{graphene}$ instead of a simple resistance. The two contact impedances in series with the graphene channel impedance $Z_{graphene}$ represent the device under test (DUT) embedded in the CPW structure. The CPW model includes a parallel capacitance C_s between the two signal sides of the gCPW and a series of a resistance R_p and a capacitance C_p modeling the coupling between the ground and signal lines. To extract the impedance values of the DUT, an open-short de-embedding method has been used. This procedure is largely described in literature, for example in [80, 81]. It consists in the S-parameters measurement of two different structures, shown in figures 4.13a and 4.13b:

- Open structure, is the same structure as the gCPW, but without the graphene channel.
- Short structure, in which the signal line is continuous, that is, metal is present instead of graphene. Moreover, the ground line is shorted with the signal line

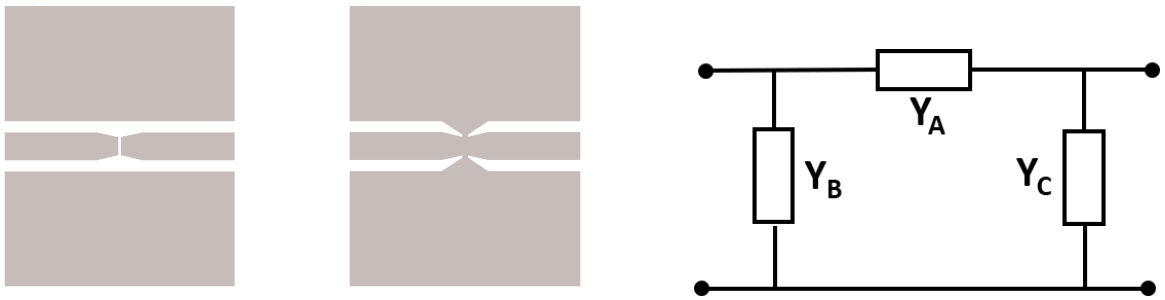

(a) (b) (c)

Fig. 4.13 Open (a) and short (b) structures used for de-embedding.(c): Pi-network used to model the gCPW

A measurement of the S parameters of the two structures and of the entire gCPW have been performed. Then, the S-matrix of each structure have been transformed in the corresponding admittance matrix Y, following the relation:

$$Y = \frac{1}{Z_0}(I + S^{-1})(I - S) \tag{4.9}$$

Where Z_0 is the transmission line connected to each port that has the value of 50 Ω.
By denoting with Y_{OPEN}, Y_{SHORT} and Y_{TOT}, respectively, the Y matrix of the open, short and entire device, one can find the inner (de-embedded) Y-matrix comprising the contribution of the contact and graphene impedance series as [81]:

$$Y_{DUT} = ((Y_{TOT} - Y_{OPEN})^{-1} - (Y_{SHORT} - Y_{OPEN})^{-1})^{-1} \tag{4.10}$$

This Y_{DUT} matrix can be conveniently written as:

$$\begin{pmatrix} Y_{11} & Y_{12} \\ Y_{21} & Y_{22} \end{pmatrix} = \begin{pmatrix} Y_A + Y_B & -Y_A \\ -Y_A & Y_A + Y_C \end{pmatrix} \tag{4.11}$$

The right part of the equation explicitly contains the values the Π-network through which a generic Y-matrix can be represented [30]. This lumped Π-network is represented in figure 4.13c. Y_A and Y_B represent the coupling between the graphene channel and the ground pads. In the model in figure 4.12 they are included in the series of R_p and C_p. $Y_A^{-1} = Z_A$ represents the DUT series impedance, that is, the series of the two contact impedances Z_{cont} with the graphene channel impedance $Z_{graphene}$.
In Reference [79], $Z_{graphene}$ and Z_{cont} are modeled as a capacitance and a resistance in paralell, and so has the following expression:

$$Z_A = \frac{2R_c}{1 + i2\pi f C_c R_c} + \frac{R_g}{1 + i2\pi f C_g R_g} \tag{4.12}$$

The terms R_c, C_c, and C_g have been sufficient to fit the measured Z_A up to 13,5 GHz. In order to fit our measurements up to 65 GHz, it was necessary to add an inductance in series with the resistances[3] in the graphene impedance. The complete model is shown in figure 4.12 and has the following expression:

$$Z_A = \frac{2(R_c + i\omega L_c)}{1 + i\omega C_c(R_c + i\omega L_c)} + \frac{R_g}{1 + i\omega C_g R_g} \tag{4.13}$$

with $\omega = 2\pi f$. The real and imaginary parts of Z_A have been fitted with the parameters R_c, C_c, L_c, C_g, while $R_g = R_{TOT} - 2R_c$, R_{TOT} being the total measured DC resistance, that corresponds to the extracted Z_A at low frequency.
A fitting example is shown in figure 4.14 for a gCPW with L=5 μm and W=5 μm, where the real and immaginary parts of the DUT impedance are plotted for high doping (a and b) and at the Dirac point voltage (c and d). Figure 4.15 shows the same curve, fitted by using the model proposed by [79]. As can be noticed, the model works for frequencies under 15 GHz, but starts to lack after this frequency values. For this device, the fitted values at high doping are: C_C=18 fF, C_G=1.7fF, R_c=4.8KΩ, L_G=1.9nH. At the Dirac point voltage, the fitting parameters are: C_C=17 fF, C_G=1fF, R_c=5.5KΩ, L_G=1.8nH.

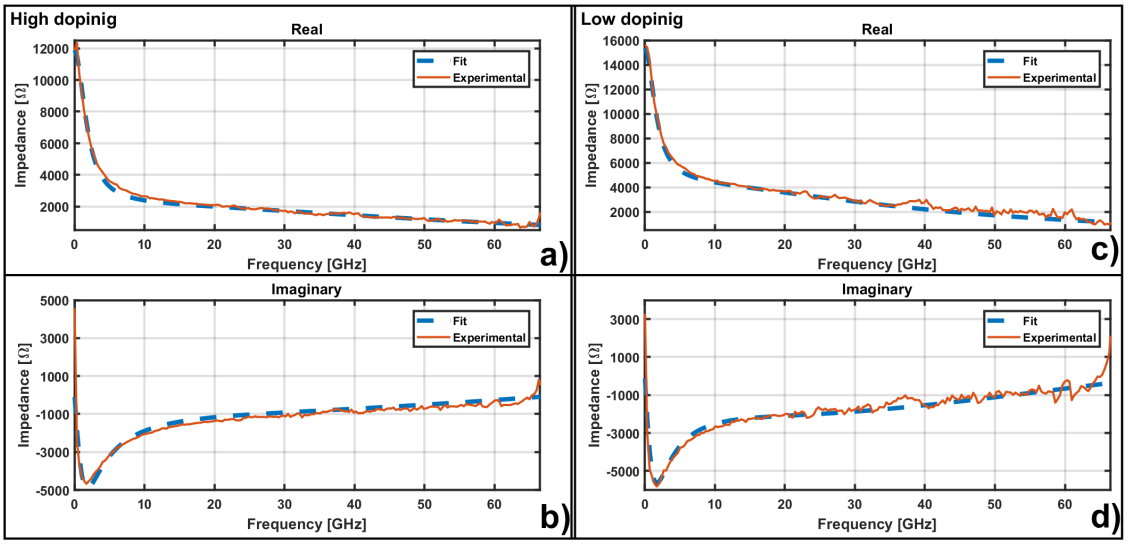

Fig. 4.14 Measured and fitted impedances at high doping and at the Dirac point voltage.

.

The fitting was conducted for 52 devices of square 9 and 20, and a statistics of the extracted contact resistance was extracted for high and low electrostatic doping. As done

[3]The origin of this series inductance at high frequencies cannot be associated to the kinetic inductance observed in high mobility samples [82, 83], but could be attributed to an equivalent residual parasitic parallel capacitance.

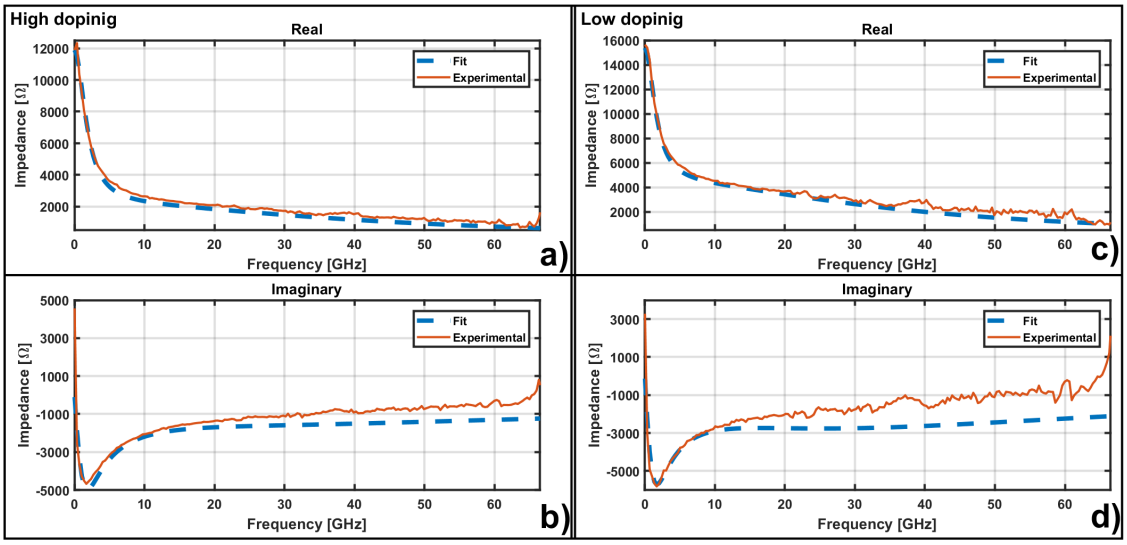

Fig. 4.15 Measured and fitted impedances at high doping and at the Dirac point voltage, without including inductive effects

.

with four-probe devices (see Chapter 3), the extracted contact resistance at high doping has been taken at 200 V from the charge neutrality point. The results are shown in figure 4.16a and 4.16b. As can be seen, they are in good agreement with the values determined from four-probe measurements (see figures 3.8a ans 3.8b). This method allowed us to determine the contact resistance value for each (2-contacts) RF device, instead of using a mean value extracted by means of the four-probe measurement presented in Chapter 3. The importance of knowing the contact resistance for each RF device will be highlighted in the following, where a statistical study on the photocurrent has been performed.

4.4.3 Photocurrent study

In the following Sections, a study on several devices with different channel lengths L and widths W is presented. The study consists in the measurements of the photocurrent generated in the devices by focusing a laser beam on the device channel. Contrary to the measurement performed in 4.3, the laser spot diameter has been reduced to 2.5 μm to measure a "local" photocurrent. Thanks to the use of two-stepper motors mounted to the collimator support (see 2.2.3.2), we where able to scan the laser spot over the channel with sub-μm precision and obtain a map of the photocurrent.
Figure 4.17 shows the optical image of one of the RF devices being tested. The point "A" is the initial position of the laser spot on the graphene channel, while point "B" indicates the laser spot final position. They define the rectangular region scanned with the laser spot, indicated with dashed lines. For each point, the generated photocurrent between 20 MHz

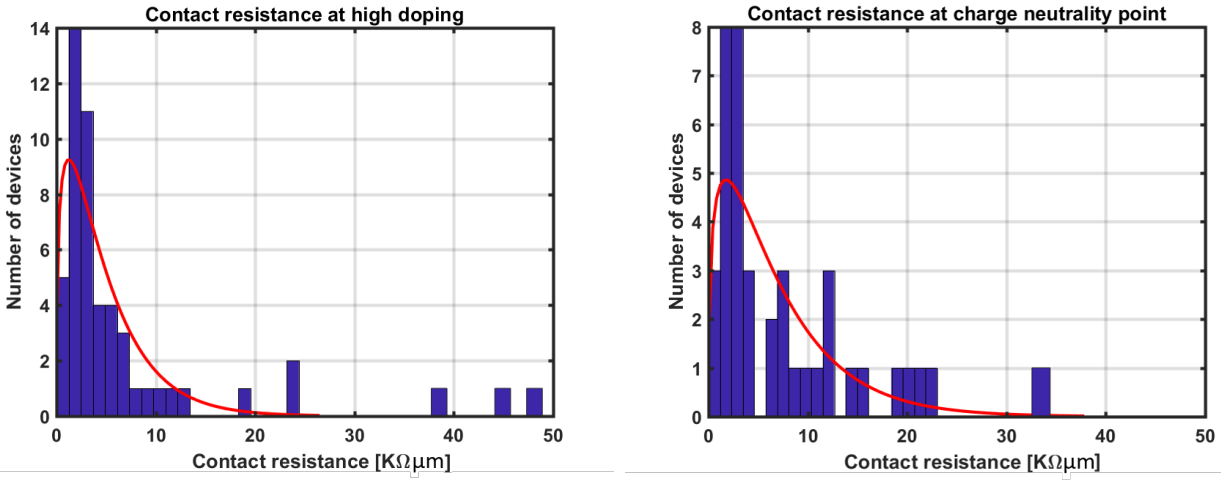

(a) (b)

Fig. 4.16 Extracted contact resistance using the de-embedding method though RF measurement at high doping (a) and at the charge neutrality point (b)

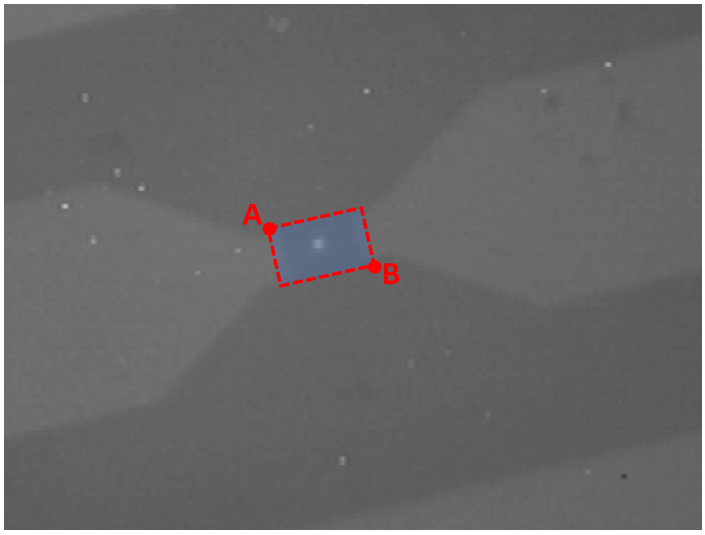

Fig. 4.17 Image of a gCPW with the laser spot focused in the center of the channel. The blue area confined in the red dashed line represents the scanned region. In the figure, the laser spot is positioned at the center of the channel

.

and 67 GHz was measured, as a function of the voltage V_{DC} applied along the graphene channel and of the voltage V_G applied to the substrate in order to change the Fermi level position. The measurement details are described in 2.2.3.

Figure 4.18 shows the measurement of one device, with L=10 μm and W=30 μm in which the laser spot was fixed on the central point of the graphene channel: the current at V_{DC} = 2V is plotted as a function of the gate voltage (figure 4.18a). The Dirac point voltage is around 70V. The blue curve in figure 4.18b shows the photocurrent as a function of the gate voltage, registered for a modulation frequency f_{opt} = 8GHz, and at an optical modulation power of 25 mW, while the red curve shows the phase of the photocurrent. A change in sign of the photocurrent takes place away from the Dirac point voltage, indicating a change from a photoconductive to a bolometric response. Around the Dirac point voltage (V_G = 70 V), the photocurrent has the same sign of DC current. This corresponds to the photoconductive regime. At high doping (e.g. V_G = -100 V or 200 V), the photocurrent exhibits an opposite phase. It thus corresponds to a bolometric current. The grey curve in figure 4.18b is the same DC current on the right, superposed for clarity.

We noticed a remarkable spatial dependence of the photoresponse along the channel. For

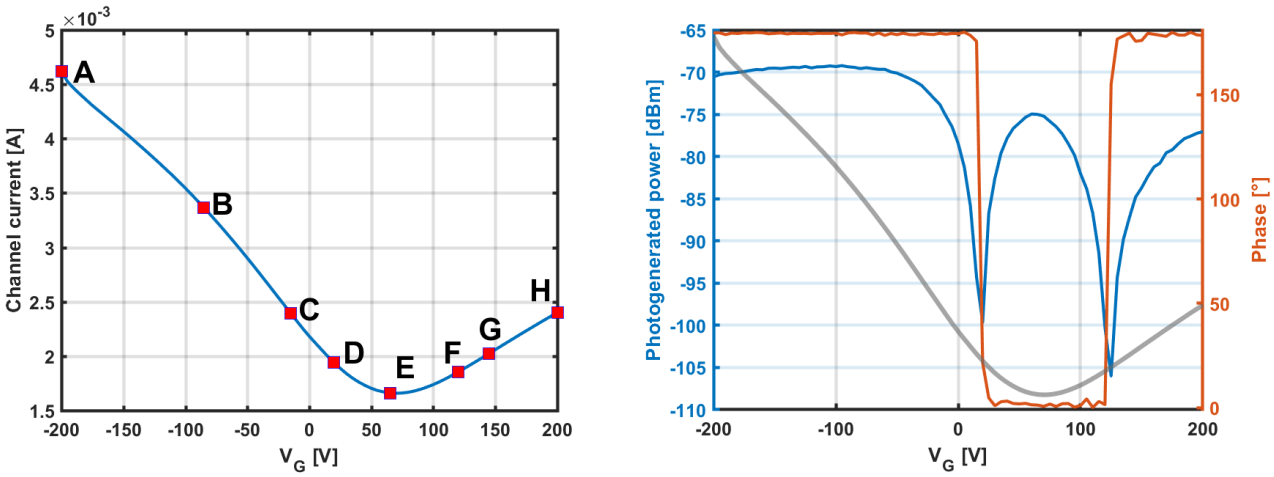

(a) (b)

Fig. 4.18 *a)* Current flowing along the graphene channel as a function of the applied gate voltage. The point A-H correspond to the gate biases at which the maps of the photocurrent over te channel are shown in figure 4.20. *b)* Photogenerated power as a function of the gate voltage (blue line) and photocurrent phase (red line).

this reason, we registered the photodetected power and phase along one straight line between source and drian. The results are presented in figure 4.19 and present the measurement on 4 different points along the straight line. The gate voltages at which the photoconductive regime is present are not the same along the channel, and the maximum of photoconductive current is not always centered around the Dirac point voltage (70 V), but instead varies from

0 to 100V. This variation corresponds to a variation in the carrier density of 10^{12} $cm^2V^{-1}s^{-1}$. We further investigated this experimental fact by scanning the laser spot along the whole the

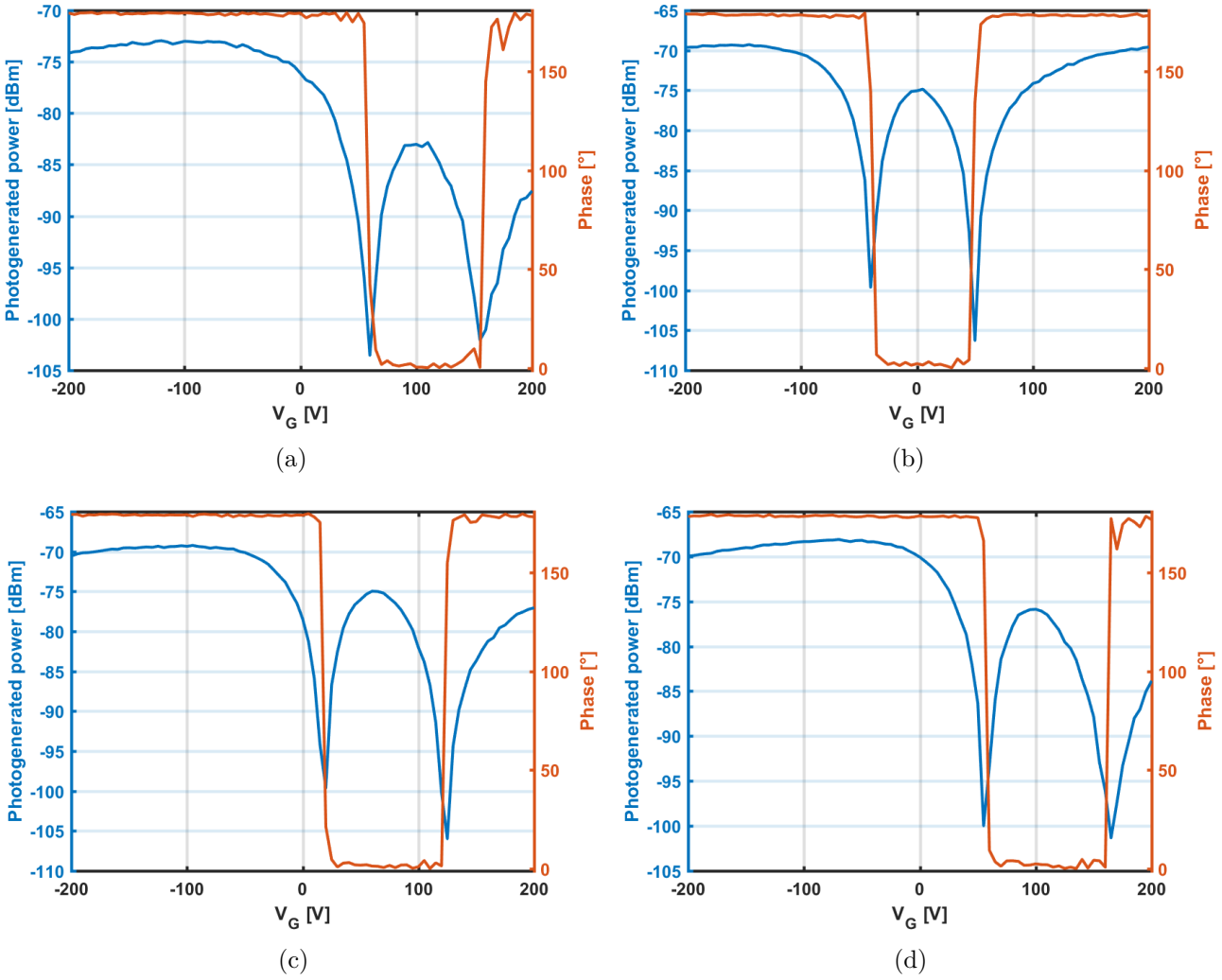

Fig. 4.19 Photogenerated power (blue curve) and photocurrent phase (red curve) versus the gate voltage at different positions of the graphene channel of a gCPW. The photoconductive maxima are measured at different gate voltages, depending on the laser spot position.

graphene channel for different gate voltages. Figure 4.20 shows the photocurrent map along the channel. Each plot shows the amplitude (left) and phase (right) of the photocurrent along the channel. The plots are tagged with a letter from A to H, and corresponds to different gate voltages. For each letter, the value of the gate voltage is shown on figure 4.18a. The maps reveal two behaviors:

1. When the channel is highly doped, the photocurrent phase (right part of plot A in figure 4.20) is homogeneous over the whole graphene channel, and is equal to 180°.

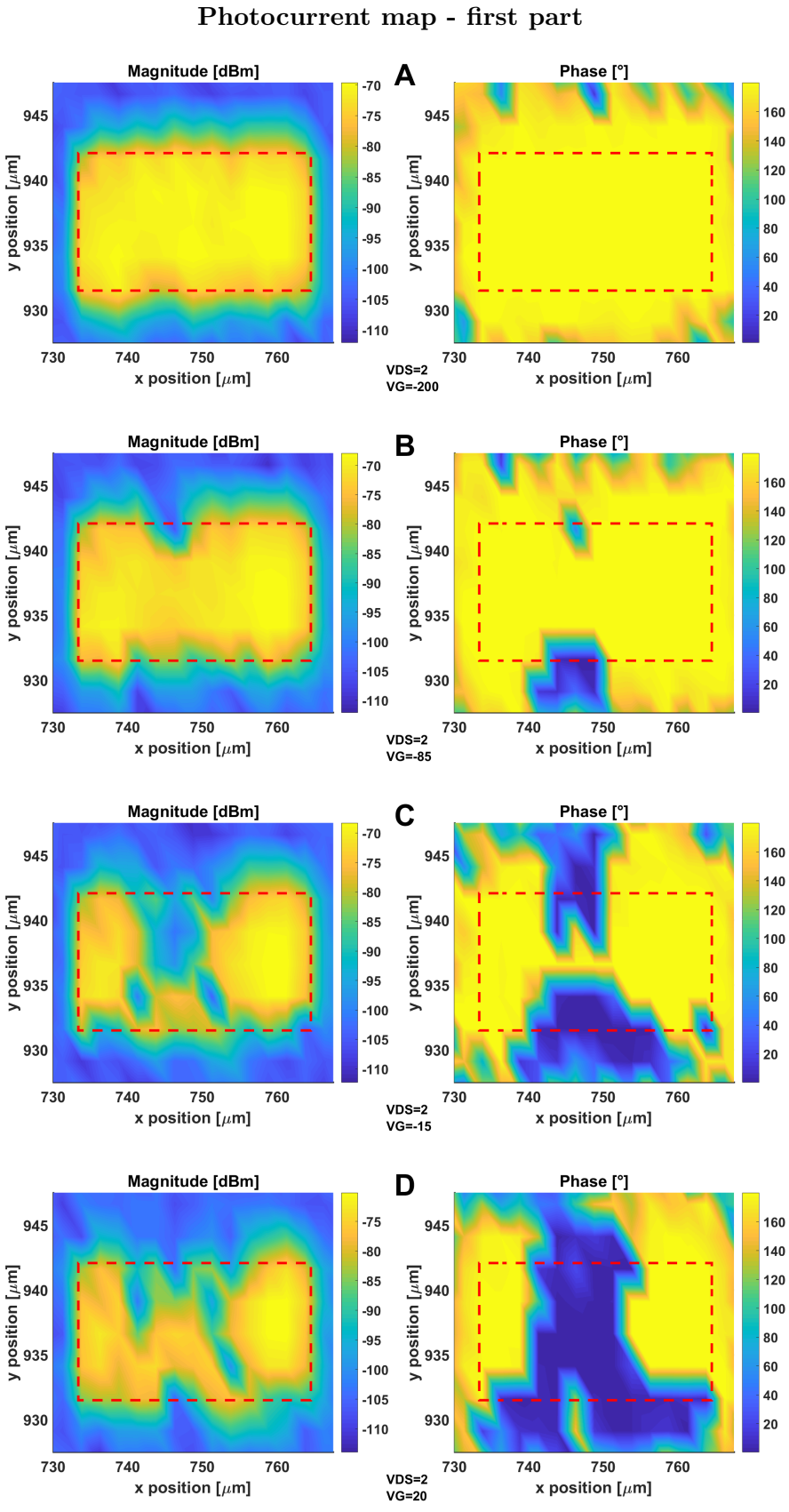

Fig. 4.20 Photocurrent map - first part

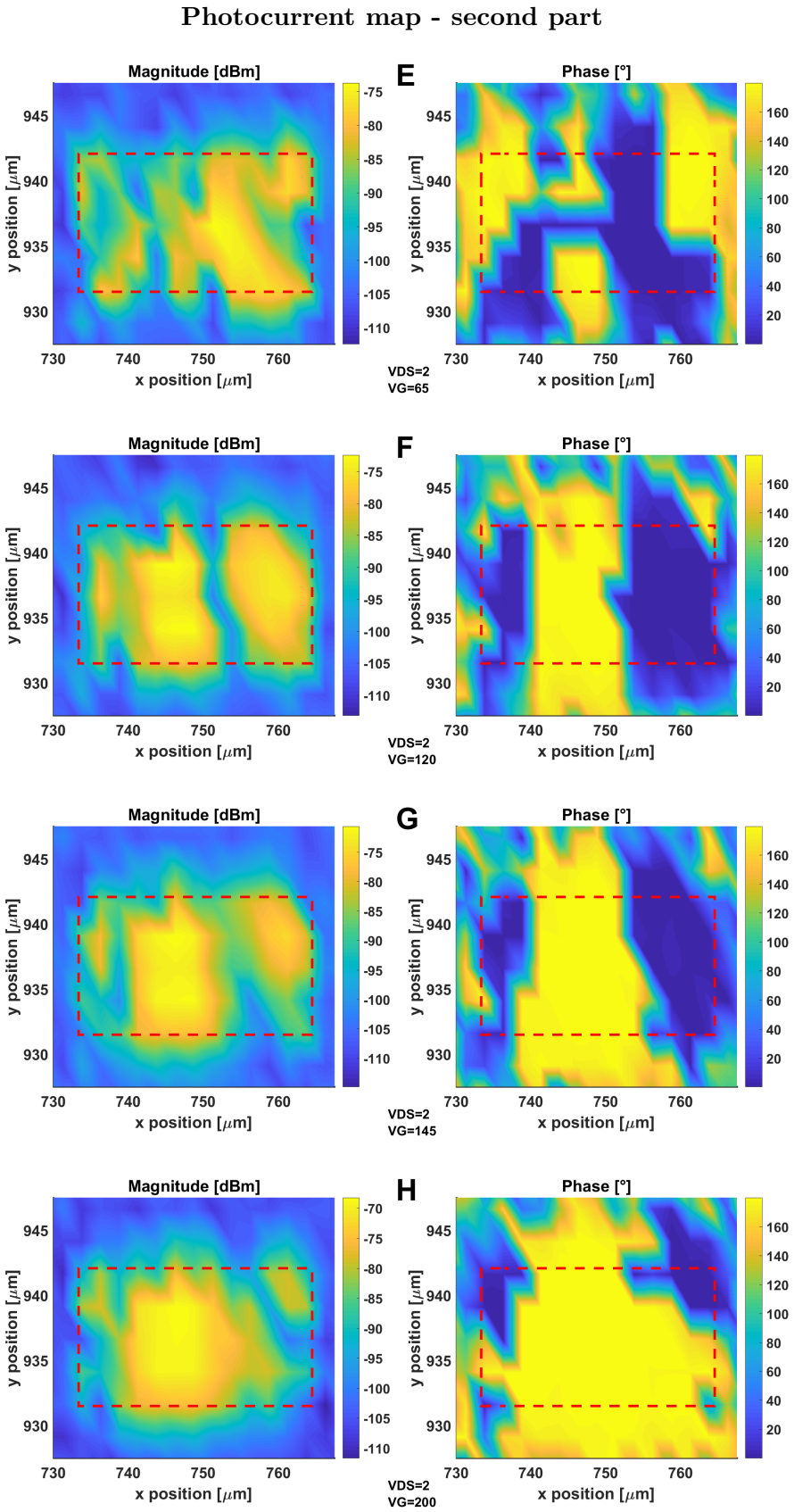

Fig. 4.20 Photocurrent map over the surface of a device with L = 10 μm W = 30 μm.The red dashed line confines the channel region. Each figure, named from A to H, is done at the gate voltage marked with the same letter in figure 4.18a. The applied voltage on the channel is V_{DC} = 2 V. The left part of each figure shows the power generated by the photocurrent on the 50 Ω of the VNA. The right part shows the phase of the photocurrent.

Thus, the graphene layer exhibits a bolometric response which is uniform along the channel.

2. When the gate voltage is set around the Dirac point voltage (plots D, E, F and G in figure 4.20), the response is not anymore homogeneous along the channel. Indeed, the phase of the photocurrent in this regime is 0° or 180°, depending on the laser spot position. In the regions exhibiting 0° photocurrent phase, the response is photoconductive, while in the other regions the response is bolometric. In this case, both photoconductive and bolometric currents coexist in the graphene channel.

Fig. 4.21 plots the mean photocurrent power value over the whole graphene channel as a function of the gate voltage. At V_G = -200 V, the mean power value (-75 dBm) is very close to the maximum power detected along the channel (-70 dBm) at the same gate voltage (see plot A in figure 4.20). On opposite, at V_G = 75 V, i.e. at a voltage close to the Dirac point voltage, the mean power value (-94 dBm) is much smaller than the maximum photodetected power along the channel at a similar gate voltage (see plot E in figure 4.20).
It is then interesting to re-analyze the photodetected power obtained with the first tested device (see Section 4.3). The measurements on this device were performed using a large laser spot diameter (20 μm) and for a gate voltage around to the Dirac point voltage. The measured photodetected power at the Dirac point voltage (see figure 4.11a) is equal to – 93 dBm, and is very close to the mean power calculated for the new device (see figure 4.21). So, the low response obtained on the gCPW in Section 4.3 has to be attributed to the inhomogeneity of the graphene channel response: a big spot focused over all the graphene channel generates local photocurrents that sum up. When the device gate voltage is set around the Dirac point voltage, this local currents can have different signs, giving as result low values of the overall photocurrent. This means that the photodetected power depends highly on the laser spot size and on its position.
As a conclusion the better photodetected power obtained with this new device with respect to the one presented in Section 4.3 is principally due to the use of a small diameter (2.5 μm instead of 20 μm) laser spot.
This behavior has been taken into account: in the following, we refer to the photoconductive current as the maximum photocurrent registered near the Dirac point voltage by scanning the laser spot along the channel.

In order to evaluate the performances of the RF devices as a function of the geometrical parameters of the channel (L and W), we tested the responsivity of 37 devices. For each device, we measured the photocurrent generated by an optical beam modulated at a frequency f_{opt} of 8 GHz, focused on the graphene channel. The optical power was 25 mW. The measured photocurrent has then been normalized to the voltage V_{DC} between the source and the drain, and is plotted against the channel L and width W at high doping in figure 4.22

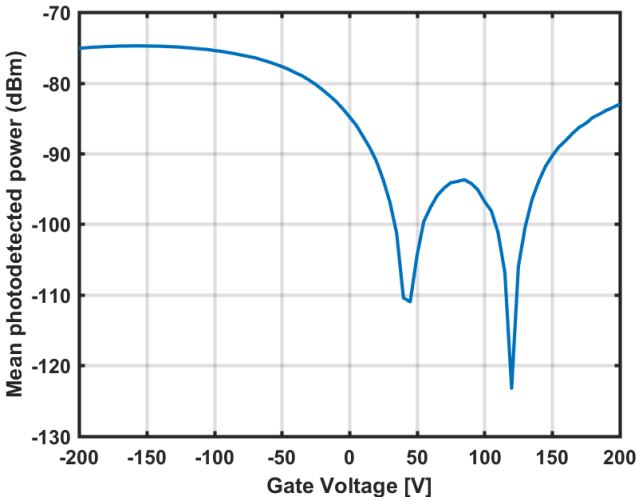

Fig. 4.21 Mean photocurrent power, calculated by integrating in space the maps obtained in figure 4.20 for each gate voltage

.

and at low doping in figure 4.23. No correlation is appreciable between the photocurrent and the geometrical parameters L and W. Actually, in order to properly analyze the dependence of the photocurrent from L and W, it is necessary to know the voltage drop along the channel, since the photocurrent is proportional to this quantity. In fact, the applied voltage V_{SD} corresponds to the voltage drop over the contact resistance plus the voltage drop along the graphene channel. As studied in Chapter 3, the value of the contact resistance is not negligible and exhibits a relatively high dispersion from one device to another. Thus, it is necessary to know the value of the contact resistance for each device in order to extract the voltage drop along the channel. This highlights the importance of the de-embedding technique described in the previous Section, thanks to which the contact resistance value of each RF device is extracted.

By taking into account the contact resistance, the voltage drop along the channel can be extracted. The photocurrent value in figures 4.24 and 4.25 can be normalized to this extracted voltage drop value. Figures 4.24a and 4.25a show the dependence of the normalized photocurrent with respect to the channel length L for different channel widths W for high and low doping respectively, while figures 4.24b and 4.25b show the normalized photocurrent with respect to the channel width W for different channel lengths L, for high and low doping respectively.

By eliminating the contribution of the contact resistance, a dependence of the photocurrent with respect to the channel length L comes out. In particular, the photoresponse decreases with L. Instead no appreciable dependence of the photocurrent with respect to W is present. The result can be explained by considering the expression of the photocurrent generated in a

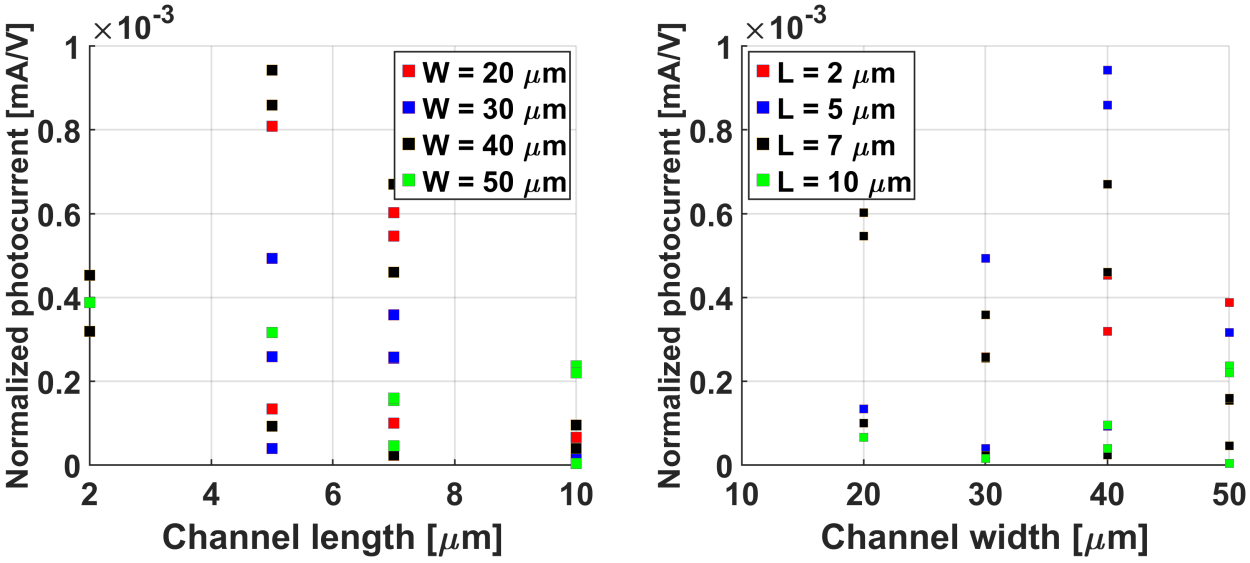

(a) (b)

Fig. 4.22 a) Normalized photocurrent as a function of the channel length L. b) Normalized photocurrent as a function of the channel width W. The measurement has been done at high doping. The normalization is performed with respect to the applied bias between the two sides of the gCPW.

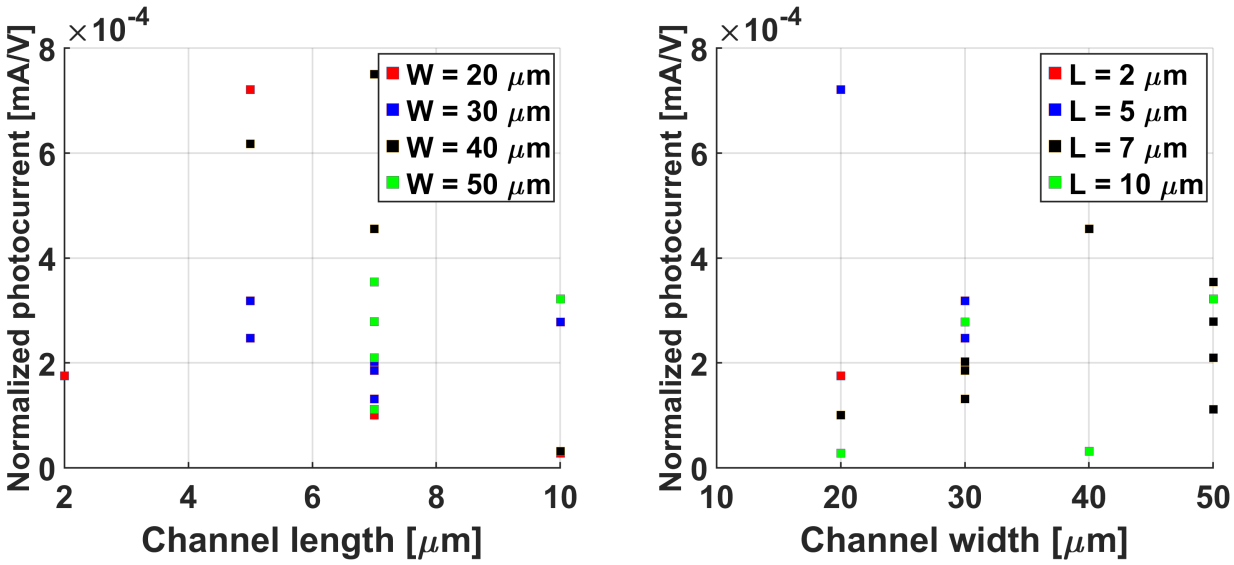

(a) (b)

Fig. 4.23 a) Normalized photocurrent as a function of the channel length L. b) Normalized photocurrent as a function of the channel width W. The measurement has been done around the Dirac point voltage. The normalization is performed with respect to the applied bias between the two sides of the gCPW.

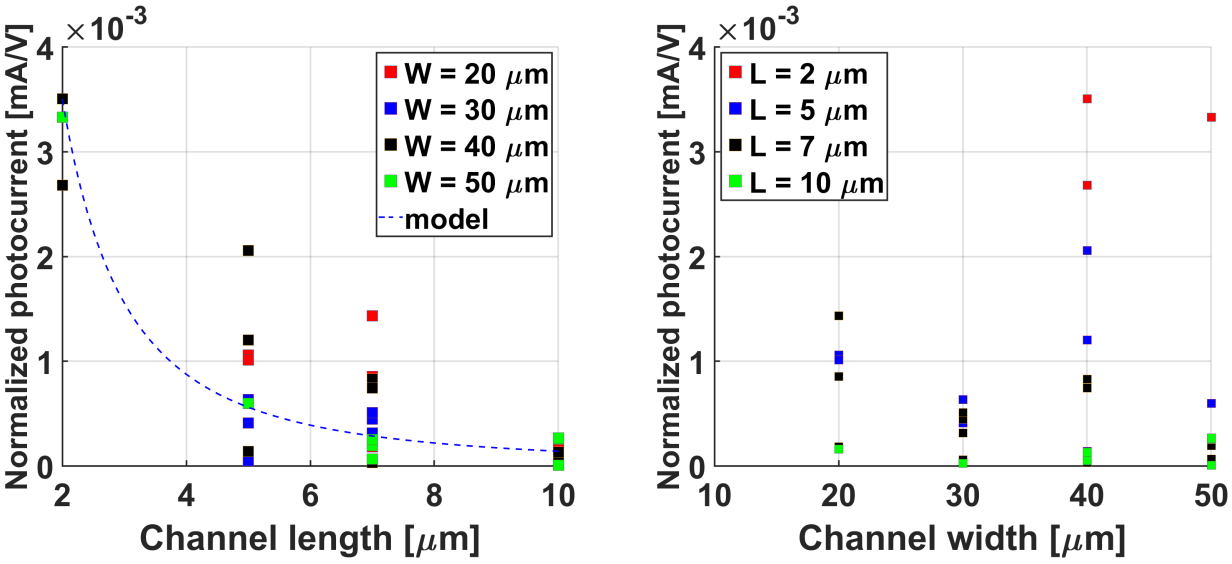

(a) (b)

Fig. 4.24 a) Normalized photocurrent as a function of the channel length L. b) Normalized photocurrent as a function of the channel width W. The measurement has been done at high doping, and the photocurrent value has been divided by the real voltage drop along the channel, without the contact resistance contribution.

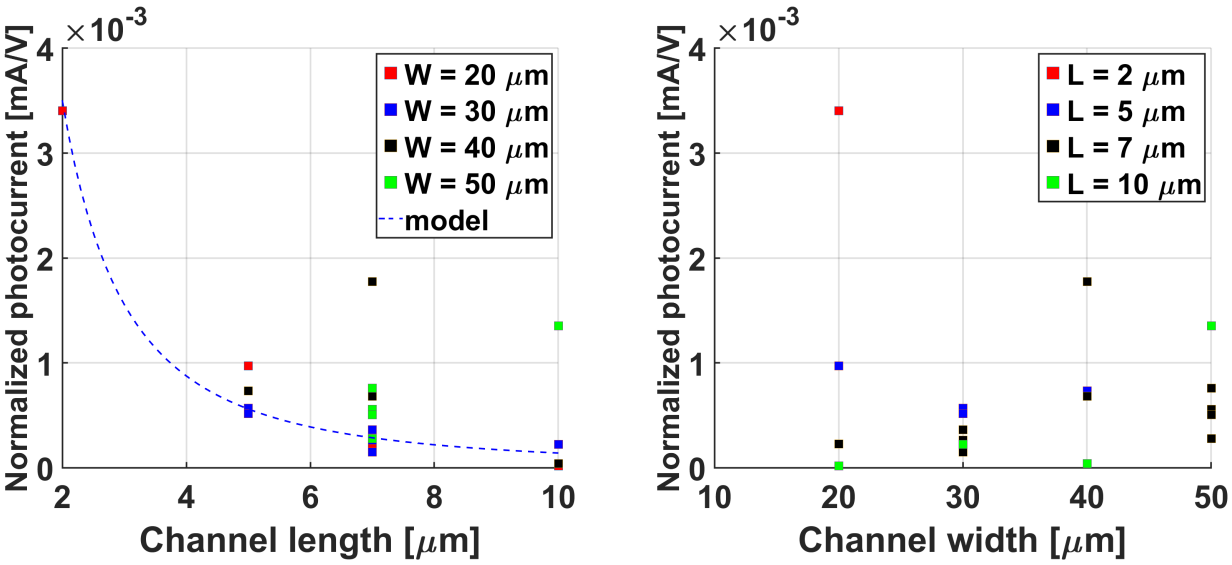

(a) (b)

Fig. 4.25 a)Photocurrent as a function of the channel length L. b) Photocurrent as a function of the channel width W. The measurement has been done around the Dirac point voltage, and the photocurrent value has been divided by the real voltage drop along the channel, without the contact resistance contribution.

photoconductor [84]:

$$I_{photo} = e\phi\eta G \tag{4.14}$$

where e is the electron charge, $\phi = \frac{P_{optical}}{h\nu}$ is the photon flux and η the quantum efficiency. G is the photoconductive gain, that is defined as:

$$G = \frac{\tau_{rec}}{\tau_{trans}} \tag{4.15}$$

Where τ_{rec} is the photogenerated carriers lifetime, and τ_{trans} their transit time which is:

$$\tau_{trans} = \frac{L}{V_{DC}}\frac{L}{\mu} \tag{4.16}$$

So that, the current can be written in this form:

$$I_{photo} = \frac{eP_{optical}}{h\nu}\eta\tau_{rec}\mu\frac{V_{DC}}{L^2} \tag{4.17}$$

While the dark current due to the application of a voltage bias V_{DC} is:

$$I_{dark} = ne\mu\frac{V_{DC}W}{L} \tag{4.18}$$

The photocurrent has a $\frac{1}{L^2}$ dependence, and is independent on W, as measurements confirm. On the other hand, the dark current has a $\frac{1}{L}$ dependence and a linear dependence in W. The blue dashed lines in figures 4.24a and 4.25a are plotted starting from the formula in equation 4.17, considering $\mu = 2000\frac{cm^2}{Vs}$, using $\eta\tau_{rec} = 0.12$ ps as fitting parameter. This value is similar to the one obtained by Freitag et al. [3][4].

So, by decreasing L, the ratio between the photocurrent and the dark current increases. On the contrary, in the limit in which the spot size is smaller than the channel width, decreasing W does not change the generated photocurrent, but the dark current can be reduced.

Another remarkable consideration rises comparing the plots in figures 4.22a and 4.23a (without any contact resistance correction) and the results in figures 4.24a and 4.25a: the performances of the devices with shorter channel are more affected by the presence of the contact resistance with respect to the devices with longer channel. Indeed, the performances of the devices with a channel length L = 10 μm do not change considerably after the elimination of the contact resistance effect, while the devices with a channel length L = 2 μm show a considerable normalized photocurrent increase. This because the contact resistance becomes comparable with the channel resistance while decreasing L.

Figure 4.26 shows the best result obtained in terms of photodetection on a device having L = 5 μm and W = 40 μm. The response of the device is almost flat up to 67 GHz, suggesting an operation frequency higher that this value, that is the limit of the measurement equipment.

[4] information contained in the supporting information of the article

The photodetected power attains -55 dBm. The optical power focused on the channel is 60 mW, and the DC bias V_{DC} = 3 V. The device exhibits a responsivity of 0.13 mA/W. The actual power coupled with the graphene channel has been calculated by considering the stack Air/Al_2O_3/Al_{Ox}/graphene/SiO_2/Si (see Chapter 2 for details on the technological process). By taking into account the refractive indexes of the different materials, we calculated that graphene absorbs 1.8% of the impinging light (see Appendix A for the calculations). By considering the amount of absorbed light, the photodeteted power value of -55 dBm is comparable with the values found in literature for CVD graphene [66, 67].

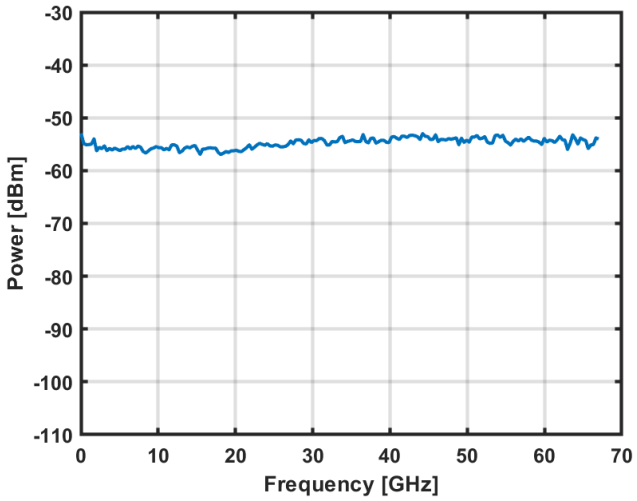

Fig. 4.26 Best photodetected power within the 37 tested devices, obtained for an optical power of 60 mW, at a V_{DC}=3V.

4.4.4 Optoelectronic mixing study

The 37 devices that have been characterized in Section 4.4.3 have then been tested as optoelectronic mixers, in order to evaluate their performances. First, we characterized the photocurrent flowing along the graphene channel as a function of the voltage bias between the two sides of the channel bias V_{DC}. Figure 4.27a shows the responsivity (that is, the photocurrent divided by the impinging optical power) obtained for a device with a channel length L = 2 μm and channel width W = 40 μm. The measured responsivity has been obtained at high doping (bolometric regime). The laser beam was modulated at a frequency f_{opt} = 8 GHz. It can be noticed that for this device the photocurrent is linear within a voltage range V_{DC} = [-1 V,1 V]. Outside this range, the responsivity starts to saturate.
We then added to the DC electrical bias an AC sinusoidal signal of 0 dBm at a frequency f_{ele} = 5 GHz. The blue line in figure 4.27b shows the downconverted photocurrent value at f_{IF} = 3 GHz as a function of the DC bias V_{DC}. It can be noticed that the maximum downconverted photocurrent is obtained for a DC bias V_{DC} = 0V. The red dashed curve in figure 4.27b has

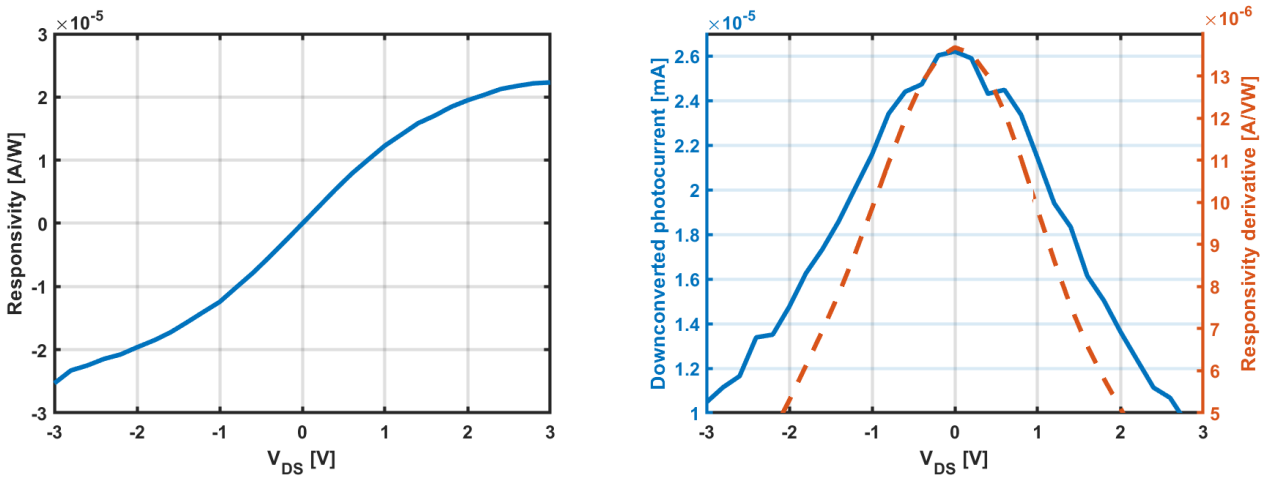

(a) (b)

Fig. 4.27 a)Responsivity of a gCPW versus the applied voltage V_{DC} between the two sides of the gCPW. b) Responsivity derivative with respect to V_{DC} (red dashed line) and downconverted photocurrent as a function of V_{DC} (blue line)

been obtained by computing the slope of the responsivity shown in figure 4.27a with respect to V_{DC}. The obtained similar shape of the two curves is easily explained by equation 4.8 which expresses the photocurrent at the intermediate frequency. The parameter Δ_R in the equation is the derivative of the responsivity as a function of V_{DC}, as defined in equation 5.3. If V_{DC} is further increased, the complete responsivity saturation can eventually be reached. This means that the responsivity starts to be independent on V_{DC} for high source-drain voltages. In this case no mixing effect is expected. One can conclude that the derivative of the photocurrent as a function of the graphene bias is a figure of merit for this kind of graphene optoelectronic mixers. In Section 4.1 we highlighted that a 0V bias is convenient since it brings to less power consumption. Figure 4.27 shows that this bias point is also convenient because the downconversion efficient is maximal.
For $V_{DC} = 0$V, We then measured the downconversion efficiency of all the devices studied in the previous Section in photodetection mode, by injecting an electrical signal in the gCPW. The best downconversion efficiency was obtained for a device with length L = 7 μm and W = 40μm. The result is presented in figure 4.28, and shows, to the best of our knowledge, the best performance of a graphene-based optoelectronic mixer in terms of bandwidth.

4.5 Graphene on Boron Nitride - first results

This Section is dedicated to the presentation of a preliminary study done in collaboration with the Laboratoire de Physique de l'Ecole Normale Supérieure (LPENS) of Paris. Compared

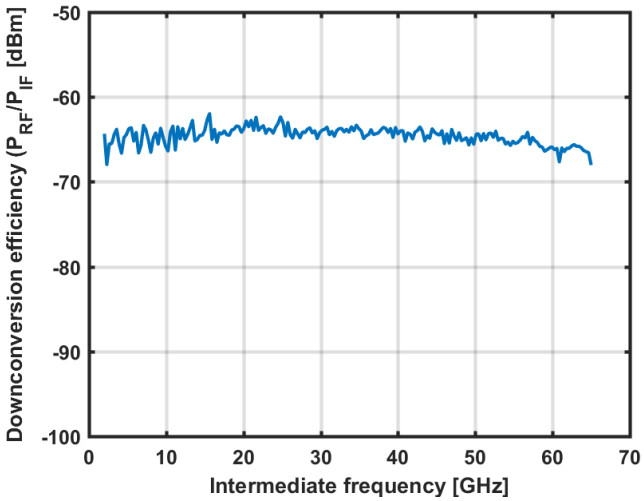

Fig. 4.28 Best downconversion efficiency within the 37 tested devices, obtained for an optical power of 60 mW, at a V_{DC}=0V.

to the gCPW just described, the geometrical design of these devices is unchanged but technological process (GoBN[5]) is different and has been developed at the LPENS [85]. Figure 4.29a shows a sketch of the stack used to fabricate the device: The substrate (High-resistivity Silicon + 2 μm SiO_2) is the same used for the gCPW presented in the previous Section. The graphene layer is encapsulated in exfoliated hexagonal boron nitride films (h-BN/graphene/h-BN), and then is protected by a layer of Al_2O_3 deposited by ALD. The metallic contacts are composed by a stack of 5 nm of chromium and 150 nm of gold. Figure 4.29b shows an optical picture of the fabricated device. The two sides of the CPW contacted the region where the BN has been exfoliated. The channel of the device is zoomed in the inset of figure 4.29b, which shows a SEM picture. The channel has a length of 3 μm and a width of 3 μm.

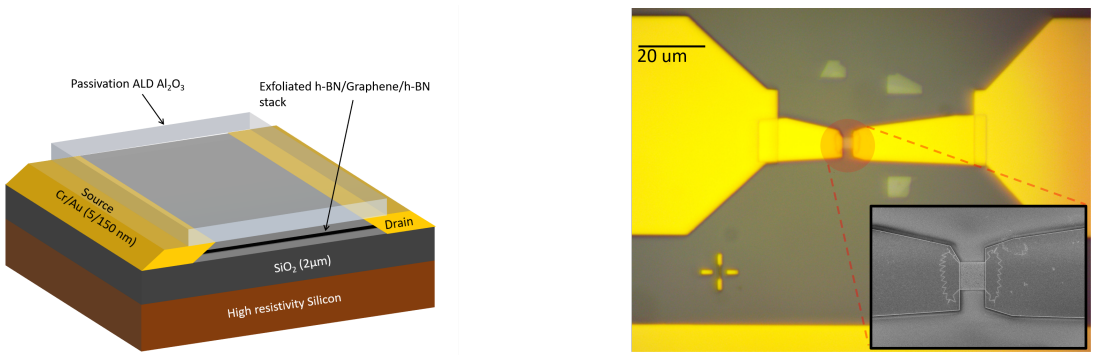

(a) (b)

Fig. 4.29 a)Sketch of the stack used to fabricate the gCPW using the GoBN technology. b) Optical image of the fabricated RF device. In the inset, an image of the graphene channel

[5]GoBN stands for Graphene on Boron Nitride

4.5.1 Experimental Results

Since no de-embedding test structures where fabricated in this sample, we were not able to extract the contact resistance value directly from the RF device. For this reason a four-probe device has been also realized on the sample. Figure 4.30a shows the extracted square resistance of the four-probe device, which channel is shown in figure 4.30b. The extracted contact resistance is about 1KΩ μm at high doping, and a carrier mobility is equal to 35500cm^{2}V^{-1}s^{-1}. The RF performances of the gCPW are shown in figure 4.31a. The

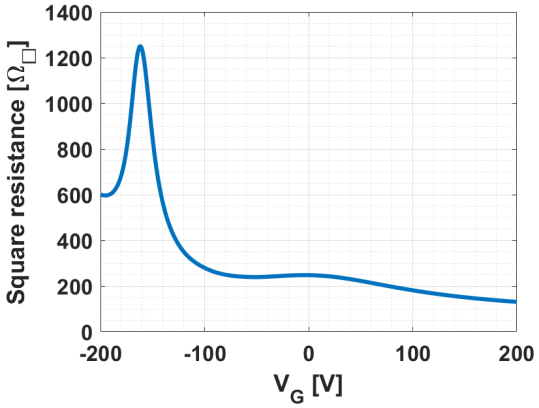

(a)

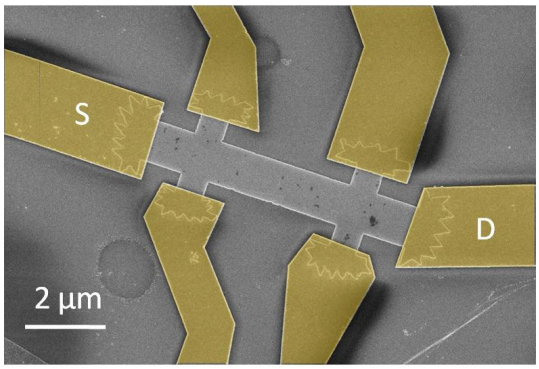

(b)

Fig. 4.30 a) Square resistance plot obtained from the four-probe measurement on the device shown in b).

voltage applied between the two sides of the gCPW was V_{DC}=0.4V, and the optical power was 50 mW. The back-gate bias V_G was set to 100V, which corresponds to an highly doped region. So, the registered photocurrent had a bolometric nature. As can be noticed in figure 4.31b, a high-pass behavior was measured, which has to be further investigated in the studies that will follow this preliminary measurement. The generated electrical power rising from the photodetection is higher than 40 dBm, and is 15 dB higher than the best result obtained for the gCPW measured in the previous Section. The corresponding responsivity is about 0.9 mA/W, which is 7 times higher than the best value obtained in the previous Section. The downconversion efficiency measurement is shown in figure 4.31b. Even in this case, the response is 15 dB higher with respect to the best value obtained in the previous Section. This measurement gives an experimental evidence of the benefits of having high carrier mobility in graphene as well as low contact resistance. The measured device has attained, to the best of our knowledge, the best performances in terms bandwidth and downconversion efficiency of a graphene-based optoelectronic mixer. Moreover, used as photodetector, the performances are comparable with those obtained with state-of-the art devices based on integrated optical waveguides coupled to the graphene channel.

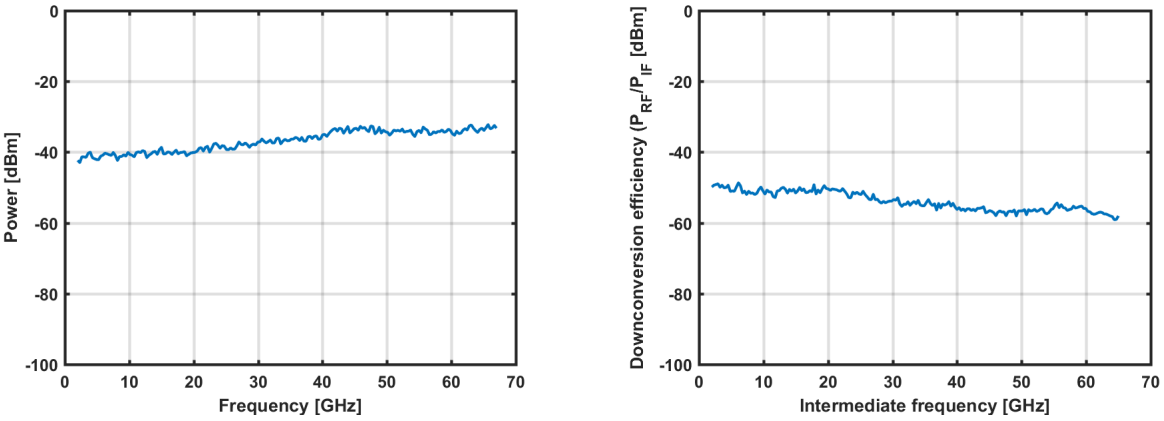

(a) (b)

Fig. 4.31 Frequency response of the gCPW based on GoBN technology. a) Shows the response of the device used as photodetector, while b) shows the downconversion efficiency.

4.6 Chapter conclusions

In this Chapter, the design and measurement of RF optoelectronic devices based on graphene has been presented. In particular, the devices have been tested as photodetectors and optoelectronic mixers. The use of a CPW embedding graphene allowed us to attain very high bandwidth operations up to the limit of the measurement equipment, i.e. 67 GHz.
A contact resistance extraction technique based on a de-embedding method has been developed. This method allowed us to determine the contact resistance for each RF device. As the average contact resistance of the RF devices was very close to the mean value determined with four-probe DC devices, this extraction method appeared reliable.
Thanks to this method, we were able to measure the normalized photocurrent (photocurrent divided by the voltage drop along the channel) for each RF device. The analysis shows a clear dependence of the photoresponse as a function of the channel length. The scan of the photocurrent value along the channel allowed us to show that, at low doping, a non-homogeneous response takes places while, at high doping, a uniform bolometric response is observed. Thus, the bolometric effect seems more suitable for the implementation of photodetectors and optoelectronic mixers.
Finally we studied gCPW fabricated with the GoBN technology. The associated high carrier mobility and low contact resistance allowed us to demonstrate the potential of graphene optoelectronic mixers.

Chapter 5

Optoelectronic mixing on graphene using high frequency transistors

5.1 Introduction

In Chapter 4 we presented the study of an optoelectronic mixer which relies on the modulation of the responsivity of a graphene photodetector with an electrical signal. This modulation is possible because a biased graphene channel produces a photocurrent which is directly proportional to the voltage applied to the channel itself. The change in time of this applied voltage produces the modulation of the detected photocurrent, an consequently the mixing. In this Chapter, we explore another approach to obtain optoelectronic mixing using a graphene-based transistor having a local RF back-gate.

Graphene high-frequency transistors (GFETs) for analog applications are very promising [86–88]. High speed operations with GFETs has been demonstrated in various works [89–92]. Here we explore the high frequency operation of GFET to obtain optoelectronic mixing. The graphene channel of the transistor is shined with a laser beam, as in the devices studied in Chapter 4, and a bias voltage is applied between the source and the drain. However, instead of modulating the voltage drop along the channel, we apply an AC signal to the back-gate of the transistor. This AC signal modulates the graphene channel doping and consequently the photocurrent magnitude and sign (see Chapter 1). In other words, this signal modulates the responsivity of the graphene channel. As a consequence, the AC signal applied on the gate is mixed with the AC photodetected signal. The mixing is then achieved since, as we have already seen, the photocurrent magnitude (and nature) depends on the graphene channel doping. We will start by the presentation of the fabrication of the device, which has been performed by the *Institut d'électronique de microélectronique et de nanotechnologie* (IEMN) in Lille. Then, the experimental characterization and performances analysis is presented.

5.2 Fabrication

Figure 5.1(a) shows a sketch of the graphene-based GFET and illustrates its operational principle as optoelectronic mixer. The device has a double-bottom gate structure. A laser beam is modulated at a frequency f_{opt} and focused on the GFET. As a result of the optical illumination, a photocurrent that contains an AC component at the frequency f_{opt} flows through the graphene channel. Similarly, if a radio frequency signal at a frequency f_{RF} is added to the gate of the transistor, the output current presents a term at the frequency f_{RF}. When both signals (optical and electric) are applied, the device acts as an optoelectronic mixer: the output contains the product of the two signals, and two AC components, $f_{opt} + f_{RF}$ and $f_{opt} - f_{RF}$ appear. The bottom gate transistor design is particularly suitable for optoelectronic mixing since (*i*) the graphene channel is laying on top of the gate and can thus be directly illuminated (*ii*) the use of a thin (4nm) Al_2O_3 dielectric and short gate length (0.4 μm or less) ensure high frequency operation [30, 87, 90]. To prevent ohmic losses at microwave frequencies, a high resistivity silicon wafer (resistivity larger than 8000 Ωcm) covered with 300 nm thick silicon dioxide was employed as a substrate. A schematic cross section of the bottom gate structure is presented in figure 5.1(b). The device fabrication started with the patterning of the double bottom-gates by electron beam lithography. Then, a 40 nm-thick layer of aluminum was deposited. An Al_2O_3 layer of around 4 nm thick is formed on top of the gates by exposing the substrate to pure oxygen for 30 min at room temperature [93]. This thin oxide acts as a gate dielectric. A single layer graphene was grown via CVD on 35nm-thick Cu, following the recipe in Ref. [23]. Afterwards, the graphene was etched by oxygen reactive ion etching to define the channel. The source and drain contacts were realized in a two-steps process. First, Cr/Au (5/50 nm) precontacts were deposited on top of graphene. Then, ohmic contacts were obtained by overlapping 30 nm of pure gold on top of the Cr/Au and the graphene, near the gate region. Finally, we realized the coplanar waveguide structure with a Ni/Au film (50/300nm). Figure 5.1(c) shows the scanning electron microscopy image of the bottom gates covered by graphene. The inset optical image shows a completed GFET integrated in the coplanar waveguide. The red square indicates the area occupied by the transistor. The quality of graphene after transfer process was verified by Raman characterization. Figure 5.1(d) shows Raman spectra obtained from three different areas of the substrate (SiO_2/Si) after the device fabrication process. The ratio of the 2D and G peak integrated intensities stands around 2.5, which indicates single layer graphene. The intensity ratio of the D and G peaks is very low, indicating the high quality of the graphene film after the devices fabrication process.

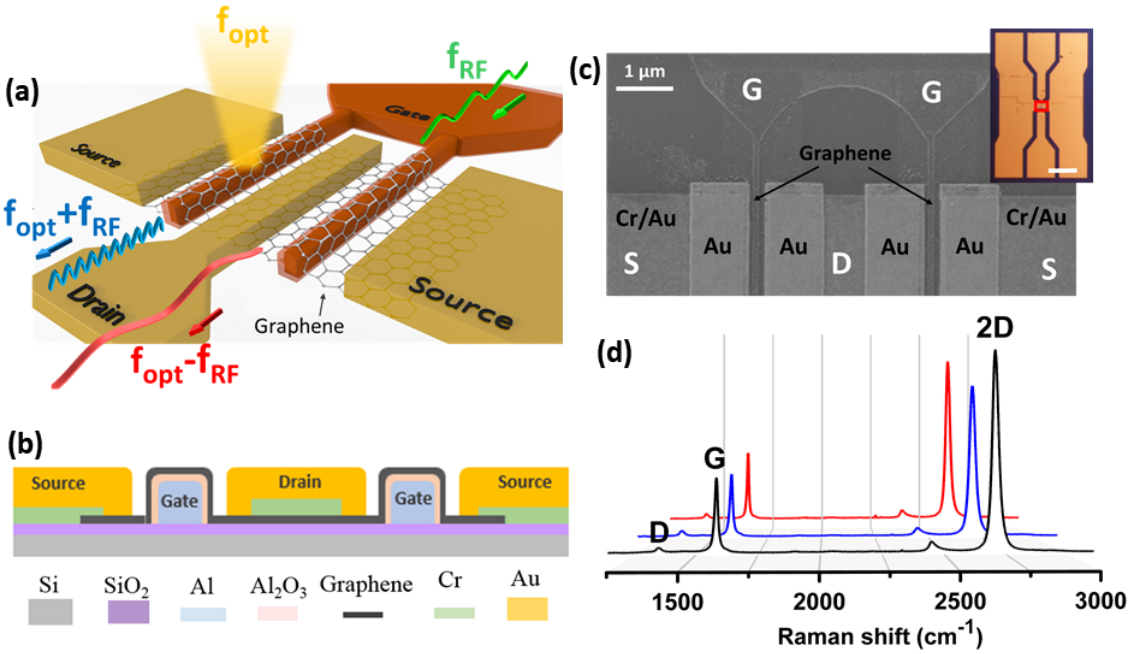

Fig. 5.1 a), GFET 3-D illustration. The sketch shows the principle of operation of our opto-electronic mixer.The mixing of the electrical signal at frequency f_{RF} with the photodetected signal at frequency f_{opt} generates two signals at the output with different frequency: f_{opt}+f_{RF} and f_{opt}-f_{RF}. b). Schematic of the cross section of our transistor, which corresponds to c) SEM image of the transistor with double gate covered by graphene. The metal in contact with graphene is pure gold. The inset optical image shows the transistor (marked by red rectangle) integrated with coplanar waveguide transmission line access. The scale bar is 100 μm. d) Two typical Raman spectra of our graphene recorded after device fabrication, showing high I_{2D}/I_G ratio and low I_D peak.

5.3 Experimental setup

The set-up scheme is very similar to the one already presented in Chapter 2 and is shown in figure 5.2a. The output of a 1.55 μm distributed feedback (DFB) laser was modulated by a Mach Zehnder modulator (MZM) used in the double sideband suppression carrier (DSB-SC) mode [31], to obtain a modulated beam at a frequency f_{opt}. The beam was then amplified with an Erbium-doped fiber amplifier (EDFA). The inset of figure 5.2a shows the laser beam focused on the transistor channel. The maximum laser power impinging on the sample was 60 mW. The gate and drain of the devices were connected to a vector network analyzer (VNA) with two high-frequency ACP probes from Cascade. The use of bias tees allowed us to DC bias the channel and the gate electrode.

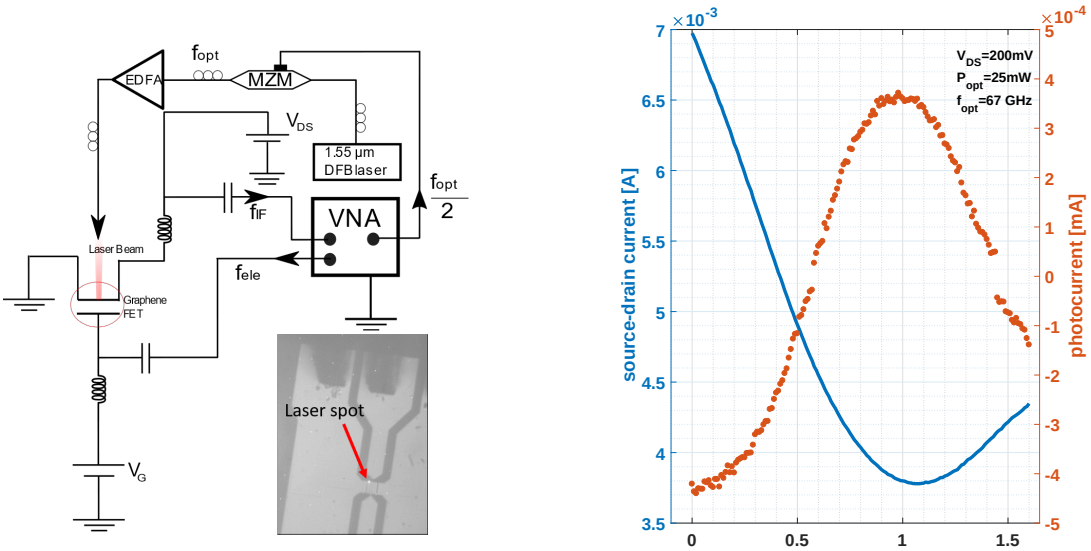

Fig. 5.2 a) Measurement setup. A cw laser is modulated by means of a Mach-Zehnder modulator (MZM). It is then amplified with an Erbium-doped fiber amplifier (EDFA) and focused on the graphene-based FET. An AC signal is applied to the gate of the transistor, and the resulting output (IF) is measured on a vector signal analyzer (VNA). Inset on the bottom-right corner: an optical image of the device with the laser focused on the channel. b) Blue line: Source drain current under an applied voltage V_{DS}=200 mV. Red line: photocurrent generated by a 25 mW laser beam focused on the graphene channel.

5.4 Experimental results

In the following, the complete characterization of a representative device is presented. The graphene channel width and length are respectively W=24 μm, L=400 nm. The gate length

is L_G = 200 nm. The field effect mobility is μ_{fe} =3800 cm^2/Vs. This value was deduced from the transfer characteristic $I_{DS}(V_{GS})$ recorded at a low bias voltage V_{DS}=10 mV, the gate capacitance was extracted from S-parameters.
The blue curve in figure 5.2b shows the source-drain current as a function of the gate voltage, at a source-drain bias V_{DS}=200 mV. The minimum of conductance is reached at gate-source bias V_{GS}=1.1V, which corresponds to the charge neutrality point voltage (V_{CNP}). First, the photoresponse of the transistor was characterized. The device was biased at V_{DS}=200 mV and illuminated with the laser beam modulated at an optical frequency f_{opt} = 67 GHz.
The photocurrent as a function of gate voltage is shown in the red curve of figure 5.2b, the optical power was 25mW. A change in the sign of the photodetected signal is present. I_{ph} is positive and has a local maximum close to the Dirac point voltage. At high doping (carrier concentration $n > 3.5 \cdot 10^{12} cm^{-2}$, or $V_{GS} - V_{CNP} > 0.5V$), I_{ph} becomes negative. This behavior, already reported in [3], is typical of biased graphene photodetectors. At low doping ($n < 3.5 \cdot 10^{12} cm^{-2}$), the laser power increases the carrier density in the channel (photoconductive regime) and the channel resistance decreases. Therefore, the photocurrent has the same sign as the DC current flowing in the channel due to the DC bias. At high doping ($n > 3.5 \cdot 10^{12} cm^{-2}$) the sign of the photocurrent is opposite to the DC current: this has been attributed to a decrease of the carriers mobility due to an increase of the carrier temperature caused by the laser power (bolometric regime) [3, 19].
In this experiment, only a fraction (31%) of the optical power of the 2 μm spot diameter laser power is actually coupled on the active area (W=24 μm and L=400 nm). Considering this, we measured a responsivity of 0.22 mA/W. A value of 0.4 mA/W was recently reached on graphene photodetectors coupled with an optical waveguide [66]. This higher value is justified because coupling with an optical waveguide gives a higher light absorption in the graphene channel [66].
For V_{GS}=0, the device reaches its maximum photodetection efficiency (photocurrent of -4.2 10^{-4} mA). For this gate voltage, the 67 GHz photocurrent was measured as a function of the DC bias and the optical power. Figures 5.3a and 5.3b plot the photocurrent as a function of the DC bias (optical power fixed at 40 mW) and of the optical power (fixed bias V_DS=330mV), respectively. It can be noticed that the response is linear in both cases, as expected for a photoconductor, and already reported in [3]. The frequency response of the photodetected power has also been measured as a function of the optical frequency f_{opt} (figure 5.4a). We found a flat response over the whole band that can be investigated by our VNA, showing that the intrinsic graphene photodetection bandwidth is larger than 67 GHz. In order to operate the device as an optoelectronic mixer (instead of a photodetector), an RF electrical signal f_{RF} was added to the DC gate bias of the transistor (figure 2.13a). The frequency f_{opt} was maintained at 67 GHz, while the frequency of the electrical signal applied to the gate was swept from 2 to 65 GHz. The VNA was used to record P_{IF}, the transistor power at the intermediate frequency $f_{IF} = f_{opt} - f_{RF}$. For this device, a maximum

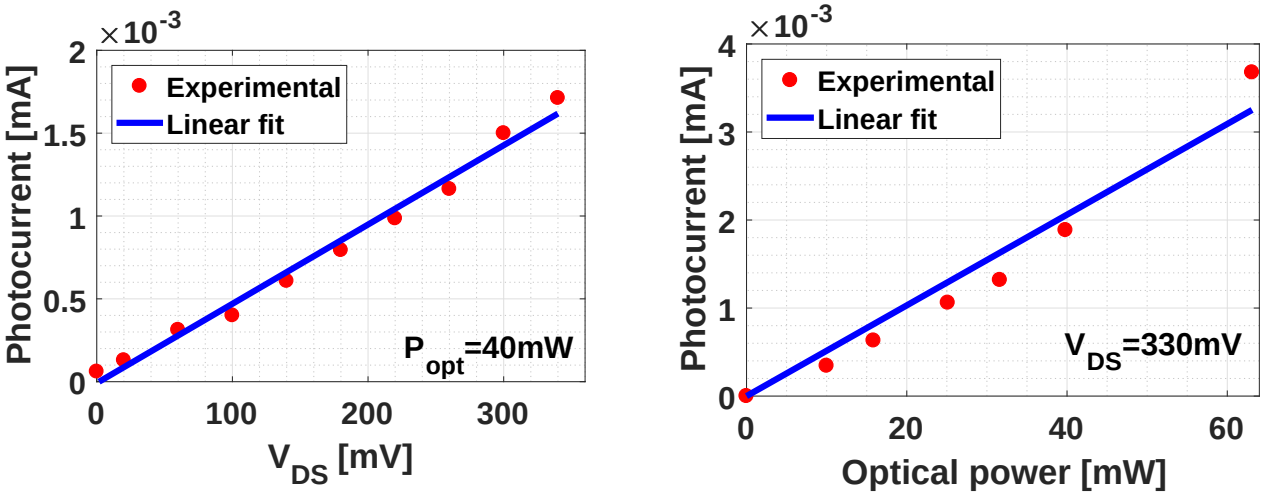

Fig. 5.3 a)Photocurrent as a function of V_{DS} under an optical beam power of 40 mW. b) Photocurrent as a function of the optical beam power, at V_{DS}=330 mV.

downconversion efficiency of $P_{eff} = -67dB$[1] was reached at V_{GS}=0.6V. For this optimum gate bias, figure 5.4b plots the downconversion efficiency as a function of f_{IF}. The device exhibits a 3dB bandwidth of 19.7 GHz. Figure 5.5a is a 2-dimensional color plot of the 67 GHz photocurrent as a function of the DC gate bias V_{GS} and the source-drain bias V_{DS}. We then added to the DC gate bias an electrical signal at f_{RF} = 10 GHz. The resulting downconverted photocurrent at f_{IF} = 57 GHz is plotted against the DC biases V_{DS} and V_{GS} in figure 5.5b. By differentiating the first 2-dimensional plot in figure 5.5a with respect to V_{GS}, we obtain a result (figure 5.5c) which resembles the one in figure 5.5b . This can also be observed in the plot in 5.5d, which plots both values as a function of V_{GS} and for a fixed V_{DS} = 200 mV. The curves of the downconverted photocurrent and of the derivative of the photocurrent can be superposed. A scaling factor of approximatively 6 has been applied to rescale the red curve.

These observations can be explained by carrying out a small-signal analysis, very similar to what has been done in Section 4.1. Let's consider the modulated optical power impinging on the photodetector, $P_{opt} = P_{cw} + P_{mod}sin(2\pi f_{opt}t)$, with P_{mod} the amplitude of the varying part of the optical power. The generated photocurrent is proportional to the impinging power P_{opt}; the proportionality constant is the responsivity R. For our device, R depends strongly on the gate voltage, as shown in the red curve of figure 5.2b, and is almost independent of the optical frequency f_{opt}, as it can be seen in figure 5.4a. Therefore, the photocurrent can be written in the form:

$$I_{ph}(V_{GS}) = R(V_{GS})(P_{cw} + P_{mod}sin(2\pi f_{opt}t)) \tag{5.1}$$

[1] see equation 2.11 for the definition of P_{eff}

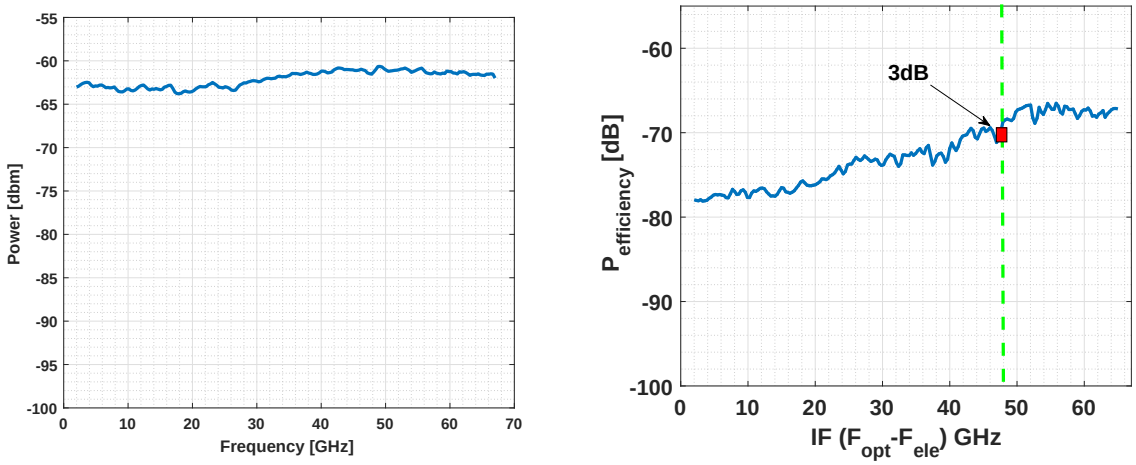

(a) (b)

Fig. 5.4 a)Maximum photodetected power at V_{GS}=0V, V_{DS}=330mV, as a function of the optical frequency f_{opt}. b) Downconversion efficiency loss at V_{GS}=0.6V, V_{DS}=330mV. In both plots, the optical power on the graphene channel is 60 mW.

By biasing the gate at a DC voltage $\bar{V}_{GS}$, and by applying to this terminal a small signal $\delta_{V_{GS}} sin(2\pi f_{ele} t)$, we can write the responsivity as:

$$R(V_{GS}) = R_{DC}(\bar{V}_{GS}) + \delta_{V_{GS}} \Delta_R sin(2\pi f_{ele} t) \tag{5.2}$$

where

$$\Delta_R = \beta(f_{ele}) \frac{dR(V_{GS})}{dV_{GS}}\Big|_{V_{GS}=\bar{V}_{GS}} \tag{5.3}$$

Here, we include a dependence on the injected electrical frequency through a frequency-dependent proportionality constant $\beta(f_{ele})$, as in Section 4.1. The total photocurrent has four terms:

$$\begin{aligned} I_{ph} = R_{DC}(\bar{V}_{GS}) P_{cw} + \delta_{V_{GS}} \Delta_R P_{cw} sin(2\pi f_{ele} t) + \\ R_{DC}(\bar{V}_{GS}) P_{mod} sin(2\pi f_{opt} t) + \delta_{V_{GS}} \Delta_R P_{mod} sin(2\pi f_{ele} t) sin(2\pi f_{opt} t) \end{aligned} \tag{5.4}$$

The first term in equation 5.4 is the DC photocurrent, the second term describe the DC photocurrent modulated by the electrical signal. The third term represents the photocurrent modulated at f_{opt}, shown in figure 5.4a. Finally, the last term of equation 5.4 describes the optoelectronic mixing. It is usefull to re-write it as it follows:

$$\begin{aligned} &\delta_{V_{GS}} \Delta_R P_{mod} sin(2\pi f_{ele} t) sin(2\pi f_{opt} t) = \\ &= \frac{1}{2} \delta_{V_{GS}} \Delta_R P_{mod} (cos(2\pi (f_{ele} - f_{opt}) t) - cos(2\pi (f_{ele} + f_{opt}) t)) \end{aligned} \tag{5.5}$$

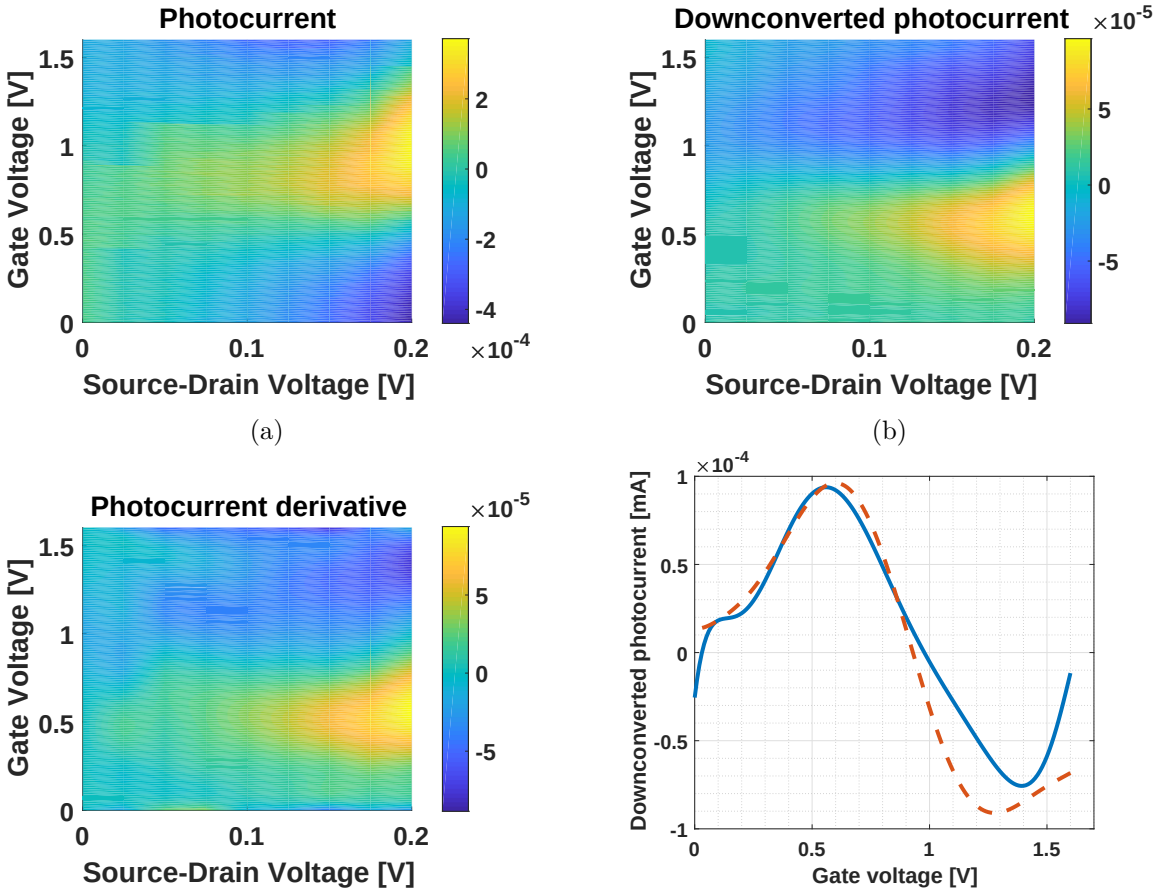

Fig. 5.5 a) Photocurrent map as a function of V_{GS} and V_{DS}. b) Downconverted photocurrent map as a function of V_{GS} and V_{DS}. c) Derivative of a) with respect to V_{GS}. d) Blue curve: cut of figure b) in correspondence of V_{DS}=200 mV. Red dashed curve: cut of figure c) in correspondence of V_{DS}=200 mV.

We recognize the two components at frequencies equals to the difference and the sum of of input frequencies f_{ele} and f_{opt}. The difference f_{opt}-f_{ele} is the previously introduced intermediate frequency f_{IF}.
Equation 5.5 shows that the mixed signal depends exclusively on Δ_R i.e. on the derivative of R with respect to the gate voltage, and not on the value of R itself, in accordance with the measurements shown in figure 5.5. The value of Δ_R is maximum for V_{GS} ∼0.6 V (figure 5.5d) i.e. in a region where the photocurrent changes in sign, as already shown in figure 5.2b. This change in sign of I_{ph} with respect to V_{GS} is essential to have optoelectronic mixing in graphene transistors, since it is responsible to the change of R with respect to V_{GS}. Therefore, the sharper is the transition between these two competing phenomena, the higher is the optoelectronic mixing downconversion efficiency. The control of the transition between the two different photocurrents could lead to a maximization of Δ_R, and in turn to a maximization of the performances of the presented device.

It was already observed that the device shows a 3dB bandwidth of 19.7 GHz when operated as a optoelectronic mixer (figure 5.4b). This behavior is mathematically modeled in the formula 5.3 by including the factor $\beta(f_{ele})$. To understand the optoelectronic mixing dependence on frequency f_{RF} and thus on IF (f_{opt} being fixed), one may consider a typical figure of merit of high frequency transistors, that is the transducer power gain [30], defined as:

$$G_T = \frac{P_{load}}{P_{avs}} \tag{5.6}$$

Where P_{load} is the power delivered to the load and P_{avs} is the power at the source. G_T coincides with S_{21} parameter when source and load are matched. This is the case in our measurement, where the power is delivered from the VNA's 50 Ω-source and measured on a 50 Ω receiver. We experimentally verified that the measured downconversion efficiency (which is, by definition, the transducer power gain G_T) trend is indeed close to the S_{21} parameters. Thus, an external impedance matching to enhance the S_{21} parameters could in turn enhance the efficiency of the device and increase the downconversion efficiency by maximing the power delivered by the transistor. These results are promising, considering that the structure has not been optimized yet. Moreover, only a small part of the 24 x 0.4 μm^2 channel was illuminated by the 2 μm diameter laser beam. We did not observe any saturation in the photodetected signal at the highest power available in our setup. Thus, illuminating a wider channel surface while maintaining the same optical power density should increase the downconversion efficiency. Moreover, impedance matching can be used to increase both bandwidth and downconversion efficiency.

5.5 Chapter conclusions

In conclusion, in this Chapter we demonstrated that a graphene high frequency transistor can be operated as an optoelectronic mixer for frequencies up to at least 67 GHz. The intrinsic bandwidth of the device operating as a photodetector exceeds 67 GHz, comparable to the best measured bandwidth in graphene based devices (>100 GHz) [66, 67]. The bandwidth of the device operated as an optoelectronic mixer is 19.7 GHz. A simple model, similar to the one already presented in Chapter 4, is presented to describe the measured downconversion efficiency.

Chapter 6

Conclusion and perspectives

6.1 Conclusions

This thesis work had as goal the demonstration of optoelectronic mixers based on graphene. First, a statistical analysis of the technological process used to fabricate graphene devices has been conducted. This has allowed to individuate the optimal technological steps, using as quality factors the key parameters that define the performances on our devices: contact resistance, charge carrier mobility and residual doping. Then we fabricated graphene-based coplanar waveguides (gCPWs) using the best technological process. Using these RF structures, we showed how a graphene photodetector can be used to obtain optoelectronic mixing. We showed that this is achieved by modulating the responsivity of the photodetector itself. This is possible in biased graphene because the responsivity is directly proportional to applied channel bias. By doing so, we demonstrated optoelectronic mixing up to 67 GHz. The statistical study of the RF structures has led to the individuation of the optimal device geometrical design and operating conditions in order to achieve the best performances.
Using the same design developed in Thales Research and Technology, a device with very high quality graphene encapsulated in Boron Nitride was fabricated at the École normale supérieure. It exhibits high mobility and low contact resistance. The performances of this device define the best downconversion efficiency obtained in graphene-based devices. Moreover, this device exhibits state-of the art performances used as photodetector.
Finally, we exploited the possibility of using graphene-based RF transistors as optoelectronic mixers. This work has been done in collaboration with IEMN in Lille, where the sample was fabricated. We showed that a graphene transistor can be operated as optoelectronic mixer by modulating the gate voltage, i.e. by switching the photoresponse from the bolometric to the photoconductive regime. We demonstrated an efficiency in optoelectronic mixing that is comparable with the first approach which makes use of gCPW.
The key parameters (contact resistance and mobility) impacting the performances of graphene-based devices still suffer from high dispersion. The experimental methodology of this work

finds its peculiarity in the extensive use of a statistical approach, which has been possible thanks to the automation of the measurement set-up that enabled the characterization of hundreds of devices. We believe that this approach, which is rare in works regarding graphene applications, is a necessary step in the prospective of a passage between demonstration and industrialization.

6.2 Perspectives

We have characterized devices based on CVD graphene exhibiting an average charge carrier mobility around 2500 $cm^2V^{-1}s^{-1}$. We showed that high mobility samples with low contact resistance can dramatically improve the performances of optoelectronic mixers. Nevertheless, these two parameters are not the only factors that limit the devices performances. The vertical illumination of the graphene channel with a laser beam is another important limiting factor. The absorption of light in graphene is 2.3%. This means that the 97.7% of the used power does not contribute to the generation of photocurrent in graphene. The use of integrated photonic waveguides can lead to near total absorption of light in bi-layer graphene and 60% absorption in monolayer graphene for 100 μm channel width [94], which could increase the responsivity of graphene phototodetectors by a factor of 40.
The extremely high bandwidth of graphene gCPW could also be exploited to implement other interesting functions in telecommunications and RADAR systems. For example, high frequency sampling can be achieved using a pulsed laser. Such photonic sampler (see figure 6.1) can then be implemented for analog-to-digital conversion.

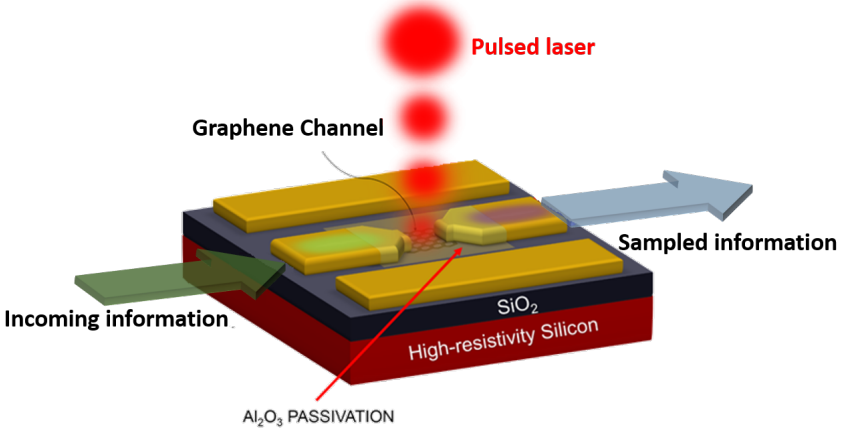

Fig. 6.1 Picture of the gCPW used as photonic sampler

Appendix A

RF Coplanar waveguide design and simulation

The RF Coplanar waveguides employed to demonstrate optoelectronic mixing have been designed using the software *CST Studio Design*. The signal-ground lines spacing has been chosen by taking into account the minimal probes signal-ground inter-distance (which was 100 μm) and the probes pads dimensions. This fixed a maximum distance of 25 μm for the signal-ground lines spacing. The line impedance value that was closest to 50 Ω corresponded to the superior limit (25 μm), for a signal width of 60 μm and a ground width of 250 μm. This is shown in figure A.1. The inset shows the quasi-TEM simulated mode of the waveguide. The simulated transmission parameters are shown in figure A.2, and are superposed to the

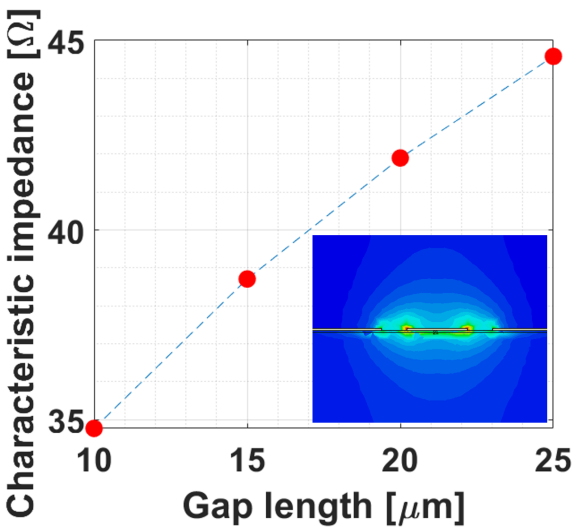

Fig. A.1 Impedance calculation of the CPW as a function of the source-ground gap length

measurement done on some test RF through-line structures realized on a substrate of the same type used for the fabrication of the gCPW. In our experiments, we applied a voltage to the substrate in order to obtain a gating effect on the graphene channel. In order to exclude any change in the transmission parameters not due to the only change in the graphene resistance,

we performed S-parameters measurements by applying 50 V to the central signal line. The results are reported in figure A.3. A very small change in the transmission parameter has been observed.

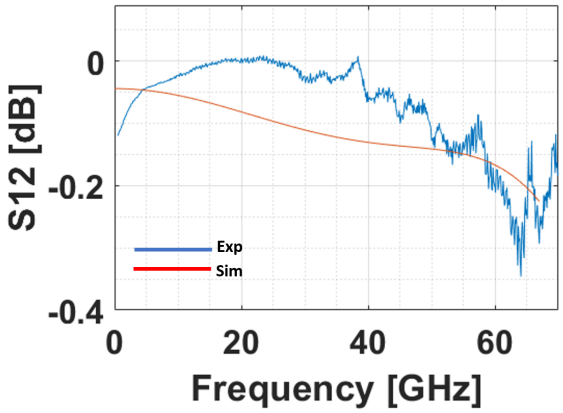

Fig. A.2 Transmission coefficient of the CPW with a signal-ground spacing of 25 μm, signal width of 60 μm and ground width of μm. The red curve shows the Simulation results, while the blue curve shows the measurement.

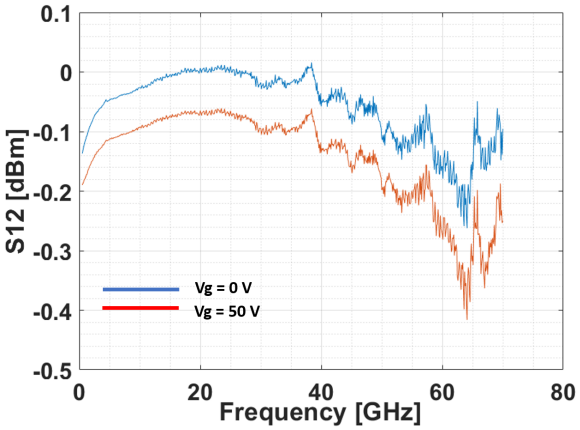

Fig. A.3 Transmission coefficient of the CPW with a signal-ground spacing of 25 μm, signal width of 60 μm and ground width of 250 μm under a signal-substrate voltage bias of 0V (red curve) and 50 V (blue curve).

Calculation of power absorption in the graphene channel

Figure A.4 shows the path of light passing through our device. To calculate the absorbed power in graphene (A in figure A.4) we used the transfer matrix method ([84, 95]. The needed material parameters (thickness and refractive index) are listed in figure A.4. A graphene thickness of 0.34 nm is used, that corresponds to the extension of graphene π orbitals out

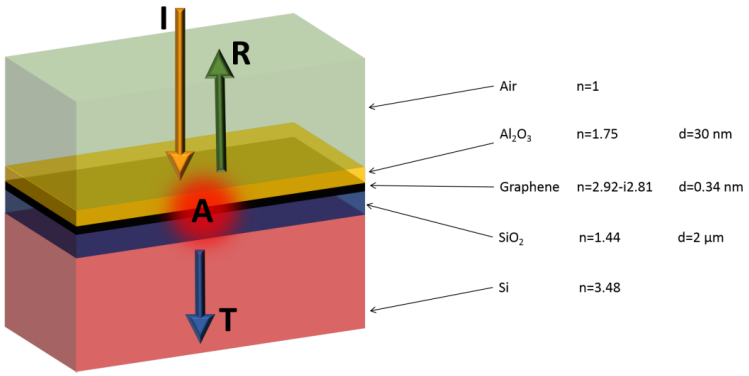

Fig. A.4 Path of light in the gCPW, constituted by a stack of different materials. The orange arrow indicates the total incident optical power(I), while the green and blue arrows indicate respectively the reflected (R) and transmitted (T) optical powers. The air and the silicon substrate thickness were considered as semi-infinite. The materials are indicated in the right part of the figure, together with the corresponding refractive indexes and thicknesses. These data were used to simulate the absorbed optical power (A) shown in figure A.5

of plane [96]. Only the refractive index of graphene is complex. We used the extinction coefficient value found in ref. [97] for non-doped graphene. The other materials (Al_2O_3, SiO_2 and high-resistivity silicon) present no absorption at 1.55 µm wavelength, thus exhibiting a real refractive index. Figure A.5 shows the calculation of optical absorption as a function of the SiO_2 layer thickness. With a 2μm SiO_2 thick layer (our case), the absorption is around 1.8 % of the total incident power (red point in figure A.5). A maximum peak of 3.3 % is reached at different thickness values.

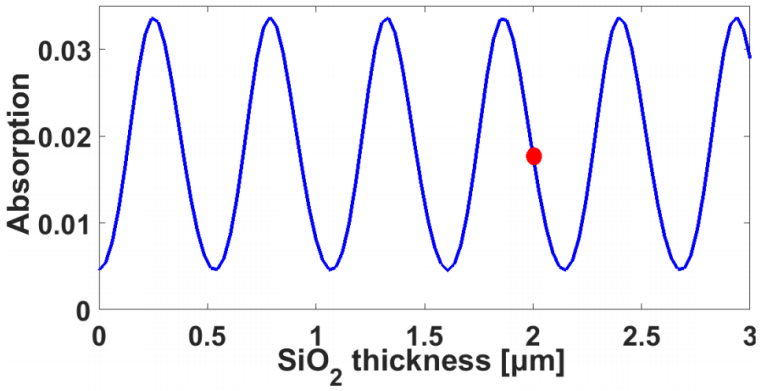

Fig. A.5 Simulation of the light absorption as a function of the SiO_2 layer thickness. In our devices, the thickness is equal to 2μm (red dot), and the corresponding absorption is around 1.8% of the total incident power.

Appendix B

2" Mask design and devices position

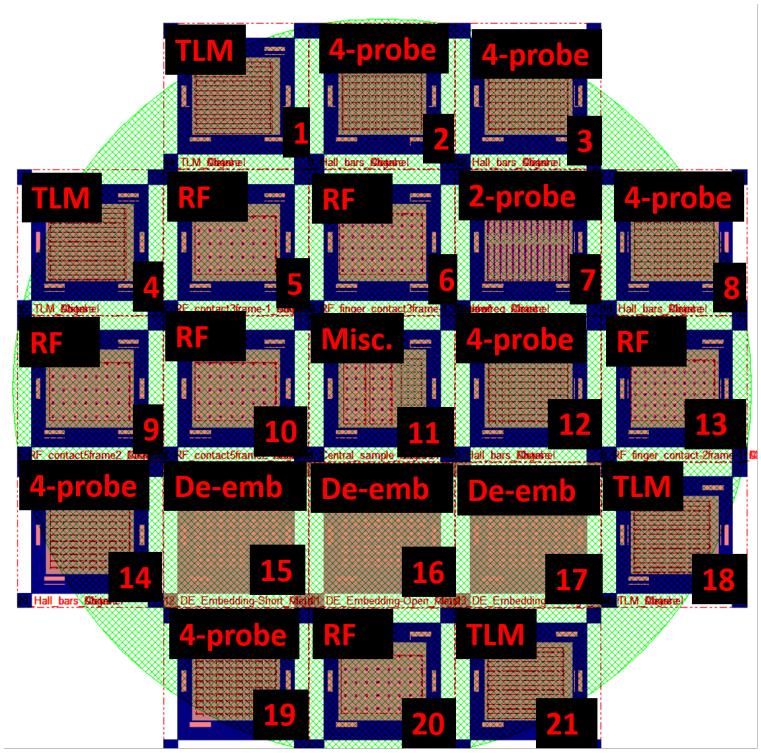

Fig. B.1 2" wafer with all the superposed lithographic masks

Figure B.1 shows the complete lithographic mask used to fabricate the devices on the 2" wafer. It is composed by 21 squares. The figure summarizes the type od devices contained in each square. A device is shown in figure B.2. The metal mask level is indicated in orange. The graphene etching level is indicated in blue. The pink level is used to etch the Al_2O_3 layer at the end of the process, in order to insure the contact between the probes pads and the metal lines.

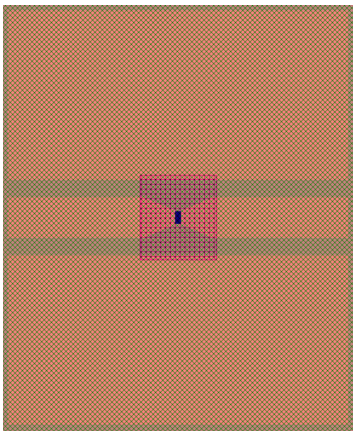

Fig. B.2 lithographic masks levels.

B.1 Raman Spectrum measurement

Figure S1 shows the Raman spectra of the graphene channel, before and after the overall lithographic process. The D/G peak ratio in the two spectra is very similar. According to Raman analysis, the devices fabrication process does not degrade the graphene structural quality.

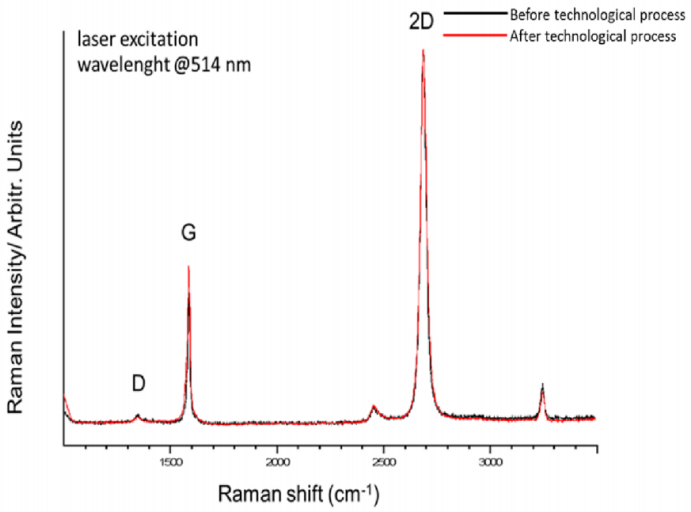

Fig. B.3 Raman spectrum before and after the overall fabrication process.

Appendix C

Change in conductivity calculation

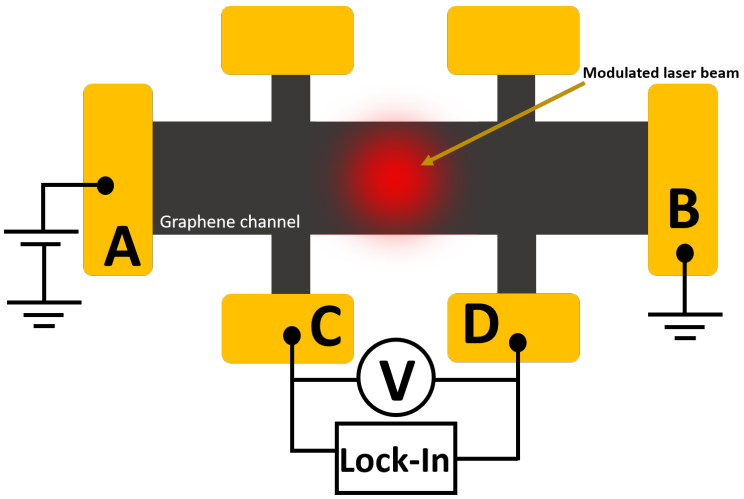

Fig. C.1 Experimental scheme for change in conductivity measurement on a four-probe structure.

The four-probe devices have been used in Chapter 3 to measure the local change in conductivity of the graphene channel caused by laser excitation. The extraction of this value is presented in the following. Referring to figure C.1, the total measured resistance, including the contact resistance can be expressed as:

$$R_{tot} = 2R_c + R_{AC} + R + R_{DB} \tag{C.1}$$

Where R_{AC} and R_{DB} is the resistance of the graphene channel outside the region defined by the internal probes. We define $\bar{R} = 2R_c + R_{AC} + R_{DB}$. So, The current flowing along the channel can be expressed as:

$$I = \frac{V_{AB}}{\bar{R} + R} \tag{C.2}$$

Where V_{AB} is the imposed voltage drop between the points A and B. Then, we express R as:

$$R = \sigma^{-1}\gamma \tag{C.3}$$

Where σ is the conductivity in the internal region, while $\gamma = l/W$, being l=10 μm and W=6 μm in our case (see Paragraph 3.1.1). The voltage drop between the points C and D is:

$$V_{CD}(\sigma) = \frac{V_{AB}}{\bar{R} + \frac{\gamma}{\sigma}} \frac{\gamma}{\sigma} \tag{C.4}$$

A varying sinusoidal laser excitation at frequency f_0 (in our case 700Hz, as specified in 3.2.3) generates a change in σ, which becomes:

$$\sigma = \sigma_{DC} + \Delta_\sigma + \Delta_\sigma sin(2\pi f_0 t) \tag{C.5}$$

Where σ_{DC} is the value of conductivity in dark conditions, Δ_σ is the non-varying part σ due to the mean optical power, and $\Delta_\sigma sin(2\pi f_0 t)$ is the varying of part of σ associated with the varying part of the optical power. The second term is equal to the amplitude of the third term, since the optical chopper performs a 100% optical power modulation.
if Δ_σ is small compared to σ (which is our case), the voltage drop between the internal contacts under laser excitation can be expressed as:

$$\widetilde{V_{CD}(\sigma)} = V_{CD}(\sigma_{DC} + \Delta_\sigma) + \Delta_\sigma \frac{dV_{CD}(\sigma)}{d\sigma}\Big|_{V_{CD}(\sigma)=V_{CD}(\sigma_{DC}+\Delta_\sigma)} sin(2\pi f_0 t) \tag{C.6}$$

The same can be done for I:

$$\widetilde{I(\sigma)} = I(\sigma_{DC} + \Delta_\sigma) + \Delta_\sigma \frac{dI(\sigma)}{d\sigma}\Big|_{I(\sigma)=I(\sigma_{DC}+\Delta_\sigma)} sin(2\pi f_0 t) \tag{C.7}$$

The constant parts of equation C.6 is read by the SMU connected to the internal contacts(M_A). The constant part of equation C.7 is read by the SMU connected to the external contacts(M_B). The magnitude of the varying part of equation C.6 is read by the Lock-In amplifier(M_C). The three unknowns [R, σ_{DC}, Δ_σ] are so found by solving the system of equations:

$$V_{CD}(\sigma_{DC} + \Delta_\sigma) = M_A \tag{C.8}$$

$$\Delta_\sigma \frac{dV_{CD}(\sigma)}{d\sigma}\Big|_{V_{CD}(\sigma)=V_{CD}(\sigma_{DC}+\Delta_\sigma)} = M_B \tag{C.9}$$

$$I(\sigma_{DC} + \Delta_\sigma) = M_C \tag{C.10}$$

Appendix D

List of acronyms

ALD	athomic layer deposition
CNP	charge neutrality point
CPW	coplanar waveguide
CVD	chemical vapour deposition
DFB	distributed feedback
DSB-SC	double sideband-suppressed carrier
DUT	device under test
EFDA	Erbium-doped fiber amplifier
gCPW	graphene coplanar waveguide
GFET	graphene field-effect transistor
IF	intermediate frequency
IR	infrared
LNA	low-noise amplifier
LO	local oscillator
MZM	Mach-Zehnder modulator
OEM	optoelectronic mixing
OSA	Optical spectrum analyzer
PMMA	poly methyl-methacrylate
RF	Radio frequency
SMU	source measure unit
TLM	transfer length method
VNA	vector signal analyzer

Appendix E

List of publications

[1] **Alberto Montanaro**, Sana Mzali, Jean-Paul Mazellier, Odile Bezencenet, Christian Larat, Stephanie Molin, Loïc Morvan, Pierre Legagneux, Daniel Dolfi, Bruno Dlubak, Pierre Seneor, Marie-Blandine Martin, Stephan Hofmann, John Robertson, Alba Centeno, and Amaia Zurutuza. *Thirty Gigahertz Optoelectronic Mixing in Chemical Vapor Deposited Graphene.* Nano Letters, 16(5):2988–2993, 2016.

[2] **Alberto Montanaro** , Sana Mzali , Jean-Paul Mazellier , Stephanie Molin , Christian Larat , Odile Bezencenet , Pierre Legagneux. *Optoelectronic mixing on CVD graphene up to 30 Gigahertz: analysis at high electrostatic doping.* Proc. SPIE 9932, Carbon Nanotubes, Graphene, and Emerging 2D Materials for Electronic and Photonic Devices IX, 99320Q (26 September 2016)

[3]**Alberto Montanaro**, Wei Wei, Domenico De Fazio, Ugo Sassi, Giancarlo Soavi, Andrea C. Ferrari, Henri Happy, Pierre Legagneux, Emiliano Pallecchi. *Optoelectronic mixing with high frequency graphene transistors* (*under submission*)

[4] Sana Mzali, **Alberto Montanaro**, Stéphane Xavier, Bernard Servet, Jean-Paul Mazellier, Odile Bezencenet, Pierre Legagneux, Maëlis Piquemal-Banci, Regina Galceran, Bruno Dlubak, Pierre Seneor, Marie-Blandine Martin, Stephan Hofmann, John Robertson, Costel-Sorin Cojocaru, Alba Centeno, and Amaia Zurutuza. *Stabilizing a graphene platform toward discrete components.* Applied Physics Letters, 109(25):253110, 2016.

[5] Paolo Bondavalli, Marie-Blandine Martin, Louiza Hamidouche, **Alberto Montanaro**, Aikaterini-Flora Trompeta, Costas Adam Charitidis *Nano-Graphitic based Non-Volatile Memories Fabricated by the Dynamic Spray-Gun Deposition Method.* Micromachines, 10(2):95, 2019.

References

[1] Tim Brown. Talga Resources makes first delivery of graphene coating product.

[2] A H Castro Neto, F Guinea, N M R Peres, K S Novoselov, and A K Geim. The electronic properties of graphene. *Rev. Mod. Phys.*, 81(1):109–162, jan 2009.

[3] Marcus Freitag, Tony Low, Fengnian Xia, and Phaedon Avouris. Photoconductivity of biased graphene. *Nature Photonics*, 7:53, dec 2012.

[4] Jon B Hagen. *Radio-Frequency Electronics: Circuits and Applications*. Cambridge University Press, 2 edition, 2009.

[5] M A Richards, W A Holm, and J Scheer. *Principles of Modern Radar: Basic Principles*. Electromagnetics and Radar. Institution of Engineering and Technology, 2010.

[6] Loïc Morvan, Ngoc D Lai, Daniel Dolfi, Jean-Pierre Huignard, Marc Brunel, Fabien Bretenaker, and Albert Le Floch. Building blocks for a two-frequency laser lidar-radar: a preliminary study. *Appl. Opt.*, 41(27):5702–5712, sep 2002.

[7] William C Ruff, John D Bruno, Stephen W Kennerly, Ken Ritter, Paul H Shen, Barry L Stann, Michael R Stead, Zoltan G Sztankay, and Mary S Tobin. Self-mixing detector candidates for an FM/cw ladar architecture. volume 4035, pages 4011–4035. Spie Proceedings, 2000.

[8] A Chizh and S Malyshev. Fiber-optic system for local-oscillator signal distribution in active phased arrays. In *2014 11th European Radar Conference*, pages 439–442, 2014.

[9] Thomas Mueller, Fengnian Xia, and Phaedon Avouris. Graphene photodetectors for high-speed optical communications. *Nature Photonics*, 4:297, mar 2010.

[10] P R Wallace. The Band Theory of Graphite. *Phys. Rev.*, 71(9):622–634, may 1947.

[11] H P Boehm, R Setton, and E Stumpp. Nomenclature and terminology of graphite intercalation compounds. *Carbon*, 24(2):241–245, 1986.

[12] Claire Berger, Zhimin Song, Tianbo Li, Xuebin Li, Asmerom Y Ogbazghi, Rui Feng, Zhenting Dai, Alexei N Marchenkov, Edward H Conrad, Phillip N First, and Walt A de Heer. Ultrathin Epitaxial Graphite: 2D Electron Gas Properties and a Route toward Graphene-based Nanoelectronics. *The Journal of Physical Chemistry B*, 108(52):19912–19916, 2004.

[13] K S Novoselov, A K Geim, S V Morozov, D Jiang, Y Zhang, S V Dubonos, I V Grigorieva, and A A Firsov. Electric Field Effect in Atomically Thin Carbon Films. *Science*, 306(5696):666–669, 2004.

[14] F Bonaccorso, Z Sun, T Hasan, and A C Ferrari. Graphene photonics and optoelectronics. *Nature Photonics*, 4:611, aug 2010.

[15] G I Zebrev. Graphene Field Effect Transistors: Diffusion-Drift Theory. In Sergey Mikhailov, editor, *Physics and Applications of Graphene*, chapter 23. IntechOpen, Rijeka, 2011.

[16] E Pallecchi, A C Betz, J Chaste, G Fève, B Huard, T Kontos, J.-M. Berroir, and B Pla\ifmmode \mbox\cc\else ç\fiais. Transport scattering time probed through rf admittance of a graphene capacitor. *Phys. Rev. B*, 83(12):125408, mar 2011.

[17] R R Nair, P Blake, A N Grigorenko, K S Novoselov, T J Booth, T Stauber, N M R Peres, and A K Geim. Fine Structure Constant Defines Visual Transparency of Graphene. *Science*, 320(5881):1308, 2008.

[18] P Plochocka, C Faugeras, M Orlita, M L Sadowski, G Martinez, M Potemski, M O Goerbig, J.-N. Fuchs, C Berger, and W A de Heer. High-Energy Limit of Massless Dirac Fermions in Multilayer Graphene using Magneto-Optical Transmission Spectroscopy. *Phys. Rev. Lett.*, 100(8):87401, feb 2008.

[19] Andrea C Ferrari, Francesco Bonaccorso, Vladimir Fal'ko, Konstantin S Novoselov, Stephan Roche, Peter Bøggild, Stefano Borini, Frank H L Koppens, Vincenzo Palermo, Nicola Pugno, José A Garrido, Roman Sordan, Alberto Bianco, Laura Ballerini, Maurizio Prato, Elefterios Lidorikis, Jani Kivioja, Claudio Marinelli, Tapani Ryhänen, Alberto Morpurgo, Jonathan N Coleman, Valeria Nicolosi, Luigi Colombo, Albert Fert, Mar Garcia-Hernandez, Adrian Bachtold, Grégory F Schneider, Francisco Guinea, Cees Dekker, Matteo Barbone, Zhipei Sun, Costas Galiotis, Alexander N Grigorenko, Gerasimos Konstantatos, Andras Kis, Mikhail Katsnelson, Lieven Vandersypen, Annick Loiseau, Vittorio Morandi, Daniel Neumaier, Emanuele Treossi, Vittorio Pellegrini, Marco Polini, Alessandro Tredicucci, Gareth M Williams, Byung Hee Hong, Jong-Hyun Ahn, Jong Min Kim, Herbert Zirath, Bart J van Wees, Herre van der Zant, Luigi Occhipinti, Andrea Di Matteo, Ian A Kinloch, Thomas Seyller, Etienne Quesnel, Xinliang Feng, Ken Teo, Nalin Rupesinghe, Pertti Hakonen, Simon R T Neil, Quentin Tannock, Tomas Löfwander, and Jari Kinaret. Science and technology roadmap for graphene, related two-dimensional crystals, and hybrid systems. *Nanoscale*, 7(11):4598–4810, 2015.

[20] F H L Koppens, T Mueller, Ph. Avouris, A C Ferrari, M S Vitiello, and M Polini. Photodetectors based on graphene, other two-dimensional materials and hybrid systems. *Nature Nanotechnology*, 9:780, oct 2014.

[21] Sana Mzali. *Méthodologie de fabrication de transistors à base de Graphène : application aux composants optoélectroniques hyperfréquences*. PhD thesis, 2016.

[22] Sukang Bae, Hyeongkeun Kim, Youngbin Lee, Xiangfan Xu, Jae-Sung Park, Yi Zheng, Jayakumar Balakrishnan, Tian Lei, Hye Ri Kim, Young Il Song, Young-Jin Kim, Kwang S Kim, Barbaros Özyilmaz, Jong-Hyun Ahn, Byung Hee Hong, and Sumio Iijima. Roll-to-roll production of 30-inch graphene films for transparent electrodes. *Nature Nanotechnology*, 5:574, jun 2010.

[23] Xuesong Li, Weiwei Cai, Jinho An, Seyoung Kim, Junghyo Nah, Dongxing Yang, Richard Piner, Aruna Velamakanni, Inhwa Jung, Emanuel Tutuc, Sanjay K Banerjee, Luigi Colombo, and Rodney S Ruoff. Large-Area Synthesis of High-Quality and Uniform Graphene Films on Copper Foils. *Science*, 324(5932):1312–1314, 2009.

[24] Francesco Bonaccorso, Antonio Lombardo, Tawfique Hasan, Zhipei Sun, Luigi Colombo, and Andrea C Ferrari. Production and processing of graphene and 2d crystals. *Materials Today*, 15(12):564–589, 2012.

[25] Graphenea. Graphenea website "https://www.graphenea.com/".

[26] Chang Goo Kang, Young Gon Lee, Sang Kyung Lee, Eunji Park, Chunhum Cho, Sung Kwan Lim, Hyeon Jun Hwang, and Byoung Hun Lee. Mechanism of the effects of low temperature Al2O3 passivation on graphene field effect transistors. *Carbon*, 53:182–187, 2013.

[27] Young Gon Lee, Chang Goo Kang, Chunhum Cho, Yonghun Kim, Hyeon Jun Hwang, and Byoung Hun Lee. Quantitative analysis of hysteretic reactions at the interface of graphene and SiO2 using the short pulse I–V method. *Carbon*, 60:453–460, 2013.

[28] Kosuke Nagashio and Akira Toriumi. Density-of-States Limited Contact Resistance in Graphene Field-Effect Transistors. *Japanese Journal of Applied Physics*, 50(7):70108, jul 2011.

[29] B Huard, N Stander, J A Sulpizio, and D Goldhaber-Gordon. Evidence of the role of contacts on the observed electron-hole asymmetry in graphene. *Phys. Rev. B*, 78(12):121402, sep 2008.

[30] D M Pozar. *Microwave Engineering*. Wiley, 2012.

[31] Keizo Inagaki, Tetsuya Kawanishi, and Masayuki Izutsu. Optoelectronic frequency response measurement of photodiodes by using high-extinction ratio optical modulator. *IEICE Electronics Express*, 9(4):220–226, 2012.

[32] Albert Gleissner. Power Calibration of Vector Network Analyzer R&S®ZVR. Technical report, Rohde & Schwarz.

[33] Hideki Hirai, Hideaki Tsuchiya, Yoshinari Kamakura, Nobuya Mori, and Matsuto Ogawa. Electron mobility calculation for graphene on substrates. *Journal of Applied Physics*, 116(8):83703, 2014.

[34] W Gannett, W Regan, K Watanabe, T Taniguchi, M F Crommie, and A Zettl. Boron nitride substrates for high mobility chemical vapor deposited graphene. *Applied Physics Letters*, 98(24):242105, 2011.

[35] M Poljak, T Suligoj, and K L Wang. Influence of substrate type and quality on carrier mobility in graphene nanoribbons. *Journal of Applied Physics*, 114(5):53701, 2013.

[36] Carlos Alvarado Chavarin, Abhay A Sagade, Daniel Neumaier, Gerd Bacher, and Wolfgang Mertin. On the origin of contact resistances in graphene devices fabricated by optical lithography. *Applied Physics A*, 122(2):58, jan 2016.

[37] L Wang, I Meric, P Y Huang, Q Gao, Y Gao, H Tran, T Taniguchi, K Watanabe, L M Campos, D A Muller, J Guo, P Kim, J Hone, K L Shepard, and C R Dean. One-Dimensional Electrical Contact to a Two-Dimensional Material. *Science*, 342(6158):614–617, 2013.

[38] W Wei, D D Fazio, U Sassi, A C Ferrari, E Pallecchi, and H Happy. Graphene field effect transistors with optimized contact resistance for current gain. In *2017 75th Annual Device Research Conference (DRC)*, pages 1–2, jun 2017.

[39] Seyoung Kim, Junghyo Nah, Insun Jo, Davood Shahrjerdi, Luigi Colombo, Zhen Yao, Emanuel Tutuc, and Sanjay K Banerjee. Realization of a high mobility dual-gated graphene field-effect transistor with Al2O3 dielectric. *Applied Physics Letters*, 94(6):62107, 2009.

[40] Hua Zhong, Zhiyong Zhang, Haitao Xu, Chenguang Qiu, and Lian-Mao Peng. Comparison of mobility extraction methods based on field-effect measurements for graphene. *AIP Advances*, 5(5):57136, 2015.

[41] Sana Mzali, Alberto Montanaro, Stéphane Xavier, Bernard Servet, Jean-Paul Mazellier, Odile Bezencenet, Pierre Legagneux, Maëlis Piquemal-Banci, Regina Galceran, Bruno Dlubak, Pierre Seneor, Marie-Blandine Martin, Stephan Hofmann, John Robertson, Costel-Sorin Cojocaru, Alba Centeno, and Amaia Zurutuza. Stabilizing a graphene platform toward discrete components. *Applied Physics Letters*, 109(25):253110, 2016.

[42] Vincent E Dorgan, Myung-Ho Bae, and Eric Pop. Mobility and saturation velocity in graphene on SiO2. *Applied Physics Letters*, 97(8):82112, 2010.

[43] Reginald Aubrey Fessenden. Wireless Signaling, aug 1902.

[44] E H Armstrong. A New System of Short Wave Amplification. *Proceedings of the Institute of Radio Engineers*, 9(1):3–11, feb 1921.

[45] Skolnik. *Introduction to Radar Systems*. Tata McGraw Hill, 2001.

[46] Q Gu. *RF System Design of Transceivers for Wireless Communications*. Springer US, 2006.

[47] Paolo Ghelfi, Francesco Laghezza, Filippo Scotti, Giovanni Serafino, Amerigo Capria, Sergio Pinna, Daniel Onori, Claudio Porzi, Mirco Scaffardi, Antonio Malacarne, Valeria Vercesi, Emma Lazzeri, Fabrizio Berizzi, and Antonella Bogoni. A fully photonics-based coherent radar system. *Nature*, 507:341, mar 2014.

[48] Valeria Vercesi, Daniel Onori, Francesco Laghezza, Filippo Scotti, Antonella Bogoni, and Mirco Scaffardi. Frequency-agile dual-frequency lidar for integrated coherent radar-lidar architectures. *Opt. Lett.*, 40(7):1358–1361, apr 2015.

[49] J P Dakin and R G W Brown. *Handbook of Optoelectronics: Enabling Technologies (Volume Two)*. Series in Optics and Optoelectronics. CRC Press, 2017.

[50] J Wenger. Automotive mm-wave radar: status and trends in system design and technology. *IET Conference Proceedings*, pages 1–1(1), jan 1998.

[51] A M Niknejad and H Hashemi. *mm-Wave Silicon Technology: 60 GHz and Beyond*. Integrated Circuits and Systems. Springer US, 2008.

[52] W Roh, J Seol, J Park, B Lee, J Lee, Y Kim, J Cho, K Cheun, and F Aryanfar. Millimeter-wave beamforming as an enabling technology for 5G cellular communications: theoretical feasibility and prototype results. *IEEE Communications Magazine*, 52(2):106–113, feb 2014.

[53] T S Rappaport, S Sun, R Mayzus, H Zhao, Y Azar, K Wang, G N Wong, J K Schulz, M Samimi, and F Gutierrez. Millimeter Wave Mobile Communications for 5G Cellular: It Will Work! *IEEE Access*, 1:335–349, 2013.

[54] J G Andrews, S Buzzi, W Choi, S V Hanly, A Lozano, A C K Soong, and J C Zhang. What Will 5G Be? *IEEE Journal on Selected Areas in Communications*, 32(6):1065–1082, jun 2014.

[55] Chang-Soon Choi, Jun-Hyuk Seo, Woo-Young Choi, H Kamitsuna, M Ida, and K Kurishima. 60-GHz bidirectional radio-on-fiber links based on InP-InGaAs HPT optoelectronic mixers. *IEEE Photonics Technology Letters*, 17(12):2721–2723, dec 2005.

[56] Efthymios Rouvalis, Martyn J Fice, Cyril C Renaud, and Alwyn J Seeds. Optoelectronic detection of millimetre-wave signals with travelling-wave uni-travelling carrier photodiodes. *Opt. Express*, 19(3):2079–2084, jan 2011.

[57] Hyo Soon Kang and Woo-Young Choi. CMOS-compatible 60 GHz harmonic optoelectronic mixer. In *2007 IEEE MTT-S International Microwave Symposium Digest*, pages 233–236, 2007.

[58] Filippo Pizzocchero, Lene Gammelgaard, Bjarke S Jessen, José M Caridad, Lei Wang, James Hone, Peter Bøggild, and Timothy J Booth. The hot pick-up technique for batch assembly of van der Waals heterostructures. *Nature Communications*, 7:11894, jun 2016.

[59] Megan A Yamoah, Wenmin Yang, Eric Pop, and David Goldhaber-Gordon. High-Velocity Saturation in Graphene Encapsulated by Hexagonal Boron Nitride. *ACS Nano*, 11(10):9914–9919, oct 2017.

[60] Luca Banszerus, Michael Schmitz, Stephan Engels, Jan Dauber, Martin Oellers, Federica Haupt, Kenji Watanabe, Takashi Taniguchi, Bernd Beschoten, and Christoph Stampfer. Ultrahigh-mobility graphene devices from chemical vapor deposition on reusable copper. *Science Advances*, 1(6), 2015.

[61] E Pallecchi, F Lafont, V Cavaliere, F Schopfer, D Mailly, W Poirier, and A Ouerghi. High Electron Mobility in Epitaxial Graphene on 4H-SiC(0001) via post-growth annealing under hydrogen. *Scientific Reports*, 4:4558, apr 2014.

[62] M Breusing, S Kuehn, T Winzer, E Mali\ifmmode \acutec\else ć\fi, F Milde, N Severin, J P Rabe, C Ropers, A Knorr, and T Elsaesser. Ultrafast nonequilibrium carrier dynamics in a single graphene layer. *Phys. Rev. B*, 83(15):153410, apr 2011.

[63] Andreas Pospischil, Markus Humer, Marco M Furchi, Dominic Bachmann, Romain Guider, Thomas Fromherz, and Thomas Mueller. CMOS-compatible graphene photodetector covering all optical communication bands. *Nature Photonics*, 7:892, sep 2013.

[64] Daniel Schall, Daniel Neumaier, Muhammad Mohsin, Bartos Chmielak, Jens Bolten, Caroline Porschatis, Andreas Prinzen, Christopher Matheisen, Wolfgang Kuebart, Bernhard Junginger, Wolfgang Templ, Anna Lena Giesecke, and Heinrich Kurz. 50 GBit/s Photodetectors Based on Wafer-Scale Graphene for Integrated Silicon Photonic Communication Systems. *ACS Photonics*, 1(9):781–784, 2014.

[65] Fengnian Xia, Thomas Mueller, Yu-ming Lin, Alberto Valdes-Garcia, and Phaedon Avouris. Ultrafast graphene photodetector. *Nature Nanotechnology*, 4:839, oct 2009.

[66] Daniel Schall, Caroline Porschatis, Martin Otto, and Daniel Neumaier. Graphene photodetectors with a bandwidth larger than 76 GHz fabricated in a 6 inch wafer process line. *Journal of Physics D: Applied Physics*, 50(12):124004, feb 2017.

[67] Daniel Schall, Emiliano Pallecchi, Guillaume Ducournau, Vanessa Avramovic, Martin Otto, and Daniel Neumaier. Record high bandwidth integrated graphene photodetectors for communication beyond 180 Gb/s. In *Optical Fiber Communication Conference*, page M2I.4. Optical Society of America, 2018.

[68] Ren-Jye Shiue, Yuanda Gao, Yifei Wang, Cheng Peng, Alexander D Robertson, Dmitri K Efetov, Solomon Assefa, Frank H L Koppens, James Hone, and Dirk Englund. High-Responsivity Graphene–Boron Nitride Photodetector and Autocorrelator in a Silicon Photonic Integrated Circuit. *Nano Letters*, 15(11):7288–7293, 2015.

[69] X Mao, C Cheng, B Huang, Z Zhang, S Gan, H Chen, and H Chen. Optoelectronic Mixer Based on Graphene FET. *IEEE Electron Device Letters*, 36(3):253–255, mar 2015.

[70] Alberto Montanaro, Sana Mzali, Jean-Paul Mazellier, Odile Bezencenet, Christian Larat, Stephanie Molin, Loïc Morvan, Pierre Legagneux, Daniel Dolfi, Bruno Dlubak, Pierre Seneor, Marie-Blandine Martin, Stephan Hofmann, John Robertson, Alba Centeno, and Amaia Zurutuza. Thirty Gigahertz Optoelectronic Mixing in Chemical Vapor Deposited Graphene. *Nano Letters*, 16(5):2988–2993, 2016.

[71] Marie-Blandine Martin, Bruno Dlubak, Robert S Weatherup, Heejun Yang, Cyrile Deranlot, Karim Bouzehouane, Frédéric Petroff, Abdelmadjid Anane, Stephan Hofmann, John Robertson, Albert Fert, and Pierre Seneor. Sub-nanometer Atomic Layer Deposition for Spintronics in Magnetic Tunnel Junctions Based on Graphene Spin-Filtering Membranes. *ACS Nano*, 8(8):7890–7895, 2014.

[72] Abhay A Sagade, Daniel Neumaier, Daniel Schall, Martin Otto, Amaia Pesquera, Alba Centeno, Amaia Zurutuza Elorza, and Heinrich Kurz. Highly air stable passivation of graphene based field effect devices. *Nanoscale*, 7(8):3558–3564, 2015.

[73] Kuan-Chun Lin, Ming-Yang Li, D C Ling, C C Chi, and Jeng-Chung Chen. Evolution of hot carrier dynamics in graphene with the Fermi level tuned across the Dirac point. *Phys. Rev. B*, 91(12):125440, mar 2015.

[74] Isabella Gierz, Jesse C Petersen, Matteo Mitrano, Cephise Cacho, I C Edmond Turcu, Emma Springate, Alexander Stöhr, Axel Köhler, Ulrich Starke, and Andrea Cavalleri. Snapshots of non-equilibrium Dirac carrier distributions in graphene. *Nature Materials*, 12:1119, oct 2013.

[75] D Brida, A Tomadin, C Manzoni, Y J Kim, A Lombardo, S Milana, R R Nair, K S Novoselov, A C Ferrari, G Cerullo, and M Polini. Ultrafast collinear scattering and carrier multiplication in graphene. *Nature Communications*, 4:1987, jun 2013.

[76] Jared H Strait, Haining Wang, Shriram Shivaraman, Virgil Shields, Michael Spencer, and Farhan Rana. Very Slow Cooling Dynamics of Photoexcited Carriers in Graphene Observed by Optical-Pump Terahertz-Probe Spectroscopy. *Nano Letters*, 11(11):4902–4906, 2011.

[77] R Bistritzer and A H MacDonald. Electronic Cooling in Graphene. *Phys. Rev. Lett.*, 102(20):206410, may 2009.

[78] Paul A George, Jared Strait, Jahan Dawlaty, Shriram Shivaraman, Mvs Chandrashekhar, Farhan Rana, and Michael G Spencer. Ultrafast Optical-Pump Terahertz-Probe Spectroscopy of the Carrier Relaxation and Recombination Dynamics in Epitaxial Graphene. *Nano Letters*, 8(12):4248–4251, 2008.

[79] S A Awan, A Lombardo, A Colli, G Privitera, T S Kulmala, J M Kivioja, M Koshino, and A C Ferrari. Transport conductivity of graphene at {RF} and microwave frequencies. *2D Materials*, 3(1):15010, feb 2016.

[80] G Dambrine, A Cappy, F Heliodore, and E Playez. A new method for determining the FET small-signal equivalent circuit. *IEEE Transactions on Microwave Theory and Techniques*, 36(7):1151–1159, jul 1988.

[81] H Cho and D E Burk. A three-step method for the de-embedding of high-frequency S-parameter measurements. *IEEE Transactions on Electron Devices*, 38(6):1371–1375, jun 1991.

[82] H Graef, D Mele, M Rosticher, L Banszerus, C Stampfer, T Taniguchi, K Watanabe, E Bocquillon, G Fève, J-M Berroir, E H T Teo, and B Plaçais. Ultra-long wavelength Dirac plasmons in graphene capacitors. *Journal of Physics: Materials*, 1(1):01LT02, sep 2018.

[83] Hosang Yoon, Carlos Forsythe, Lei Wang, Nikolaos Tombros, Kenji Watanabe, Takashi Taniguchi, James Hone, Philip Kim, and Donhee Ham. Measurement of collective dynamical mass of Dirac fermions in graphene. *Nature Nanotechnology*, 9:594, jun 2014.

[84] B E A Saleh and M C Teich. *Fundamentals of Photonics*. Wiley Series in Pure and Applied Optics. Wiley, 2007.

[85] Quentin Wilmart. *Engineering doping profils in graphene : from Dirac fermion oprtics to high frequency electronics*. PhD thesis, École normale supérieure, 2015.

[86] Deji Akinwande, Nicholas Petrone, and James Hone. Two-dimensional flexible nanoelectronics. *Nature Communications*, 5:5678, dec 2014.

[87] F Schwierz, J Pezoldt, and R Granzner. Two-dimensional materials and their prospects in transistor electronics. *Nanoscale*, 7(18):8261–8283, 2015.

[88] K S Novoselov, V I Falko, L Colombo, P R Gellert, M G Schwab, and K Kim. A roadmap for graphene. *Nature*, 490:192, oct 2012.

[89] Wei Wei, Emiliano Pallecchi, Samiul Haque, Stefano Borini, Vanessa Avramovic, Alba Centeno, Zurutuza Amaia, and Henri Happy. Mechanically robust 39 GHz cut-off frequency graphene field effect transistors on flexible substrates. *Nanoscale*, 8(29):14097–14103, 2016.

[90] Zelei Guo, Rui Dong, Partha Sarathi Chakraborty, Nelson Lourenco, James Palmer, Yike Hu, Ming Ruan, John Hankinson, Jan Kunc, John D Cressler, Claire Berger, and Walt A de Heer. Record Maximum Oscillation Frequency in C-Face Epitaxial Graphene Transistors. *Nano Letters*, 13(3):942–947, mar 2013.

[91] Nicholas Petrone, Inanc Meric, James Hone, and Kenneth L Shepard. Graphene Field-Effect Transistors with Gigahertz-Frequency Power Gain on Flexible Substrates. *Nano Letters*, 13(1):121–125, jan 2013.

[92] E Pallecchi, C Benz, A C Betz, H v. Löhneysen, B Plaçais, and R Danneau. Graphene microwave transistors on sapphire substrates. *Applied Physics Letters*, 99(11):113502, 2011.

[93] W Wei, X Zhou, G Deokar, H Kim, M M Belhaj, E Galopin, E Pallecchi, D Vignaud, and H Happy. Graphene FETs With Aluminum Bottom-Gate Electrodes and Its Natural Oxide as Dielectrics. *IEEE Transactions on Electron Devices*, 62(9):2769–2773, 2015.

[94] Simone Schuler, Daniel Schall, Daniel Neumaier, Lukas Dobusch, Ole Bethge, Benedikt Schwarz, Michael Krall, and Thomas Mueller. Controlled Generation of a p–n Junction in a Waveguide Integrated Graphene Photodetector. *Nano Letters*, 16(11):7107–7112, 2016.

[95] P Blake, E W Hill, A H Castro Neto, K S Novoselov, D Jiang, R Yang, T J Booth, and A K Geim. Making graphene visible. *Applied Physics Letters*, 91(6):63124, 2007.

[96] K S Pitzer. The Nature of the Chemical Bond and the Structure of Molecules and Crystals: An Introduction to Modern Structural Chemistry. *Journal of the American Chemical Society*, 82(15):4121, 1960.

[97] F Xu, S Das, Y Gong, Q Liu, H.-C. Chien, H.-Y. Chiu, J Wu, and R Hui. Complex refractive index tunability of graphene at 1550 nm wavelength. *Applied Physics Letters*, 106(3):31109, 2015.

RÉSUMÉ

Depuis les premières expérimentations effectuées en 2004 par Andrej Geim et Konstantin Novosëlov, le graphène a été largement étudié dans le domaine de la photonique et de l'optoélectronique. Ses extraordinaires propriétés incluent une très grande mobilité des porteurs de charge et une absorption large bande y compris à la longueur d'onde typique des télécommunications (1.55 µm). Ces propriétés rendent ce matériau très prometteur pour les composants optoélectroniques utilisées dans les RADAR ou pour les télécommunications. En outre, comme le graphène peut être intégré sur une plateforme silicium, il apparait comme un potentiel substitut aux matériaux III-V.
Le domaine d'application des composants à base de graphène a considérablement augmenté au cours de ces dernières années. Néanmoins, comme les paramètres clés impactant les performances des dispositifs optoélectroniques basé sur le graphène ne sont pas encore bien contrôlés, le nombre d'implémentations à l'échelle industrielle reste toujours très limité. Dans ce travail de thèse, le mélange optoélectronique, une fonction très utilisée dans les systèmes RADAR et de télécommunications, est démontré avec des dispositifs basées sur le graphène. Dans un premier temps, nous avons effectué une étude statistique de la mobilité des porteurs de charge, du dopage résiduel et des résistances de contact. Cette étude a permis d'identifier le meilleur procédé technologique et les meilleures méthodes de caractérisation (choix des composants de test et des méthodes d'extraction des paramètres). En utilisant ce procédé optimisé, nous avons réalisé la première démonstration d'un mélangeur optoélectronique hyperfréquence basé sur le graphène. Puis, une étude approfondie de nombreux dispositifs RF avec différentes géométries a permis d'identifier les meilleures conditions opératives et le meilleur design. A l'aide de lignes coplanaires mais aussi de transistors hyperfréquence à base de graphène, nous avons démontré le mélange optoélectronique à des fréquences allant jusqu'à 67 GHz. Ce travail a été principalement mené en utilisant des méthodes statistiques. A cette fin, j'ai développé une mesure automatisée qui a permis de mesurer et d'étudier un nombre considérable de dispositifs. Cette approche s'est avérée essentielle pour contrôler et optimiser le processus technologique dans la perspective d'un développement industriel.

MOTS CLÉS

Graphene, optoélectronique microonde, mélange opto-électronique

ABSTRACT

Since the first experiment performed in 2004 by Andrej Geim et Konstantin Novosëlov, graphene has been extensively studied in the field of photonics and optoelectronics. Its extraordinary properties include very high charge carrier mobility and light absorption in a wide spectrum of wavelengths, including the telecommunication wavelength (1.55 μ m). This properties make this material very appealing for the realization of optoelectronic devices used in RADAR and telecommunications. Moreover, since graphene can be integrated the standard silicon technological platform, it has the potential to substitute III-V materials. The application domain of graphene-based devices and components has considerably grown during the last years. Nevertheless, since the key parameters impacting the performances of graphene-based optoelectronic devices are still not properly controlled, the number of applications at the industrial scale remains very limited. In this thesis work, optoelectronic mixing, a very used function in RADAR and telecommunication systems, is demonstrated by using graphene-based devices. First, we performed a statistical study of charge carrier mobility, residual doping and contact resistance. This study allowed to identify the best technological process and the best characterization methods (choice of the test devices and of the parameters extraction methods). By using this optimized procedure, we realized the first demonstration of a high frequency optoelectronic mixer based on graphene. Then, an in-depth study of several RF devices with different geometries allowed to identify the best operation conditions and the best design. Using the designed coplanar waveguides as well as an alternative method relying on high frequency based RF transistors, the optoelectronic mixing in graphene has been demonstrated up to 67 GHz. The majority of this work has been conducted using statistical methods. To do so, I implemented a automatized experimental set-up which enabled the study of a considerable number of devices. This approach has proven to be essential for controlling and optimizing the technological process in the perspective of an industrial development.

KEYWORDS

Graphene, microwave optoelectronics, optoelectronic mixing,